

UNIVERSIDADE DE LISBOA
FACULDADE DE CIÊNCIAS
DEPARTAMENTO DE QUÍMICA E BIOQUÍMICA



Synthesis and characterization of abiotic electrocatalysts based on reduced graphene oxide for oxygen reduction reaction

Ana Catarina Gomes Moreira Alves

Mestrado em Química
Especialização em Química

Dissertação orientada por:
Doutor Jorge Manuel Palma Correia
Doutor Lionel Dubois

2019

ON THE INTERNATIONAL YEAR OF THE PERIODIC TABLE OF CHEMICAL ELEMENTS, 2019

The research described in this thesis was integrated in the Interfacial Electrochemistry group, of the center of Chemistry and Biochemistry, in the research facilities of the Faculty of Sciences of University of Lisbon, Portugal, under the supervision of Professor Jorge Correia.

Under the Erasmus Placement Program, the investigation work was also developed on the facilities of the *Commissariat à l'énergie atomique et aux énergies alternatives* (CEA), in the *Institut Nanosciences et Cryogénie* (INAC) and *Systèmes Moléculaires et nanomatériaux pour l'énergie et la santé* (SyMMES), in the investigation group *Conception d'architectures moléculaires et processus électroniques* (CAMPE), Grenoble, France, under the co-supervision of Professor Lionel Dubois. And in the laboratory *Techniques de l'ingénierie Médicale et de la Complexité – Informatique, Mathématiques et Applications*, Grenoble (TIMC-IMAG), in the investigation group *Systèmes Nanobiotechnologiques et Biomimétiques* (SyNaBi), in the research efforts of the University of Grenoble-Alpes, France.

So, I began to look about and write down the elements with their atomic weights and typical properties, analogous elements, and like atomic weights on separate cards, and this soon convinced me that the properties of the elements are in periodic dependence upon their atomic weights...

D. Mendeleev, Principles of Chemistry, 1905



ACKNOWLEDGEMENTS

After twelve months and it is the final countdown for my MSc degree in Chemistry by the University of Lisbon. The research presented in this dissertation would not be performed if not by the direct or indirect support of several individuals.

First and foremost, it was a pleasure to develop this dissertation with the guidance of my mentor, Professor Jorge Correia and co-supervisor Doctor Lionel Dubois. I am grateful for the opportunity of working under their supervision that enable me to progress professional and personally. Their support and guidance allowed me to develop critical ideas about the topic and work independently on the laboratory.

I would like to extent my gratitude to Abdel Zebda, Florence Duclairoir and Yves Chenavier, who warmly received me in Grenoble and facilitated the integration on the amazing team of CAMPE. I would also like to thank Professor Ana Viana, who always gave me some good advices and struggle with me on AFM images of graphene materials; Doctor Virgínia Ferreira, Tânia Frade and Luís Almeida, who were impeccable during the relentless battle with the platinum nanoparticles and the rotating disk electrode.

A huge thanks to all the people in the CAMPE laboratory, specially Johan Loison, Coralie Marcucci, Sandy Perie and Gauthier Menassol for all the good laughs, amazing lunches, incredible cheese and, more importantly, their friendship; I would like also to extent my gratitude to all lab partners in *Eletroquímica Interfacial*, who were always supportive in some dark times.

A special mention to all my friends in Grenoble, particularly, Lisa, for all the good times, all the great talks and Friday night pizza. I will always be grateful; and back in Portugal, wherever we are, we always find a way to *mocar*.

Por fim, gostaria de deixar uma palavras de gratidão aos meus pais e aos meus irmãos. I am thankful for all the unconditional support, unrestricted laughs and unlimited love. *Ao Carlos.* For all the patience, support and love. *À minha família Dimas Dinis.*

ABSTRACT

The use of low-temperature fuel cells as power supplies of energy conversion devices is attracting considerable interest because of the direct electrochemical conversion of a fuel, *e.g.* hydrogen and glucose, and an oxidant, such as oxygen, producing electrical current. The sluggish kinetic of the oxygen reduction reaction (ORR) on the cathode half-reaction is particularly investigated since its acceleration relies on the development of efficient electrocatalysts. Unfortunately, the most promising catalysts for ORR are platinum-based materials that exhibit poor durability, limited resource and high cost. Under such circumstances, the development of non-noble, efficient and low-cost electrocatalysts has attracted a great deal of attention.

The present dissertation focuses on the synthesis and physicochemical characterization of graphene-based materials doped with nitrogen and 2 and 10 wt % transition metals (Fe, Co, Mn, Cu, Ni and Rh), denoted as rGO/M 2 and 10 %, capable of reducing molecular oxygen. Firstly, nitrogen-doped reduced graphene oxide with atomically dispersed transition metal materials were synthesized using commercial graphene as precursor. A sequential extra-exfoliation and oxidation of the graphene increased the *d*-spacing between carbon layers and created porosity on the structure, which is essential for the diffusion of reactants on the material. Further simultaneous N doping and reduction of graphene oxide using thermal and low-temperature plasma treatment allowed the formation of M-N_x active sites that contribute greatly on the ORR activity. The obtained carbon structure exhibited a large specific surface area (*c.a.* 800 m² g⁻¹) doped with *c.a.* 1.98 wt % of nitrogen. The incorporation of atomically dispersed metal reached 21 % of 2 wt %, 3 % and 0.46 % of 10 wt % using different reduction methods.

The engagement of aromatic macrocycle molecules, particularly iron and cobalt metalloporphyrins, in the graphene oxide structure was also studied. The synthesis of these hybrid materials was based on a procedure described previously, relying on the addition of the metalloporphyrin to the graphene structure, followed by its pyrolysis under N₂ atmosphere.

The ORR electrochemical characterization of the materials was performed using hydrodynamic convective systems: the rotating disk electrode (RDE) and the rotating ring-disk electrode (RRDE), in acidic, alkaline and neutral media. Among all the synthesized materials, iron- and cobalt-based materials showed the highest performance towards ORR. In particular rGO/Fe 2 % exhibited a remarkable activity in acidic (E_{onset} 0.76 V vs. RHE), alkaline (E_{onset} 0.91 V vs. RHE) and neutral (E_{onset} 0.78 V vs. RHE) media, comparable to Pt/C catalysts. A mixed 2- and 4-electron pathway was observed for rGO/Fe 2 % in acidic and alkaline media due to the contributions of several functional groups in the structure. The remaining materials displayed lower onset potential in acidic (0.44 to 0.71 V vs. RHE), alkaline (0.80 to 0.87 V vs. RHE) and neutral (0.64 to 0.74 V vs. RHE) media. The outstanding ORR performance of these materials is attributed to the presence of M-N_x active sites dispersed in the carbon structure and intrinsic ORR activity of metalloporphyrins.

Keywords: graphene oxide, reduced graphene oxide, transition metal, atomically dispersed metals, aromatic macrocycle molecules, oxygen reduction reaction.

RESUMO

Com o desenvolvimento de dispositivos de conversão de energia, a utilização de células de combustível de baixa temperatura tem captado bastante interesse da comunidade científica, devido à conversão eletroquímica de um combustível, *p. ex.* o hidrogénio e a glucose, e um oxidante, como o oxigénio, produzindo corrente elétrica. A limitação cinética por parte da reação de redução do oxigénio (ORR) é um ramo de particular interesse de estudo, devido à possibilidade de inovação de catalisadores capazes de reduzir o oxigénio de forma eficiente. Atualmente, os catalisadores à base de platina são os materiais mais promissores para a ORR; no entanto, a sua baixa durabilidade, recursos limitados, e elevado custo tornam a sua aplicabilidade condicionada em sistemas eletrónicos. Nestas circunstâncias, o desenvolvimento de eletrocatalisadores de baixo custo e de igual desempenho tem atraído a atenção de estudos recentes.

Este trabalho de investigação foca na síntese e na caracterização de materiais com base de grafeno dopado com átomos de azoto e 2 e 10 *wt %* de metal de transição (Fe, Co, Mn, Cu, Ni e Rh), designado rGO/M 2 e 10 %, aplicáveis na reação de redução do oxigénio. Inicialmente, o trabalho consistiu na síntese de grafeno oxidado (GO), utilizando grafeno comercial como precursor. A extra-exfoliação seguida da oxidação do grafeno permitiram o aumento do *d-spacing* entre camadas de grafeno, para além de formar uma estrutura porosa no material, características essenciais para a difusão dos reagentes. Posteriormente, a simultânea dopagem e redução do GO utilizando um tratamento térmico com NH₃ e plasma com N₂ permitiu a formação de sites ativos M-N_x que contribuem consideravelmente para a redução do oxigénio. Os catalisadores obtidos apresentam uma grande área superficial (*c.a.* 800 m² g⁻¹) dopado com, aproximadamente, 1,98 *wt %* de azoto. A incorporação dos metais de transição alcançou 21 % de 2 *wt %*, 3 % e 0,46 % de 10 *wt %*, usando os diferentes métodos de redução/dopagem.

A imobilização de moléculas macrocíclicas aromáticas na estrutura do GO também foi estudada, em particular a incorporação de metaloporfirinas de ferro e cobalto. A síntese destes materiais híbridos foi conseguida através de uma metodologia descrita previamente, baseando-se na adição das metaloporfirinas no GO, seguida da pirólise dos materiais em atmosfera de azoto.

A caracterização eletroquímica da ORR na presença dos catalisadores sintetizados foi realizada utilizando sistemas hidrodinâmicos com convecção, como por exemplo o elétrodo rotativo de disco (RDE) e o elétrodo rotativo de disco e anel (RRDE), em meios ácido, alcalino e neutro. De entre os materiais sintetizados, os de ferro e cobalto demonstraram maior atividade catalítica na redução do oxigénio. Em particular, o rGO/Fe 2 % apresentou uma atividade notável em meio ácido (E_{onset} 0,76 V vs. RHE), alcalino (E_{onset} 0,91 V vs. RHE) e neutro (E_{onset} 0,78 V vs. RHE), que é comparável à atividade dos catalisadores de platina. Relativamente ao número de eletrões transferidos durante a reação, foi observada uma mistura dos mecanismos de 2- e 4-eletrões para o rGO/Fe 2 % devido a diferentes contribuições dos diversos grupos funcionais na estrutura do material. Os restantes materiais demonstram um valor mais baixo de *onset* de potencial em meio ácido (0,44 to 0,71 V vs. RHE), alcalino (0,80 to 0,87 V vs. RHE) e neutro (0,64 to 0,74 V vs. RHE). A *performance* destes materiais foi atribuída ao sites ativos M-N_x dispersos na estrutura do grafeno e à atividade intrínseca das metaloporfirinas.

Palavras-chave: grafeno oxidado, grafeno oxidado e reduzido, metal de transição, metais atómicamente dispersos, moléculas macrocíclicas aromáticas, reação de redução do oxigénio.

CONTENTS

Acknowledgements	ii
Abstract	iii
<i>Resumo</i>	iv
List of Figures	vii
List of Tables	xi
List of Abbreviations	xiii
List of Symbols	xv
1. Background and motivation	1
2. Theoretical considerations	4
2.1. Oxygen reduction reaction	4
2.1.1. General aspects of ORR	4
2.1.2. Mechanism of ORR	7
2.2. Non-noble transition metal-based catalysts for ORR	9
2.2.1. The sp^2 carbon support	9
2.2.1.1. Preparation of graphene oxide	10
2.2.1.2. N-doped graphene oxide	10
2.2.1.3. Methods of N-doping and reducing graphene	11
2.2.1.4. N-doped graphene oxide as electrocatalysts for ORR	13
2.2.2. Metal/Macrocycle and Nitrogen doped reduced graphene oxide	14
2.2.2.1. Transition metal doped reduced graphene oxide	16
2.2.2.2. Macrocycle and nitrogen doped reduced graphene oxide	19
3. Experimental details and methods	21
3.1. Synthesis of electrocatalysts	21
3.1.1. Chemicals	21
3.1.2. Catalyst preparation	22
3.1.2.1. Synthesis of GO	22
3.1.2.2. GO doping with nitrogen and transition metal	22
3.1.2.3. Incorporation of porphyrins in GO	23
3.2. Characterization techniques	24
3.2.1. Electrochemical characterization	24
3.2.1.1. Potential sweep methods: Cyclic voltammetry	24
3.2.1.2. Hydrodynamic methods: Convective diffusion systems	25
3.2.1.3. Kinetics of ORR	29
3.2.1.4. Experimental section	29
3.2.2. Atomic Force Microscopy	30
3.2.2.1. Introduction of Scanning Probe Microscopy	30
3.2.2.2. AFM topographic modes	31
3.2.2.3. Experimental details	33
3.2.3. BET specific surface area analysis	33
3.2.3.1. The Langmuir isotherm and physical adsorption	33
3.2.3.2. BET theory	34
3.2.3.3. Experimental section	36
3.2.4. Further characterization	36

4. Results and discussion	37
4.1. Analysis of the synthesis of graphene oxide	37
4.2. Role of the surface structure and N-doped on ORR	40
4.2.1. Atomically dispersed transition metals in rGO	40
4.2.2. The effect of aromatic macrocycle metalloporphyrins in rGO	48
4.3. Electrocharacterization of modified rGO materials towards ORR	50
4.3.1. The effect of pH of the electrolyte: a brief analysis	52
4.3.2. Role of graphene oxide	57
4.3.3. Metal and N-doping of graphene oxide	60
4.3.4. Macrocycle doping of graphene oxide	63
4.3.5. Rotating ring-disk electrode on ORR	68
4.3.6. ORR electrochemical kinetics	70
5. Conclusions and future perspectives	71
Bibliography	73
Appendix A	85
Appendix B	90
Appendix C	92
Appendix D	93

LIST OF FIGURES

Figure 2.1. Schematic representation of the dissociative 4-electron reduction (green arrow) and associative 2- (orange arrow) and 4-electron (red arrow) reduction mechanism for the reduction of oxygen in a catalytic surface [29].	5
Figure 2.2. Free-energy diagram for oxygen reduction over Pt(111) catalytic surface by the (a) dissociative and (b) associative mechanisms. Results for low oxygen coverage are described at zero cell potential ($U = 0$ V vs. SHE) and at equilibrium potential ($U = 1.23$ V vs. SHE), assuming 0.5 oxygen coverage. Adapted from [31].	6
Figure 2.3. (a) Volcano plot showing the relationship between the ORR activity and the O binding energy and (b) ORR activity as a function of both O and OH binding energy [31].	7
Figure 2.4. Molecular diagram of oxygen molecule in ground state.	7
Figure 2.5. Representation of the proposed models for adsorbed oxygen molecule and the corresponding pathways to its reduction [32].	8
Figure 2.6. Proposed mechanism of the oxygen reduction reaction in an aqueous solution. The indices $*$, b and a designate bulk, vicinity of the disk electrode and adsorbed molecule, respectively. Adapted from [34].	9
Figure 2.7. Schematic key techniques to synthesize graphene oxide and reduced graphene oxide. Adapted from [50].	10
Figure 2.8. Schematic of N-doping graphene oxide and the location of different nitrogen atoms in the carbon structure.	11
Figure 2.9. Schematic representation of the oxygen containing functional groups on graphene oxide and N-doping simultaneous reduction of graphene oxide.	12
Figure 2.10. (a) Schematic representation of the synthesis of NC-2 and 3. The synthesis approach of NC-1 is similar to NC-3 except that no ferric nitrate and titanium dioxide was added. Adapted from [90]. (b) Polarization curve of N-GFs-TPA electrocatalysts in O_2 -saturated 0.1 M $HClO_4$ solution, at 10 $mV s^{-1}$ [89].	13
Figure 2.11. (a) Comparison between onset and half-wave potentials of N-G-800, 900 and 1000 catalysts and (b) the proposed ORR mechanism scheme of N-doped graphene [89].	14
Figure 2.12. Schematic of (a) the synthesis of the electrocatalysts CNT@Fe-N-PC prepared by PPy polymerization on the CNTs, followed by Fe^{3+} adsorption and pyrolysis [36] and (b) the ORR catalysts characterized by a F-N-C core-shell structure [35].	17
Figure 2.13. Schematic illustration of cobalt and nitrogen doped carbon nanosheets (Co-N-PCN) [114].	18
Figure 2.14. Schematic of (a) the synthesis of atomically dispersed Mn-N active sites in ZIF-8 (Adapted from [101]) and (b) Mn-N-C catalysts synthesized by the polymerization and pyrolysis of polyaniline hydrogel [108].	19
Figure 2.15. Schematic of (a) vitamin B_{12} molecule, highlighting the axial back ligand, (b) FetMPyP/BIm@rGO catalysts, emphasizing the interaction between the BIm and rGO [137] and (c) ERGO-Co-APFP catalyst [138].	20
Figure 3.1. Schematic of the synthesis of GO via commercial graphene.	22
Figure 3.2. Schematics of the synthesis of rGO/M 2 and 10 % electrocatalysts catalysts.	23
Figure 3.3. Potential-time profiles: (a) linear sweep voltammetry and (b) cyclic voltammetry and (c) a cyclic voltammogram for a reversible charge-transfer reaction.	24

Figure 3.4. Convective diffusion systems (a) flow through channel, (b) flow through channel with turbulence promoter, (c) fluidized bed electrode, (d) packed bed electrode; (e) rotating disk electrode with a concentric tube and a schematic illustration of flow patterns created by the RDE. Adapted from [143, 145].	25
Figure 3.5. Steady state concentration profile for the electroactive species using Nernst diffusion layer model.	26
Figure 3.6. Complete I-E curves over a wide range of overpotentials.	27
Figure 3.7. (a) Rotating ring-disk electrode system and (b) an example for a RRDE curve, in which the reaction in the ring and the disk are marked in the Figure [147].	28
Figure 3.8. Schematic of a rotating ring-disk electrode in a single compartment cell. Adapted from [148]. Copyright 2018, American Chemical Society.	30
Figure 3.9. (a) Schematics of atomic force microscopy apparatus [149] and (b) Qualitative sketch of the force between tip and sample as function of tip-sample distance and respective regimes [151].	31
Figure 3.10. Qualitative plot of the interaction force between the tip and the sample as a function of the distance to the surface [149].	32
Figure 3.11. Schematics of a force-distance curve showing (a) contact in a repulsive region, (b) non-contact AFM, (c) intermittent-contact regime and (d) different operating regimes for oscillating AFM modes: A – small amplitude and B – large amplitude of oscillation.	32
Figure 3.12. Surface area and porosity in a porous material. Adapted from https://www.particletesting.com/surface-area/ .	34
Figure 4.1. Transmission electron microscopy (TEM) image of nearly transparent graphene nanoplatelet aggregates. Adapted from [154].	37
Figure 4.2. (a) Schematic representation of graphite, highlighting the thickness of the graphene layers [157] and (b) Atomistic model of two oxygen containing functional (i) epoxy (ii) hydroxyl groups and (iii) epoxy and hydroxyl groups on both sides of the graphene sheet. Adapted from [156].	38
Figure 4.3. Morphologic image from AFM of (a) graphene oxide wet (550.8 x 550.8 nm), (b) graphene oxide dry (550.8 x 550.8 nm) and (c) X-ray diffraction patterns of graphene oxide and an expanded window between $2\Theta = 40$ and 70° (inset graph).	38
Figure 4.4. Morphologic 2D image from AFM of (a) HOPG and (b) graphene oxide wet in HOPG (1.1 x 1.1 μm).	39
Figure 4.5. (a) FT-IR spectrum of graphene oxide, highlighting the presence of different oxygen containing functional groups and (b) N_2 adsorption-desorption isotherm of graphene oxide.	39
Figure 4.6. Schematic representation of the oxygen and nitrogen containing functional groups on reduced graphene.	40
Figure 4.7. Morphologic image from AFM of (a) rGO/Fe 2 % (820.3 x 820.3 nm), (b) rGO/Fe 10 % (c) rGO/Co 2 % and (d) rGO/Co 10 % (830.8 x 830.8 nm).	41
Figure 4.8. X-ray diffraction patterns of modified rGO electrocatalysts (inset graph of rGO/Fe 2 %).	42
Figure 4.9. FT-IR spectra of (a) rGO/M 2 wt % under argon atmosphere from 4000 to 400 cm^{-1} and (b) rGO/M 10 wt % under air atmosphere, highlighting the presence of different oxygen and nitrogen containing functional groups, from 4000 to 1000 cm^{-1} .	42
Figure 4.10. Raman spectra of graphene oxide and reduced graphene oxide doped with 2 and 10 wt % Fe and Co and corresponding ratio I_D/I_G .	43

Figure 4.11. (a) XPS full and (b) high-resolution N 1s spectra of GO and rGO/M 2 %, M = Fe, Ni and Mn 2 %.....	44
Figure 4.12. TGA and DTG curves of (a) graphene oxide, (b) TGA curves of graphene oxide and modified rGO 2 wt % materials and an expanded window between 600 and 800 °C (inset graph) and (c) rGO/Co 2 %.....	45
Figure 4.13. Nitrogen adsorption-desorption isotherm of the GO, rGO/Ni 2 % M1, rGO/Ni 10 % M1 and rGO/Ni 10 % M2.....	47
Figure 4.14. Brief schematics of the synthesis of rGO/M 2 and 10 % electrocatalysts catalysts, highlighting the different steps used in the ICP-OES analysis.....	48
Figure 4.15. Schematic of (a) iron and (b) cobalt tetramethoxyphenyl porphyrins and (c) manganese metalloporphyrin.....	49
Figure 4.16. (a) Schematic illustration of π interaction between the aromatic structure of the macrocycle and the electronic π -system of graphene [163] and (b) morphologic AFM 3D image of rGO/CoP.....	49
Figure 4.17. (a) FT-IR and (b) Raman spectra of graphene oxide and doped rGO with macrocycle molecules.....	50
Figure 4.18. Schematic of the possible mechanism of oxygen reduction by the transfer of 2, 4 or 2+2 electrons.....	51
Figure 4.19. Comparison of the ORR polarization curves of rGO/M 2 % in air-saturated (a) 0.1 M H ₂ SO ₄ , (b), 0.1 M KOH and (c) 0.01 M PBS electrolytes recorded at 800 rpm on GC modified electrode at 10 mV s ⁻¹	52
Figure 4.20. Comparison of the ORR polarization curves of rGO/M 10 % in air-saturated (a) 0.1 M H ₂ SO ₄ , (b), 0.1 M KOH and (c) 0.01 M PBS electrolytes recorded at 800 rpm on GC modified electrode at 10 mV s ⁻¹	55
Figure 4.21. Comparison of the ORR polarization curves of rGO/P 2 % in air-saturated (a) 0.1 M H ₂ SO ₄ , (b), 0.1 M KOH and (c) 0.01 M PBS electrolytes recorded at 800 rpm on GC modified electrode at 10 mV s ⁻¹	56
Figure 4.22. Comparison of the ORR onset and half-wave potentials between Pt/C and rGO/M and P 2 % electrocatalysts in (a) 0.1 M H ₂ SO ₄ and (b) 0.1 M KOH solutions.....	57
Figure 4.23. Polarization curves of graphene oxide in a GC rotating disk electrode recorded at different rotation rates for ORR N ₂ and air-saturated 0.1 M H ₂ SO ₄ at 10 mV s ⁻¹	58
Figure 4.24. (a) Carbon surface features of relevance to the electrochemistry and details of some different oxygen-containing surface functional groups. Adapted from [28]. (b) Koutecký-Levich plots at different potentials. Inset graph: the variation of number of electrons with the potential.....	58
Figure 4.25. Polarization curves of graphene oxide in a GC rotating disk electrode recorded at different rotation rates for ORR N ₂ and air-saturated (a) 0.1 M KOH and (b) 0.01 M PBS, at 10 mV s ⁻¹ . Inset: Koutecký-Levich plots at different potentials.....	59
Figure 4.26. Protonation of nitrogen atoms upon the reduction of oxygen in aqueous acidic solution.....	59
Figure 4.27. (a) Polarization curves of rGO/Fe 2 % on GC modified electrode in N ₂ and air-saturated 0.1 M H ₂ SO ₄ solution at different rotation speed at 10 mV s ⁻¹ and (b) correspondent K-L plots at several potentials.....	60
Figure 4.28. Polarization curves of rGO/Fe 2 % in a GC rotating disk electrode recorded at different rotation rates for ORR N ₂ and air-saturated (a) 0.1 M KOH and (b) 0.01 M PBS, at 10 mV s ⁻¹ . Inset: Koutecký-Levich plots at different potentials.....	61

Figure 4.29. (a) Polarization curves of rGO/Co 2 % on GC modified electrode in N ₂ and air-saturated 0.1 M H ₂ SO ₄ solution at different rotation speed at 10 mV s ⁻¹ and (b) correspondent K-L plots at several potentials.	62
Figure 4.30. Polarization curves of rGO/Co 2 % in a GC rotating disk electrode recorded at different rotation rates for ORR N ₂ and air-saturated (a) 0.1 M KOH and (b) 0.01 M PBS, at 10 mV s ⁻¹ . Inset: Koutecký-Levich plots at different potentials.	62
Figure 4.31. (a) Polarization curves of rGO/FeP 2 % on GC modified electrode in N ₂ and air-saturated 0.1 M H ₂ SO ₄ solution at different rotation speed at 10 mV s ⁻¹ and (b) correspondent K-L plots at several potentials.	64
Figure 4.32. Polarization curves of rGO/FeP 2 % in a GC rotating disk electrode recorded at different rotation rates for ORR N ₂ and air-saturated (a) 0.1 M KOH and (b) 0.01 M PBS, at 10 mV s ⁻¹ . Inset: Koutecký-Levich plots at different potentials.	64
Figure 4.33. (a) Polarization curves of rGO/CoP 2 % on GC modified electrode in N ₂ and air-saturated 0.1 M H ₂ SO ₄ solution at different rotation speed at 10 mV s ⁻¹ and (b) correspondent K-L plots at several potentials.	65
Figure 4.34. Polarization curves of rGO/CoP 2 % in a GC rotating disk electrode recorded at different rotation rates for ORR N ₂ and air-saturated (a) 0.1 M KOH and (b) 0.01 M PBS, at 10 mV s ⁻¹ . Inset: Koutecký-Levich plots at different potentials.	66
Figure 4.35. Polarization curves of rGO/VB ₁₂ 2 % in a GC rotating disk electrode recorded at different rotation rates for ORR N ₂ and air-saturated (a) 0.1 M H ₂ SO ₄ , (b) 0.1 M KOH and (c) 0.01 M PBS, at 10 mV s ⁻¹ . Inset: Koutecký-Levich plots at different potentials.	66
Figure 4.36. Schematic of the sequential steps of depositing modified rGO electrocatalysts in the surface of an electrode using drop-casting technique.	68
Figure 4.37. Polarization curves of rGO/M 2 % and rGO/P 2 %, M= Fe and Co and P = FeP, CoP and VB ₁₂ in an Au/Au rotating ring-disk electrode recorded at 600 rpm for ORR in air-saturated 0.1 M H ₂ SO ₄ , at 10 mV s ⁻¹ (Bottom figure); Ring potential 0.9 V vs. SCE (Upper figure).....	69
Figure 4.38. Picture of the Au/Au RRDE modified with a rGO/M electrocatalysts, highlighting a heterogeneous film of material in the disk electrode surface.....	69
Figure 4.39. Tafel plots of rGO/M 2 % and rGO/P 2 %, M = Fe and Co and P = FeP, CoP and VB ₁₂ in 0.1 M H ₂ SO ₄ solution and at 800 rpm.....	70

LIST OF TABLES

Table 2.1. Summary of the synthesis of recent N-doped carbon materials with C, O and N atomic contents of the catalysts and the correspondent electrocatalytic activity. The potentials values correspond to the onset potential and half-wave potential values vs. the reversible hydrogen electrode (RHE) at 25 °C.	15
Table 3.1. Calculated values for x wt % ($x = 2$ and 10) metal precursors used for doping of graphene.	22
Table 3.2. Metalloporphyrins precursors used for 2 wt % doping of graphene. The values in brackets is the mass weighted of wet graphene.	24
Table 4.1. Atomic concentration, <i>at</i> %, of C 1s, N 1s and O 1s in the samples GO, rGO/M 2 %, M = Fe, Ni and Mn 2 % determined by XPS. The values inside brackets are assigned to the calculated weight percentage, <i>wt</i> %	44
Table 4.2. TGA minimum weight loss in % of graphene oxide and rGO/M 2 % electrocatalysts.	46
Table 4.3. BET surface area and pore structures of the electrocatalysts GO, rGO M2, rGO/Ni 2 %, rGO/Ni 10 % M1 and rGO/Ni 10 % M2.....	47
Table 4.4. Elemental composition in wt % of nickel in reduced graphene oxide doped catalysts synthesized by M1 and M2, according to the different steps highlighted in Figure 4.14.	48
Table 4.5. Experimental parameters used in the Koutecký-Levich equation for the determination of the number of electrons, according to the electrolyte used in the measurement.....	51
Table 4.6. Electrocatalytic activity of the GC rotating disk electrode modified rGO materials in aqueous 0.1 M H ₂ SO ₄ , 0.1 M KOH and 0.01 M PBS solutions. The potentials values correspond to the onset and half-wave potential values vs. SCE. The values inside brackets are assigned to the E_{onset} and E_{half} potential values vs. reversible hydrogen electrode (RHE).....	53
Table 4.7. Number of electrons calculated by K-L plots for rGO/M 2 % materials in acidic, alkaline and neutral electrolyte solutions.	54
Table 4.8. Number of electrons calculated by K-L plots for rGO/M 10 % materials in acidic, alkaline and neutral electrolyte solutions.	55
Table 4.9. Number of electrons calculated by K-L plots for rGO/P 2 % materials in acidic, alkaline and neutral electrolyte solutions.	56
Table 4.10. Contribution of ORR 2- and 4-electron pathway in GO in acidic, alkaline and neutral electrolyte solutions.	60
Table 4.11. Contribution of ORR 2- and 4-electron pathway in rGO/Fe 2 % and rGO/Co 2 % in acidic, alkaline and neutral electrolyte solutions.....	61
Table 4.12. Contribution of ORR 2- and 4-electron pathway in rGO/Fe 2 % and rGO/Co 2 % in acidic, alkaline and neutral electrolyte solutions. The metal, nitrogen and carbon contributions are denoted as <i>M</i> , <i>N</i> and <i>C</i> , respectively.....	63
Table 4.13. Contribution of ORR 2- and 4-electron pathway in rGO/FeP, rGO/CoP and rGO/VB ₁₂ in acidic, alkaline and neutral electrolyte solutions.	65
Table 4.14. Contribution of ORR 2- and 4-electron pathway in rGO/FeP, rGO/CoP and rGO/VB ₁₂ in acidic, alkaline and neutral electrolyte solutions.	67
Table 4.15. Electrocatalytic activity of the GC rotating ring-disk electrode modified with rGO-based materials in 0.1 M H ₂ SO ₄ solution and the contributions of active sites in the material. The potentials values correspond to the onset potential and half-wave potential values vs. SCE (the potentials in brackets are assigned to the potentials vs. reversible hydrogen electrode (RHE) at 25 °C).	67

Table A.1. Electrocatalytic activity comparison of recent advances on iron-nitrogen co-doped carbon materials. The potentials values correspond to the onset potential and half-wave potential values vs. the reversible hydrogen electrode (RHE) at 25 °C..... 85

Table A.2. Electrocatalytic activity comparison of recent advances on cobalt-nitrogen co-doped carbon materials. The potentials values correspond to the onset potential and half-wave potential values vs. the reversible hydrogen electrode (RHE) at 25 °C..... 86

Table A.3. Electrocatalytic activity comparison of recent advances on manganese-nitrogen co-doped carbon materials. The potentials values correspond to the onset potential and half-wave potential values vs. the reversible hydrogen electrode (RHE) at 25 °C. 87

Table A.4. Electrocatalytic activity comparison of recent advances on copper-nitrogen co-doped carbon materials. The potentials values correspond to the onset potential and half-wave potential values vs. the reversible hydrogen electrode (RHE) at 25 °C..... 88

Table A.5. Electrocatalytic activity comparison of recent advances on macrocycle doped carbon materials. The potentials values correspond to the onset potential and half-wave potential values vs. the reversible hydrogen electrode (RHE) at 25 °C..... 88

LIST OF ABBREVIATIONS

AFM – Atomic force microscopy

BET – Brunauer-Emmett-Teller theory

BFC – Biofuel cell

CCa – Calcium citrate

CNT – Carbon nanotube

CoP – Cobalt(II) meso-Tetra(4-sulfonatophenyl) porphyrin chloride

CV – Cyclic voltammetry

CVD – Chemical vapour deposition

DFT – Density functional theory

DNA – Deoxyribonucleic acid

DTG – Difference thermogravimetric ratio between weight loss and time

EPR – Electron paramagnetic resonance

FeP – Iron(II) meso-Tetra(4-sulfonatophenyl) porphyrin tetrasodium chloride

FT-IT – Fourier-transform infrared spectroscopy

GCE – Glassy carbon electrode

GO – Graphene oxide

HOPG – Highly oriented pyrolytic graphite

ICP-OES – Inductively Coupled Plasma – Optical Emission Spectroscopy

IMD – Implantable medical device

K-L – Koutecký -Levich plot/equation

LSV – Linear sweep voltammetry

MnP – Manganese(II) porphyrin

MOF – Metal-organic framework

NHE – Normal hydrogen electrode

ORR – Oxygen reduction reaction

PBS – Phosphate buffered saline

RDE – Rotating disk electrode

RDS – Rate-determining step

rGO – Reduced graphene oxide

RHE – Reversible hydrogen electrode

RRDE – Rotating ring-disk electrode

SCE – Saturated calomel electrode

SPM – Scanning probe microscopy

STM – Scanning tunneling microscopy

STP – Standard temperature and pressure

TGA – Thermogravimetric analysis

VB₁₂ – Vitamin B₁₂

XPS – X-ray photoelectron spectroscopy

XRD – X-ray diffraction

LIST OF SYMBOLS

A_m	Area occupied by one molecule on the surface of the material, m^2
$A_{\text{micropore}}$	Micropore total area, $m^2 g^{-1}$
S_{ABET}	Surface area, $m^2 g^{-1}$
S_{BET}	Slope of the BET curve
I_{BET}	Intercept of the BET curve
S_{ext}	External surface area, $m^2 g^{-1}$
$c_{(x=0)}$	Concentration at the electrode surface, mol dm^{-3}
c^∞	Bulk concentration, mol dm^{-3}
$C_i v$	Convective flux, $\text{mol dm}^{-3} \text{cm}^{-2} \text{s}^{-1}$
D_i	Diffusion coefficient, $\text{cm}^2 \text{s}^{-1}$
E_{eq}	Equilibrium potential, V
E_{half}	Half-wave potential, V
E_{onset}	Onset potential, V
η	Overpotential, V
ΔE_{O}	Binding energy of the oxygen species, V
ΔE_{OH}	Binding energy of the hydroxide species, V
F	Faraday constant, 96485 C mol^{-1}
i_k	Current density controlled by kinetic processes, mA cm^{-2}
j	Current density, mA cm^{-2}
j_0	Exchange current density, mA cm^{-2}
j_{2e}	2-electron current density, mA cm^{-2}
j_{4e}	4-electron current density, mA cm^{-2}
j_c	Current density of the cathodic half-reaction, mA cm^{-2}
j_D	Current density at the disk electrode, mA cm^{-2}
J_i	Flux involved in the diffusion mass transport per unit area and time, $\text{mol dm}^{-3} \text{cm}^{-2} \text{s}^{-1}$
j_L	Limiting current density, mA cm^{-2}
k	Boltzmann's constant, 1.380 J K^{-1}
N	Collection coefficient
n	Number of electrons transferred in a redox reaction
P	Pressure of a gas, Pa
Q_i	Heat of adsorption in i layer, J mol^{-1}
R	Gas constant, $8.314 \text{ J K}^{-1} \text{mol}^{-1}$
T	Temperature, Kelvin
V_{ads}	Standard volume adsorbed, $\text{m}^3 \text{g}^{-1}$
$V_{\text{mesoporous}}$	Mesoporous volume, $\text{m}^3 \text{g}^{-1}$
$V_{\text{micropore}}$	Micropore volume, $\text{m}^3 \text{g}^{-1}$
$V_{\text{total pore}}$	Total pore volume, $\text{m}^3 \text{g}^{-1}$
	Percentage of transition metal
x	Or direction of mass transport
	Or the number of surface sites per unit area
α	Transfer coefficient
δ	Nernst diffusion layer
θ_i	Theta angle on XRD
	or Coverage of the sample surface covered by a number of i successive layers
κ	Proportionality constant between flux and pressure of an ideal gas
ν	Frequency of vibration
ν	Kinematic viscosity, $\text{cm}^2 \text{s}^{-1}$
ω	Angular velocity, rad s^{-1}

Background and motivation

Implantable medical devices (IMDs) represent a category of devices that are implanted inside of the human body during a medical procedure for the treatment of a malfunctioning organ or to control vital sign of a specific therapy or diagnosis [1-3]. Examples of IMDs include orthopedic rods, flexible polymer-based devices, pacemakers, cardiovascular stents, defibrillators, neural prosthetic, neurostimulators and drug delivery systems [4-7]. In the past six decades, IMDs have provided substantial benefits to the health care of patients: 8-10 % of the American population and 5-6 % of the people of industrialized countries have experienced the implantation of a device that enhanced their quality of life, relieved pain and increased longevity [1]. In particular, cardiac pacemaker is a medical device that generates electrical impulses and it is estimated that about 370 000 people receive a pacemaker per year in the U.S. [4], 98 000 patients (average age 75 years) have received a pacemaker in Germany [8] and, according to the European Society of Cardiology, in 2016, it was estimated that 590 pacemakers were implanted per million of the population over 56 countries [2]. Furthermore, it was estimated that medical devices account for 4-6 % of the total U.S. expenses on health care [6]. Therefore, with the increasing of the world's population and the respective improvement in quality of life, the conception of new implantable devices based on biomaterials is a quest for new healthcare development.

The design of new implantable electronic systems is based on safety and efficacy so there can be a minimal invasive medical procedure and discomfort for the patient. For the system to be optimized, these devices should fulfil the following requirements: small volume (minimal size and weight to reduce pain and discomfort to the patient during usage), protection barrier, high biocompatibility, minimal toxicity, low power consumption and large lifetime [1, 3, 9, 10]. Furthermore, the device should have some basic self-targeting and programmable treatment in order to reduce the surgical intervention and to be able to receive, transmit and control data.

To ensure a successful deployment and to accomplish the requirements mentioned above, several investigations were developed focusing on the power supply for IMDs. Since the first medical implant in 1958, the major challenges of the power sources are size and weight limitation, low capacity and volumetric energy density, limited lifetime and stability, difficult replacement and high cost [1, 10, 11]. Among all the batteries used for IMDs, lithium-based batteries have played a significant role as a power source due to their high volumetric energy density, low self-discharge and compacted sizes [11, 12]. Despite efforts for the implantation of this battery, lithium-based batteries have been limited to the size and potential toxicity [11].

Over the last two decades, biofuel cell (BFC) has been an alternative power supply for IMDs due to its biocompatibility with the body and high energy density that can reach up to 300 Wh kg⁻¹ [13]. The concept of BFC is based on the electrochemical reaction of a biological fuel and an oxidant on catalytic electrodes that allow the transformation of chemical energy into electric current via the transference of electrons by an external circuit. Since the first implantable biofuel cell, the reliability and efficiency of this biodevice depend on the following criteria: **(i)** low overpotentials, **(ii)** optimal availability of biofuel

and oxidant on physiological fluids, **(iii)** low self-discharging time, **(iv)** biocompatibility, in case of contact with the body fluid, **(v)** minimum size and light weight and **(vi)** operation at physiological conditions (around pH 7 and at 37 °C) [14-16].

Taking advantage of the continuous re-establishment of the reactants by the body fluids, it is possible to develop new power supplies for IMDs based on the theoretical capability for operating, as long as there is a constant supply of fuel. Typically, the biofuel and oxidant used for generating electrical current are glucose and oxygen, respectively. This feature of BFCs has been the major motivation for the development of new materials for power supplies for IMDs.

In the cathode side of a biofuel cell, a sluggish oxygen reduction reaction controls the overall performance of the BFC. In order to improve the efficiency of the BFC, platinum-based electrodes have been used as electrodes that allow the reduction of molecular oxygen to water via 4-electron transfer. However, noble-based materials are known for several drawbacks, such as high cost, low stability and poisoning [17-21]. Recently, non-noble transition metal-based electrocatalysts have been considered highly efficient, low cost and stable electrodes for ORR, specially atomically dispersed metals.

The focus of this report is the synthesis of new abiotic electrocatalysts based on reduced graphene oxide (rGO) doped with nitrogen and 2 and 10 wt % 3d single metal atoms and aromatic macrocycles and their applicability on the oxygen reduction reaction (ORR). Our main goal is to develop a new and biocompatible rGO based catalyst, produced by a simple and eco-friendly procedure, that is capable of reducing oxygen via 4-electron route to produce water as final product. Depending on the structure of the catalyst, the extent to which both 2 and 4-electron pathways are involved in ORR is studied by hydrodynamic convective methods – rotating disk electrode (RDE) and rotating ring-disk electrode (RRDE) in neutral, alkaline and acidic media.

The results obtained during this thesis and discussed in Chapter 4 were presented in the form of a panel communication in the XXVI Nacional meeting of Portuguese Society of Chemistry (XXVI *Encontro Nacional da SPQ*), 24-26 July, Porto, Portugal (Appendix C) and in the First edition of CQE Days, 30-31 May, Academy of Sciences of Lisbon (*Academia das Ciências de Lisboa*), Lisbon, Portugal (Appendix D).

To facilitate the reading, this dissertation is organized in the following sequence. In the *first chapter* of the present dissertation, background and motivation are presented, covering the problem of biocompatible and sustainable power supplies for implantable medical devices and its resolution using biofuel cells based on oxygen and glucose reactants.

The *second chapter* is devoted to a general introduction of the oxygen reduction reaction, followed by the state-of-the-art of both synthesis and electrochemical performance towards ORR of nitrogen-doped carbon-based materials. Particular attention is given to atomically dispersed iron, cobalt and manganese on carbon structure, and the correlation between their synthesis and the observed ORR catalytic activity. Furthermore, the incorporation of aromatic macrocycle molecules in the carbon framework is also discussed in this chapter as electrocatalysts for ORR.

The experimental details and methods of characterization of the synthesized materials are presented in the *third chapter*. Our approach towards the synthesis of electrocatalysts is based on an extra-exfoliation of commercial graphene, followed by its oxidation and 2 and 10 wt % doping with transition metals or metalloporphyrins. Additionally, the theoretical support of the physical and chemical characterization of the structure and the methods used in the measurement of the electrochemical activity of the materials are also described.

In the *fourth chapter*, the presentation and the discussion of the experimental results are shown. Firstly, the physical and chemical characterization of the synthesized material is approached, using several complementary techniques essential for the better understanding of the carbon system. Secondly, the electrocatalytic performance of the materials is analysed by RDE and RRDE polarization curves in acidic, alkaline and neutral media and the determination of the number of electrons is achieved using the Koutecký-Levich equation.

The conclusions of the overall thesis work is presented in the *fifth chapter*, as well as future perspectives in the field of inorganic synthesis and energy conversion devices.

Theoretical considerations

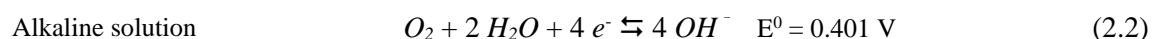
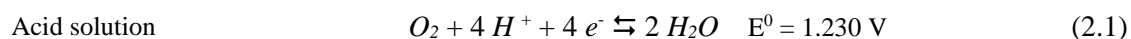
In this chapter, a brief review of oxygen reduction reaction catalysed by transition metal-N-based carbon materials is presented. Our discussion is restricted to the aspects that are relevant for the understanding of this work. Firstly, the oxygen reduction reaction is addressed, with the explanations of different pathways of the reactions, followed by the presentation of the possible mechanism of ORR. Then, a succinct analysis of the state of art on the non-noble transition metals as electrocatalysts for ORR is presented. In this subchapter, several synthesis of graphene oxide are discussed and its reduction and simultaneous doping with nitrogen atoms. Finally, a brief discussion on the synthesis and ORR electrocatalytic activity of single metal atoms and aromatic macrocycles reported recently on the literature is presented.

2.1. OXYGEN REDUCTION REACTION

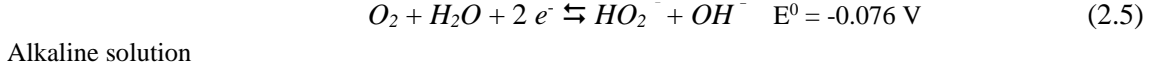
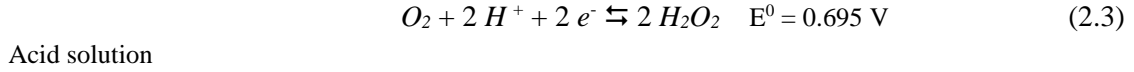
Molecular oxygen, O₂, is one of the most abundant gases in the surface of the planet Earth and its participation on several processes of storage and conversion of energy is essential for the development of new devices such as BFCs and metal-air batteries [17, 22, 23]. In order to improve the cell efficiency of fuel cells, the presence of a catalyst as cathode for the oxygen reduction is necessary. Platinum-based electrodes are known for being the most efficient catalyst for ORR [24, 25]. Because Pt-based materials suffers from high cost, low stability and poor tolerance to contaminants such as CO and NO_x [17-21], extensive research has been focused on the developing new, highly efficient, low-cost and stable non-noble metal catalysts for ORR. The alternative electrocatalysts explored include transition metals oxides, single atom transition metals, alloys, transition metal macrocyclic compounds and carbon materials.

2.1.1. GENERAL ASPECTS OF ORR

The electrochemical reduction of oxygen provides a multielectron process that allows the generation of an electrical potential through the transference of 4- or 2-electron pathway from O₂ to H₂O and O₂ to H₂O₂, respectively. Consider the full reduction of oxygen by the transference of 4-electrons in acidic and alkaline electrolytes, producing directly two water molecules.



The working potential of the ORR process in alkaline aqueous solution shift by *c.a.* - 0.800 mV with the 14-fold increase in pH. This shift can be explained by the high overpotential required for O₂/O₂^{-*} redox couple in acidic medium that is correlated to the high free energy of adsorption of O₂ of the catalysts [26]. On the other hand, the ORR can follow an incomplete two-electron pathway, resulting in the production of hydrogen peroxide as a product-adsorbed intermediate – the partial reduction of oxygen. Hereafter, the obtained peroxide species can undergo to a subsequent reduction and form water via an indirect two-step (2 + 2 electron), as shown in the following equations.



The potentials correspond to the standard reduction values vs. the normal hydrogen electrode (NHE) at 25 °C [27].

On the surface of most of the electrocatalysts, the reduction of oxygen occurs by the formation of a high-energy peroxide specie that is further reduced to form water molecules. This observation may be assigned to the high stability of the O-O bond of the oxygen molecule that has a dissociation energy of 494 kJ mol⁻¹, while the dissociation energy of O-O bond in peroxide is only 146 kJ mol⁻¹ [28].

Considering the reduction of one oxygen molecule, there are two possibilities for the reduction of oxygen in a catalytic surface: a dissociative and an associative mechanism that occurs in aqueous solutions (Figure 2.1). The key feature of the following pathways is when the O-O bond breaks [29].

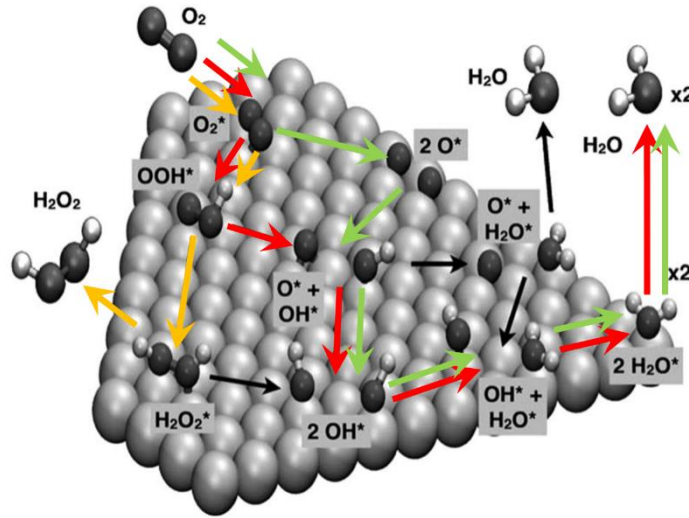
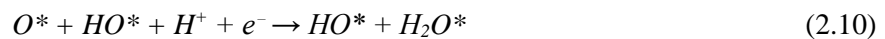


Figure 2.1. Schematic representation of the dissociative 4-electron reduction (green arrow) and associative 2- (orange arrow) and 4-electron (red arrow) reduction mechanism for the reduction of oxygen in a catalytic surface [29].

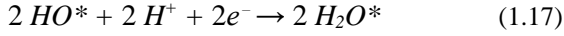
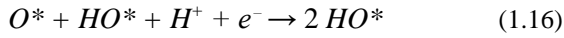
The direct dissociation of oxygen molecule has an activation barrier of > 0.5 eV, depending on the catalysts surface, which is a high energy barrier unlikely to be overcome for the reaction to happen [29-31]. The dissociative mechanism of a 4-electron pathway is described as follows: the oxygen molecule is firstly adsorbed in the surface of the catalyst, denoted O₂^{*}, followed by its dissociation in two oxygen atoms 2O^{*} and reduction to form two water molecules.



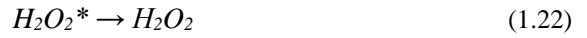
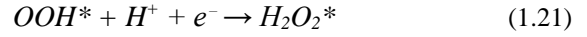
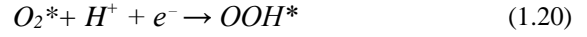


Alternatively, the associative mechanism is based on the adsorption of the oxygen molecule O_2^* to firstly form the intermediate OOH^* that is subsequently reduced to form two water molecules. An analogous mechanism is the 2-electron pathway, in which the intermediate OOH^* is reduced directly to peroxide $H_2O_2^*$.

4-electron pathway



2-electron pathway



The binding affinity to the oxygenated species determines the ORR catalytic activity of the material. Using Density Functional Theory (DFT) calculations to obtain the bond energy of O^* and OH^* , Nørskov *et al.* [31] introduced a new model that predicts a volcano-shaped relationship between the rate of the cathode reaction and the oxygen adsorption energy. The model explains why platinum-based electrodes are the most promising materials for ORR. Consider the dissociative and associative mechanisms of ORR in Pt(111) electrode, shown in Figure 2.2. Assuming that the rate-limiting step for these mechanisms is the adsorption of oxygen into the surface of the catalysts, the activation free energy for the overall process is 0.45 eV, which is close to experimental measurements as mentioned before [31].

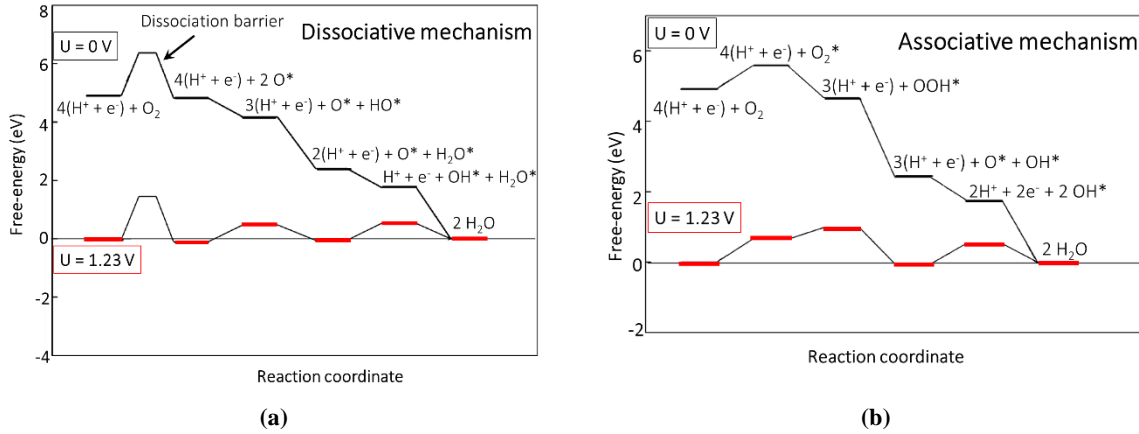


Figure 2.2. Free-energy diagram for oxygen reduction over Pt(111) catalytic surface by the (a) dissociative and (b) associative mechanisms. Results for low oxygen coverage are described at zero cell potential ($U = 0$ V vs. SHE) and at equilibrium potential ($U = 1.23$ V vs. SHE), assuming 0.5 oxygen coverage. Adapted from [31].

Based on both theoretical and experimental energy data, a volcano-shaped plot, Figure 2.3, compares the ORR catalytic activity and the oxygen (ΔE_O) and hydroxide (ΔE_{OH}) species binding energy. These plots have been used for as a starting point for the development of new catalysts for ORR, such as iron and cobalt based materials. Although highly active for ORR, platinum is not at the peak of the volcano plot which leaves room for the improvement of new catalysts.

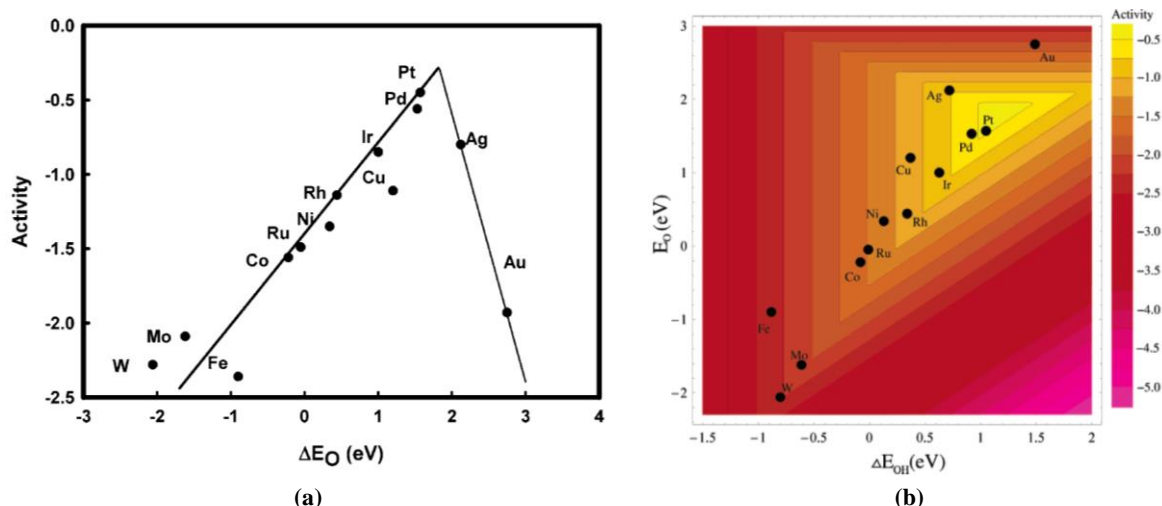


Figure 2.3. (a) Volcano plot showing the relationship between the ORR activity and the O binding energy and (b) ORR activity as a function of both O and OH binding energy [31].

The ORR electrocatalytic activity of catalysts can be studied using the following methods: gas diffusion electrodes method, steady-state polarization, cyclic voltammetry, rotating disk electrode (RDE) and rotating ring-disk electrode (RRDE). This study focuses on the cyclic voltammetry, RDE and RRDE and the principles of these techniques are discussed in detail in Chapter 3 (Experimental details and methods).

2.1.2. MECHANISM OF ORR

To begin to understand the ORR mechanism, it is necessary to study the oxygen molecule and its molecular orbital diagram (Figure 2.4). According to Hund's rule, the oxygen molecule presents two unpaired electrons located in a double degenerate π^* antibonding orbital, in the ground state, corresponding to a triplet state. The bonding orbitals of O_2 can be assigned to the σ_g orbitals with two electrons and the double degenerated π_u and π_g^* orbitals, resulting in a bond order of 2. Upon the reduction of oxygen, the electrons added occupy antibonding orbitals, decreasing the bond order of the molecule and increasing the length of the O-O bond. The excess of bonding (in σ_g , σ_g and π_u) over non-bonding (σ_u^* and π_g^*) electrons in the diagram is 4 that clarifies the high stability of the oxygen molecule, despite its high oxidizing power [28].

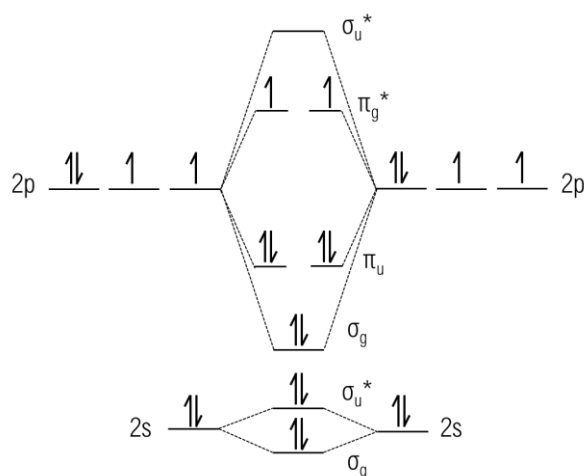


Figure 2.4. Molecular diagram of oxygen molecule in ground state.

One of the most remarkable aspects of ORR in aqueous solutions is the interaction of oxygen and active sites on the electrode surface that possess an unusual high ORR activity compared to the

neighbouring sites. Such interactions of oxygen molecules with the catalytic surface are an extremely important issue as it is going to determine the rate at which the reaction takes place (j_0 for reduction of oxygen is *c.a.* 10^{-10} to 10^{-11} A cm^{-2}) [32]. Three types of models of this interaction have been proposed, as shown in Figure 2.5. The Griffiths model described a lateral interaction of π orbitals of oxygen molecule with empty d_z^2 orbitals of the transition metal, forming a σ bond and a backbond interaction between partially filled d_{xz} or d_{yz} orbitals of the transition metal to the π^* orbitals of the oxygen [32]. A strong interaction of this type may weaken the O-O bond, dissociating the molecule, followed by a simultaneous proton addition and the reduction of the transition metal.

The following model is the Pauling model that is the most probably structure of adsorbed oxygen in the electrode. The interaction of the sp^2 orbitals of the oxygen molecule with the d_2 orbitals of the transition metal involve an end-on interaction with a partial charge transfer, changing the oxidation state of both metal and oxygen species and forming peroxide intermediates. Further reduction of oxygen requires the rupture of the O-O bond through the formation of peroxide free radicals that can go under an additional 4-electron reduction to form water molecules, or by 2-electron pathway to produce peroxide [32].

Finally, the Bridge model is based on the lateral adsorption of oxygen by two active sites with partially filled d_{xz} and d_{yz} orbitals to form a bond with π^* orbitals of oxygen. In order to establish a bond with O_2 , a proper spacing between the two metal sites is necessary. Similarly to the Griffiths mechanism, the formation of water molecules results from the oxidation and reduction of the electrocatalysts.

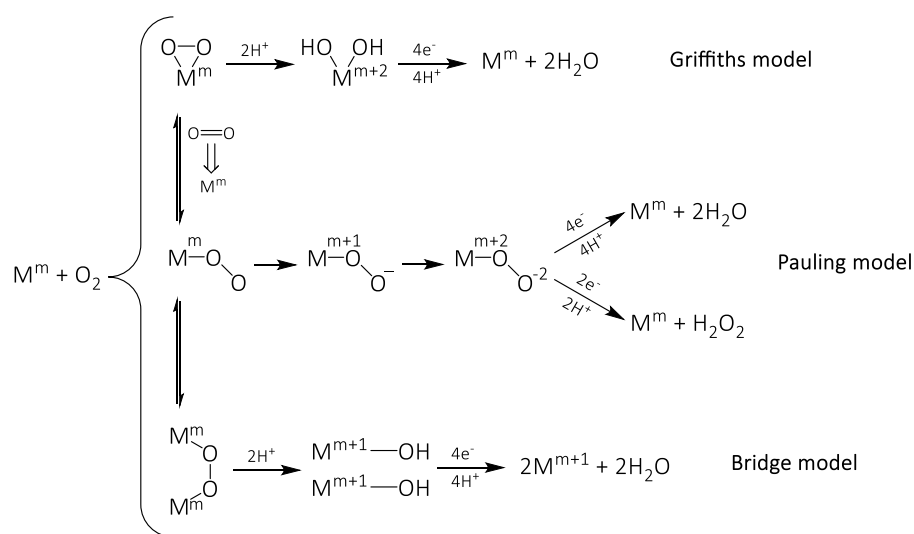


Figure 2.5. Representation of the proposed models for adsorbed oxygen molecule and the corresponding pathways to its reduction [32].

Based on the relation between the reaction pathway for oxygen reduction and the geometry of the compound and the previous interactions between O_2 and the metal, several authors proposed different schemes to describe the mechanism of ORR [28, 33]. The difficulty of the process of reduction of oxygen is the large number of reaction intermediates, several multielectron transfer, various series-parallel pathways and rate-determining steps (RDS). Among several investigations on how the reaction occurs in the electrode-solution interphase, Wroblowa *et al.* [34] proposed a modified scheme that describe the complexity of the ORR at the metal surface in aqueous solutions (Figure 2.6).

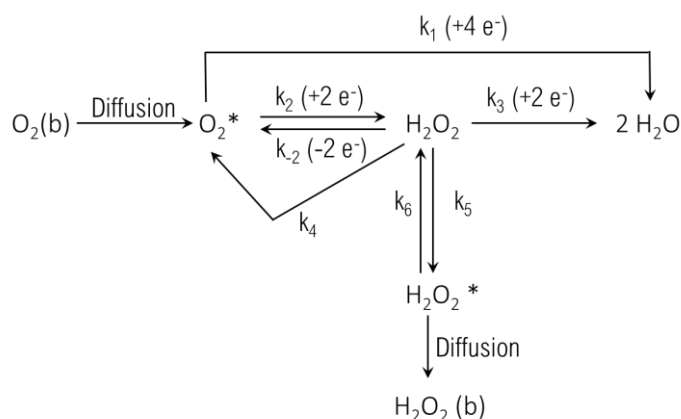


Figure 2.6. Proposed mechanism of the oxygen reduction reaction in an aqueous solution. The indices *, *b* and *a* designate bulk, vicinity of the disk electrode and adsorbed molecule, respectively. Adapted from [34].

In their report, Wroblowa and co-workers also proposed a criterion that assures unambiguous distinction between parallel-sequential mechanism (direct 4-electron or 2+2-electron reduction) and the sequential mechanism (in the absence of direct 4-electron pathway) [34].

2.2. NON-NOBLE TRANSITION METAL-BASED CATALYST FOR ORR

Most ORR cathodes electrocatalyst involve high-area carbon supports doped with other materials, such as transition metal-based compounds highly dispersed in the surface of the support that provides the enhancement of the electrocatalytic activity of the hybrid complex. Generally, carbon-based ORR catalysts can be divided into 3 types, based on their composition as metal-free heteroatoms (B, N, S, P)-doped carbon, metal/nitrogen co-doped carbon and carbon catalysts with nanoparticles encapsulated inside. This work focuses on the metal-free nitrogen-doped carbon and metal/nitrogen-co-doped carbon.

2.2.1. THE sp^2 CARBON SUPPORT

The structure and the environment provided from the support material is essential for the insertion of metal/macrocycle and nitrogen catalysts and, consequently, for the electrocatalytic activity of the material as a whole. As an electrocatalytic reaction, the ORR can be characterized by three important processes: mass transport, catalytic reaction and electron transfer, that are dependent on the structure, active sites and crystallinity of the catalysts [35]. Thus, among diverse conditions that carbon supports have to fulfil, the presence of a high density of active center in a large and crystalline surface area with porosity is of particular importance [6, 12, 36-42].

Graphene is composed by a single atom layer of sp^2 hybridized carbon arranged in a two-dimensional structure with a hexagonal lattice [43]. Since the nineteenth century, graphene has attracted considerable attention owing to its exceptional structure, physicochemical and mechanical properties, such as high electrical conductivity, mechanical strength, large specific surface area ($2630 \text{ m}^2 \text{ g}^{-1}$) and thermal and chemical stability [43-48]. Thus, graphene has become a promising candidate in the sector of catalysis, energy storage, electronic devices and functional films [44].

Currently, graphene and its derivatives such as graphene oxide (GO) and reduced graphene oxide (rGO) have been extensively studied as electrocatalysts for several reactions or as carbon support for loading transition metals, enzymes and oxides [49]. In the following subsection, a brief description of the key techniques to synthesize GO and GO-based materials is introduced (Figure 2.7).

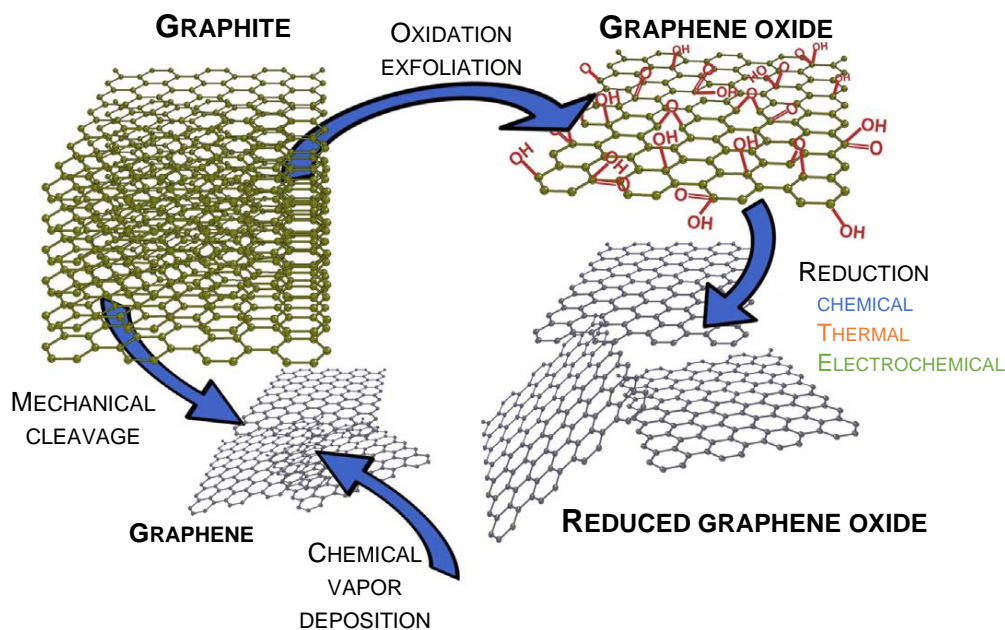


Figure 2.7. Schematic key techniques to synthesize graphene oxide and reduced graphene oxide. Adapted from [50].

2.2.1.1. PREPARATION OF GRAPHENE OXIDE

Graphene oxide is produced by several chemical and physical processes. Among these processes, chemical vapour deposition (CVD) and mechanical and chemical exfoliation of graphite are the most used techniques to obtain high quality graphene [47, 51-54]. As a chemical approach, Hummer's method has been widely used due to its easy operation conditions, good exfoliation and well-dispersed GO products [52, 55]. In this method, graphite (1 wt equiv.) is oxidized by a water-free mixture of concentrated sulfuric acid, sodium nitrate (0.5 wt equiv.) and potassium permanganate (3 wt equiv.), producing graphene oxide with highly oxygenated surface between layers [56, 57]. Although its common use, the major drawback of this synthesis method is the production of toxic gases (*e.g.*, NO₂ and N₂O₄) upon the oxidation of graphene by NaNO₃ [45]. Therefore, several reports on the synthesis of GO have been using the modified Hummer's method in order to obtain a higher degree of oxidation in an eco-friendly procedure [43-45, 51, 55, 58]. For example, one of the challenges of these improved methods is the proportions of the reactants by playing with the ratio of KMnO₄ and sodium nitrate [58].

2.2.1.2. N-DOPED GRAPHENE OXIDE

The doping of carbon materials with heteroatoms has proven to be a successful methodology to modify physical and chemical properties of carbon by introducing new elements with different electronic structures that provide more active sites and enhance the catalytic performance. Among several heteroatom-doping agents, nitrogen is considered to be an excellent candidate due to the atomic size similarity with the carbon atom, electronic configuration and charge density that is responsible for enhanced catalytic activity of N-doped carbon for ORR [17, 23, 59-61].

Rather than the number of atoms, the location of nitrogen atoms in the carbon structure is the most critical for the catalytic activity of N/C materials. Depending on the bonding features between the nitrogen and carbon atoms in N-doped graphene, there are three different N types: *sp*² quaternary N (or

graphitic-N) that results from the substitution of C atoms in the hexagonal ring; sp^2 pyridinic-N and sp^3 pyrrolic-N, located in the edges or defects of graphene, as shown in Figure 2.8.

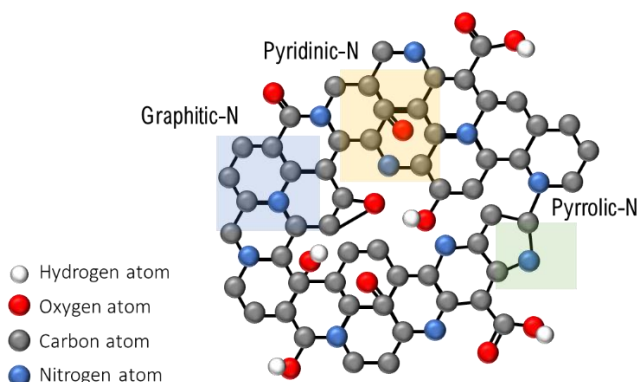


Figure 2.8. Schematic of N-doping graphene oxide and the location of different nitrogen atoms in the carbon structure.

The active sites of a N-doped carbon catalyst are thought to be essential for the enhancement of the catalytic activity of the material, not only because of the synergistic effect between N atoms and other transition metal species, but due to for the presence of pyridinic-N and graphitic-N groups. Several investigation consider both pyridinic- and N graphitic-N groups the most active centers responsible for the activation of O_2 and the enhancement of electronic conductivity [62-65].

The process of N-doping of GO gives rise to new properties of the carbon structure that are related to the high catalytic activity. Furthermore, the simultaneous nitrogen doping and reduction of GO is essential for the reestablishment of the π -network of the GO and increase the electrical conductivity of the material. Thus, numerous studies have shown that the morphology and atomic composition of the hybrid carbon material are determinant for the catalytic activity of the material [66-70] and these parameters are dependent on the synthesis methodology of N-doped GO.

2.2.1.3. METHODS OF N-DOPING AND REDUCING GRAPHENE OXIDE

The reduction of the obtained GO is an essential reaction in order to restore the electrical conductivity by the renovation of the conjugated graphitic structure [46, 48, 51]. Usually, this reduction reaction can be achieved through a **(i)** chemical pathway, by the addition of a reducing agent, such as hydrazine [52, 71] or sodium borohydride [71], **(ii)** thermal reduction [66, 67, 72, 73], **(iii)** electrochemical routes [74-76] and **(iv)** plasma treatment [77-82]. Among these, thermal reduction and plasma treatment are considered the more sustainable options due to their innocuity to the environment and low cost [72]. Moreover, several methods have been reported on the simultaneous nitrogen doping of the GO using both of the thermal [66, 67] and plasma reduction [68-70] (Figure 2.9).

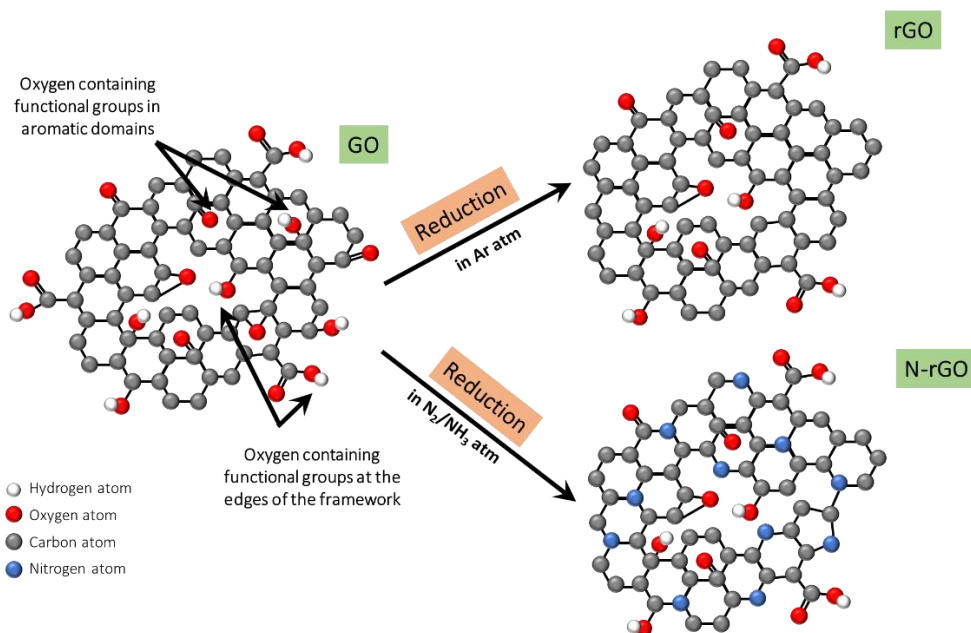


Figure 2.9. Schematic representation of the oxygen containing functional groups on graphene oxide and N-doping simultaneous reduction of graphene oxide.

Thermal reduction is a highly effective method for reducing graphene using temperature as an important condition for the degree of reduction and porosity (*e.g.* temperatures below 500 °C and above 750 °C give rise to C/O ratio < 7 and > 13, respectively) [66, 72]. Thermal reduction and simultaneous N-doping of GO have been a subject of several investigations due to its applicability in electronic and energy devices and catalysis. One of the most popular thermal annealing was reported by Li *et al.* [67], in which the GO thermal annealing was performed in the presence of 10 % NH₃/Ar atmosphere from room temperature to 1100 °C. As expected, the NH₃ annealing of GO resulted in the N-doping of the graphene material (3 to 5 % N between 300 and 1100 °C) and the reduction of GO is proved with the low oxygen levels in rGO [67]. Moreover, XPS analysis of control GO (reduced in H₂ below 500 °C and then reacted with NH₃ at 900 °C) suggested that oxygen groups might be essential for the formation of C-N bonds and to afford N-doping [67].

Plasma is often considered to be the “fourth state of matter” because its characteristics are significantly different from the other three states, specially due to its mixed composition of electrons, ions, neutral particles and excited molecules [83-85]. Such excited species in plasma result in an exceptional intrinsic reactivity that allows high-surface selectivity, efficiency and conservation of the material’s framework [85]. Nitrogen non-thermal plasma simultaneous reduction and N-doping have been widely applied in carbon materials as an eco-friendly and energy-saving methodology. Recently, several works have been reported on N₂ or NH₃ plasma for reduction and N-doping GO. Zhang *et al.* [68] described a simple method to synthesize Fe,N-doped graphene via a modified Hummer’s method and atmospheric pressure NH₃ plasma treatment. XPS spectra suggested that the plasma treatment created edges on the graphene structure with the formation of pyridinic N (68.19% of the total N content), that are the most active N species towards ORR; Moreover, BET surface area analysis pointed out an extra-exfoliation of the GO due to NH₃ plasma [68]. In another work, Lee *et al.* [70] demonstrated the effects of low-pressure NH₃ plasma on the doping and reduction in GO. XPS analysis of synthesized rGO indicated graphitic N and pyridinic N contributed to the formation of C-N bonds in the doped graphene and the introduction of *sp*³ defects was confirmed by Raman spectroscopy [70].

It is also possible to reduce GO in the presence of another gas, such as H₂ or Ar that can be applied in large-scale production of rGO (Figure 2.9) [72, 73, 86]. This method also reveals intrinsic high number of surface defects due to oxygen-carbon bonds [86] which proves the reduction of GO.

2.2.1.4. N-DOPED GRAPHENE AS ELECTROCATALYSTS FOR ORR

N-doped carbon materials have been considered promising metal-free catalysts for ORR because of their low cost, high ORR activity and durability [87]. Therefore, extensive research of reduced graphene oxide doped with heteroatoms has been done on the addition of nitrogen atoms as active sites for ORR [87-90]. Inspired on the synergistic effect of the combination heteroatoms and carbon structures, recent investigations of N-doped carbon materials have demonstrated high onset and half-wave potentials in alkaline and acidic media, as shown in Table 2.1.

One of the techniques for N doping materials is to take advantage of a high temperature treatment under nitrogen/ammonia flow to simultaneously dope and reduce carbon materials. Dong *et al.* [87] described the synthesis of a N-doped reduced graphene oxide material, through the preparation of graphene oxide by a modified Hummers' method which was then subjected to an ammonia flow at 750 °C for 2 hours. The resulting material with few layers exhibited an onset and half-wave potential of 0.947 V and 0.832 V vs. RHE, respectively, that is comparable to the activity of commercial Pt/C (20 wt % Pt). These results can be explained by the arrangement of the electronic structure of the graphene oxide, modifying its electron donor properties that improves ORR activity [87].

Similar results were reported by Zhang *et al.* [90], in which the carbonization under N₂ atmosphere of a biomaterial (chitosan) allowed the synthesis of a large specific surface area with a high doped pyridinic-N content material, denoted NC-*x*. The synthesis is based on the mixture of chitosan and ferric nitrate, Fe(NO₃)₃, or titanium dioxide, TiO₂, followed by a heat treatment under N₂ atmosphere and at 800 °C, and an acid washing, as shown in Figure 2.10(a). The main goal of adding Fe(NO₃)₃ or TiO₂ is to create a porous structure that is revealed after pyrolysis and acid washing. From the polarization curves obtained, the ORR onset potential of NC-1, NC-2 and NC-3 was 0.92 V, 0.75 V and 0.95 V vs. RHE, respectively. The NC-3 catalyst is considered the most active among the three, pointing out a higher ORR activity due to the synergistic effect between the large surface area and pyridinic-N content. Furthermore, the number of electrons calculated by K-L plots was 1.5-1.6, 1.32-1.4 for NC-1 and NC-2, demonstrating a 2-electron reduction of oxygen, while NC-3 exhibited a 4-electron pathway with 3.6-3.9 electrons transferred.

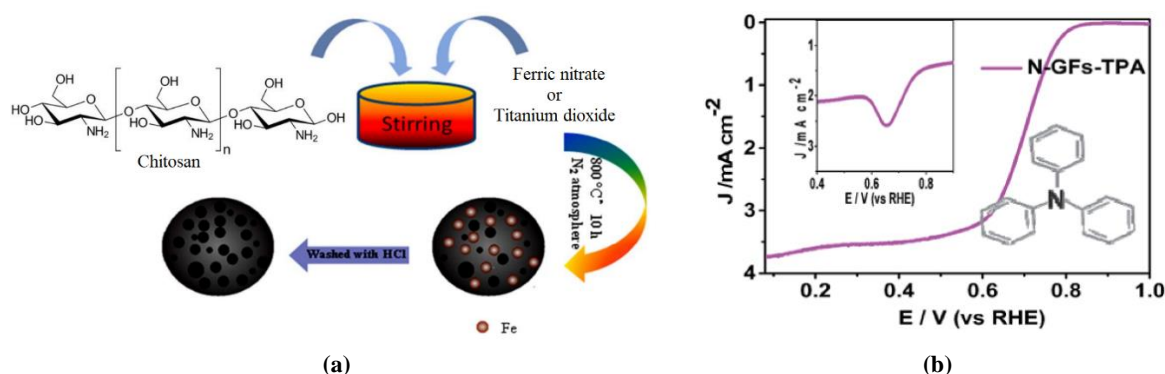


Figure 2.10. (a) Schematic representation of the synthesis of NC-2 and 3. The synthesis approach of NC-1 is similar to NC-3 except that no ferric nitrate and titanium dioxide was added. Adapted from [90]. (b) Polarization curve of N-GFs-TPA electrocatalysts in O₂-saturated 0.1 M HClO₄ solution, at 10 mV s⁻¹ [89].

Instead of using directly the N₂ pyrolysis to dope the carbon material, Li *et al.* [88] and Lu *et al.* [89] produced N-doped carbon catalysts by the chemical reaction of materials containing amino functional

groups and a carbon material. Li *et al.* [88] demonstrated the synthesis of a ORR highly efficient N-doped electrocatalyst in acidic media, based on triphenylamine and carbon nanotubes (Figure 2.10(b)). The ORR onset potential and half-wave potential reached 0.82 V and 0.67 V vs. RHE, respectively, in 0.1 M HClO₄, which is 50 to 100 mV more positive than the previous reported N-materials. In alkaline media, the E_{onset} and E_{half} results were slightly more positive, 0.97 V and 0.78 V vs. RHE, respectively. Similar results were obtained for N-G-1000, with an onset potential of 0.981 V vs. SCE, in alkaline medium (Figure 2.11(a)) [89]. The origin of the high activity of these compounds may be assigned to the synergistic tuning of N and C atoms for the electronic structure. Figure 2.11(b) shows the proposed mechanism of the ORR in N-G material, verifying the different contributions of N-types as catalytic centers, although the role of nitrogen in the catalysis of ORR is controversial [89].

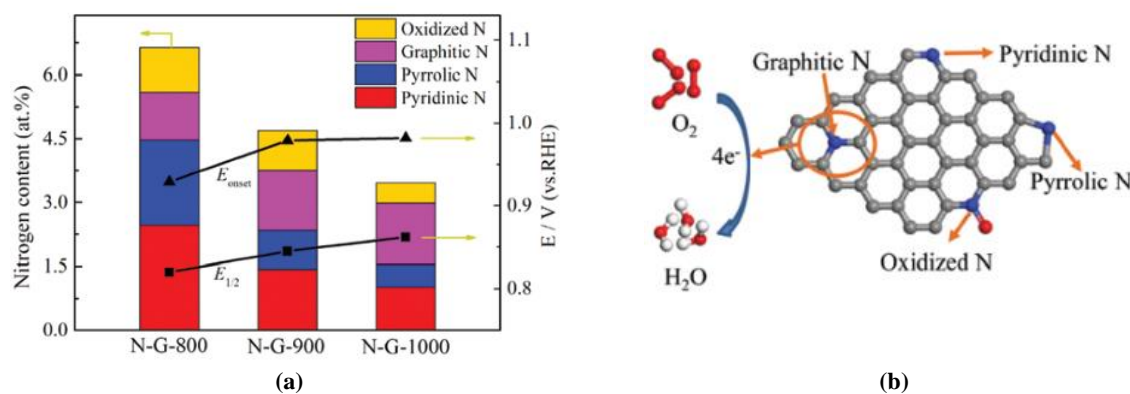


Figure 2.11. (a) Comparison between onset and half-wave potentials of N-G-800, 900 and 1000 catalysts and (b) the proposed ORR mechanism scheme of N-doped graphene [89].

2.2.2. METAL/MACROCYCLE AND NITROGEN DOPED REDUCED GRAPHENE OXIDE

Non-noble transition metal-based catalysts are a highly efficient and sustainable alternative to noble metal electrodes for the reduction of oxygen due to their high activity towards ORR, possibility of acquiring multiple oxidation states and low cost. One of the most studied structures based on non-noble transition metals are metal oxides owing to their high efficiency towards oxygen reduction [61, 91-98]. These materials have been the hotspot of several investigations because of their environmental abundance, high and various oxidation states and excellent thermal and chemical stabilities [21, 99]. Despite the excellent electroactivity properties of metal oxides electrodes, atomic dispersion of transition metal species is a more promising method that takes advantage of their unique hierarchical structure to increase active site exposure, in order to obtain maximization of exposure of the atom [100-103]. Thus, the synthesis of new cathodes based on atomically dispersed particles (as low as 1 at %) is the main key for the development of innovative and more efficient electrocatalysts for ORR.

The controllable synthesis of metal and N co-doped conductive and porous carbon materials is a new strategy to improve the overall catalytic process for ORR by increasing the electrical conductivity and the surface area of the material, preventing conglomeration and instability [42, 104, 105]. The metal and nitrogen co-doping of the carbon support are essential to ensure superior catalytic behaviour due to the formation of nitrogen-coordinated metal sites that are embedded in the sp^2 carbon lattice or located at the edges of the graphene sheets.

Table 2.1. Summary of the synthesis of recent N-doped carbon materials with C, O and N atomic contents of the catalysts and the correspondent electrocatalytic activity. The potentials values correspond to the onset potential and half-wave potential values vs. the reversible hydrogen electrode (RHE) at 25 °C.

Catalyst	Precursors	Methods	C at %	O at %	N at %					Electrolyte	E _{onset} (V)	E _{1/2} (V)	Tafel slope/ mV dec ⁻¹	HO ₂ ⁻ yield %	n	Year&Ref.
					Total	Pyri-N	Pyrrro-N	Graph-N	Pyri-N-O							
N-rGO	GO	Pyrolysis under N ₂ atmosphere 750 °C	81.6	12.3	6.1	20.2	39.2	29.2	11.4	0.1 M KOH	0.947	0.832	118	–	Not given	2017, [87]
N-GFs-TPA	Triphenylamine; CNTs	Pyrolysis under Ar atmosphere	89.6	6.8	3.9	33.0	16.2	46.5	4.3	0.1 M KOH	0.97	0.78	91	11.5	3.77	2018, [88]
										0.1 M HClO ₄	0.82	0.67	100	20.4	3.59	
N-G-1000	GO; Urea	Pyrolysis under H ₂ /Ar (5%:95%) atmosphere at 1000 °C	89.1	7.44	3.46	29.25	15.29	41.54	13.92	0.1 M KOH	0.981	0.862	72	–	3.92	2018, [89]
NC-1	Chitosan; Ferric nitrate; Titanium dioxide	Pyrolysis under N ₂ atmosphere 800 °C; Acid washing	88.75	3.36	4.89	9.9	31.3	58.8	–	0.1 M KOH	0.92	–	–	Not given	1.5-1.6	2018, [90]
NC-2			18.83	64.54	9.4	–	–	100	–		0.75	–	–		1.3-1.4	
NC-3			56.31	32.11	11.58	100	–	–	–		0.95	–	–		3.6-3.9	

TPA – Triphenylamine
GFs – graphene foams
CNTs – carbon nanotubes

2.2.2.1. TRANSITION METAL DOPED REDUCED GRAPHENE OXIDE

The reduction of oxygen catalysed by atomically dispersed transition metals and nitrogen doped carbon (M-N/C) is an important technological reaction and several studies have shown the superior ORR electrocatalytic activity of transition metals, comparable to commercial Pt/C electrodes in acidic [12, 35-39, 101, 106-109], alkaline [6, 12, 18, 37-42, 105, 106, 109-119] and neutral media [120]. Among 3d transition metals, iron-, cobalt-, manganese- and copper- based materials have been identified as potential candidates for the oxygen reaction because of their high activity, long-term durability, non-poisoning character by methanol, low cost and environmental friendliness [6, 105, 112, 114, 118].

In basic media, generally, M-N/C materials catalyse ORR by the transfer of 4-electrons with high selectivity and efficiency. However, in acidic solution, the electrocatalytic activity towards ORR is lower in nitrogen doped carbon materials due to protonation of nitrogen active sites and high overpotential of O_2/O_2^{*} from the first electron transfer and easier departure of peroxide species [37, 88]. Furthermore, the durability of the catalysts depends on the degradation by the oxidation of the carbon framework or corrosion, decreasing the catalytic sites and the ORR activity [38, 39]. Thus, one of the main challenges of this area is to develop a new material that catalyses the reaction in an effective and durable way, in acidic media.

Recently, several investigation groups have reported high catalytic performances of Fe-N based catalysts because of their strong interactions between the Fe and N species in the carbon framework [93], excellent stability during consecutive cycles and outstanding performance towards ORR in acidic [12, 35-39, 106, 109] and alkaline media [12, 18, 37-42, 106, 109]. Table A1 gives a summary of atomically dispersed iron and nitrogen doped carbon catalysts in acidic and alkaline solutions in terms of their precursors, synthesis and resulting ORR activity.

The optimization of mass transfer, charge transfer and catalytic reaction lies on the structure and active sites of complex Fe-N/C that are dependent on the methodologies of synthesis and on the iron, nitrogen and carbon precursors [35, 42, 106]. For instance, Ferrero *et al.* [109] synthesized Fe-N/C mesoporous carbon through carbonization of calcium citrate CCa as a sacrificial support. This strategy gave rise to a high surface area ($910 \text{ m}^2 \text{ g}^{-1}$) and large pore volume ($113 \text{ cm}^3 \text{ g}^{-1}$) materials doped with 1.12 and 6.86 wt % of iron and nitrogen, respectively [109]. Based on the performance towards ORR, CCa-0.37-10 (Fe : CCa = 0.37 and N:CCa = 10) catalyst exhibited a high ORR performance in acidic and alkaline media with high E_{onset} (0.74 and 0.91 V vs. RHE, respectively), $E_{1/2}$ (0.5 and 0.814 V vs. RHE, respectively) and kinetic current densities (4.92 and 13.6 mA cm^{-2} , respectively). Moreover, it was revealed relative low yield of peroxide produced (15 and 10 % respectively). It was ascribed the good catalytic activity to the combination of N-type functionalities with dispersed iron in the carbon framework [109].

Instead of using sacrificial support to prepare mesoporous carbon materials, Li *et al.* [35, 36] described a new synthetic pathway using directly a carbon material such as carbon nanotubes (CNTs). In their first report, a porous carbon CNT@Fe-N-PC electrocatalyst with high concentration of N-coordinated single iron atoms was prepared by pyrrole polymerization of CNTs, followed by Fe^{3+} adsorption and pyrolysis (Figure 2.12(a)) [36]. This synthesis not only allowed a uniform dispersion of Fe atoms (0.3 at %) and the formation of N-coordinated iron, but also the creation of pores during volatilization of zinc atoms that resulted in a highly porous catalyst ($0.88 \text{ cm}^3 \text{ g}^{-1}$) with a large surface area ($1180.2 \text{ m}^2 \text{ g}^{-1}$).

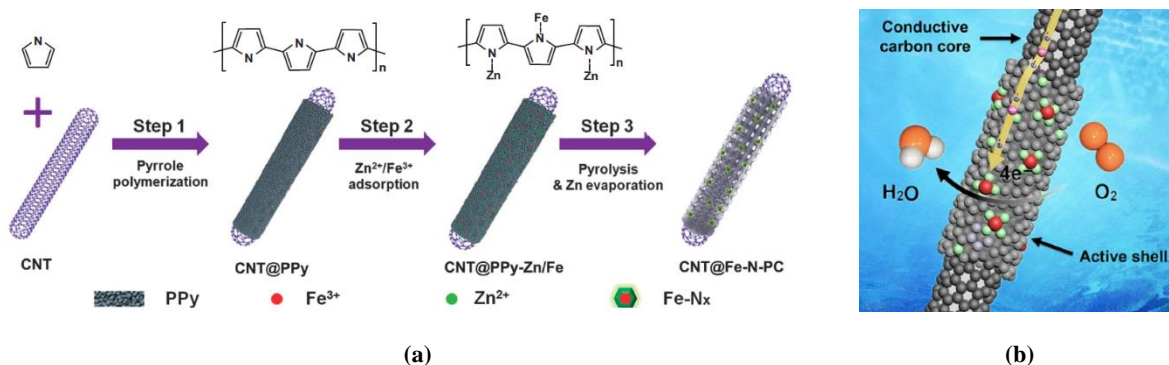


Figure 2.12. Schematic of (a) the synthesis of the electrocatalysts CNT@Fe-N-PC prepared by PPy polymerization on the CNTs, followed by Fe^{3+} adsorption and pyrolysis [36] and (b) the ORR catalysts characterized by a F-N-C core-shell structure [35].

The accommodation of Fe-N_x active sites in a porous material is considered to be a half step to expect a significant ORR electroactivity. As a result, the CNT@Fe-N-PC revealed an excellent ORR catalytic activity with high E_{onset} and $E_{1/2}$ (1.01 and 0.82 V vs. RHE, respectively), in an acidic media; Moreover, the peroxide formation yield at all potential is < 3 % [36]. In a later report, Li *et al.* [35] described an atomic isolation method used for the formation of one-dimensional core-shell structures ($1140 \text{ m}^2 \text{ g}^{-1}$) to accommodate high concentrated single Fe atoms (1.92 wt %) – the conductive shell, anchored on N-doped porous CNTs – the support core (Figure 2.12(b)). The CNT@Fe-N-PC exhibits similar ORR activity compared to the previous catalyst, even though higher electrical conductivity is observed in CNT@Fe-N-PC (higher Tafel plot) [35]. The high catalytic efficiency for ORR can be corroborated by the low peroxide yield (< 3 %).

Despite high ORR activity, the developed Fe-N/C electrocatalysts must produce a minimum quantity of peroxide species. However, it is known that iron-based carbon materials participate in Fenton reactions that are characterized by the reaction between iron ions and peroxide species to produce hydroxyl and hydroperoxyl radical species, causing toxicity, degradation and, eventually, cell failure [101, 107, 108]. Hence, it is imperative to find alternatives for iron-based carbon materials and it has been already reported that the ORR catalytic activity of M-N/C catalysts follows the order of $\text{Fe} > \text{Co} > \text{Mn} > \text{Cu} > \text{Ni}$ in alkaline and acid electrolytes [107].

Cobalt is one of the essential vestigial metals in the human body (1 to 2 mg) and its role in the production of neurotransmitters and red blood cells is indispensable for the good functioning of the organism [121, 122]. Therefore, cobalt atom and N co-doped carbon materials appears to be the most promising alternative of iron-based carbon materials in biofuel cells. Table A2 gives a summary of cobalt and nitrogen co-doped carbon catalysts in acidic and alkaline solutions in terms of their precursors, synthesis and resulting ORR activity.

Similarly to Fe-N/C catalyst, the morphology of Co-N/C complexes is essential to determine the optimization of the ORR process. Tang *et al.* [114] described the synthesis of cobalt and nitrogen doped carbon nanosheets (Co-N-PCN) using graphene oxide. The induced polymerization of aniline and pyrrole coated the GO surface with nitrogen-containing groups that allows the coordination of cobalt ions (Figure 2.13). This approach resulted in the formation of a highly porous and large specific surface area material ($450 \text{ m}^2 \text{ g}^{-1}$) that is essential for fast accessibility of reactants to the active sites and contributes for enhanced ORR activity in alkaline medium ($n = 4$; E_{onset} and $E_{1/2}$ are 0.90 and 0.82 V vs. RHE, respectively) [114].

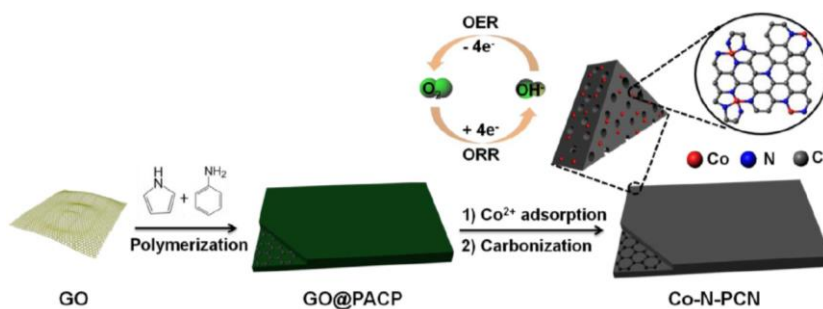


Figure 2.13. Schematic illustration of cobalt and nitrogen doped carbon nanosheets (Co-N-PCN) [114].

Regardless, Co-N/C catalysts produce substantial yield of peroxide species during ORR in acidic and basic media, suggesting that some (if not all) active site of Co catalysts are aimed for the promotion of 2-electron instead of 4-electron ORR. For instance, Cheng *et al.* [105] reported a new catalyst based on single cobalt atom incorporated in N-doped carbon nanofibers that exhibited excellent ORR activity ($n = 3.4$; E_{onset} and $E_{1/2}$ are 0.82 and 0.70 V vs. RHE, respectively). However, RRDE analysis revealed a high peroxide yield of ca. 30 % in basic media. Similar results were reported using silica nanoparticles as hard template ($n = 4.19$; $E_{1/2}$ is 0.82 V vs. RHE, respectively, and H_2O_2 yield 15.8 %, in 0.1 M KOH) [111], cobalt amino acid chelate ($n = 3.84$; E_{onset} and $E_{1/2}$ are 0.93 and 0.81 V vs. RHE, respectively, and H_2O_2 yield 10 %, in 0.1 M KOH) [6] and MOFs ($n = 4$; E_{onset} and $E_{1/2}$ are 0.93 and 0.80 V vs. RHE, respectively, and H_2O_2 yield 5 %, in 0.5 M H_2SO_4) [107].

In contrast to Fe and Co-based materials, the production of peroxide species and their interaction with manganese ions is insignificant which encourages the development of Mn-N doped carbon materials towards ORR for biofuel cells. According to theoretical density function theory studies, Mn-N moieties in the carbon framework have shown higher ORR kinetic activity and stability relative to Fe-N materials in acidic medium (Table A3) [101, 108]. However, carbonization process of Mn-N materials triggers the formation of manganese aggregates that are unstable and inactive compounds, decreasing the density of active sites [101]. Such drawbacks can be overcome by the confinement of atomically Mn-N in the carbon framework (such as MOFs [101] and polymers [108]) which allows the dispersion of stable active sites and enhancement of ORR activity in acidic medium (Figure 2.14(a) and (b)). Both Mn-N/C catalysts exhibited high ORR activity ($E_{1/2}$ are 0.80 V and 0.78 V vs. RHE, with 4-electron reduction) and negligible peroxide yield (< 3 %).

Copper is another 3d transition metal characterized by its ability to complex with N-containing ligands to form Cu-N moieties that are essential for ORR activity. Recently, several works have reported on atomically dispersed Cu ions in alkaline medium [116-119]. The synthesized Cu-N/C catalysts exhibited satisfactory ORR activity with high onset potentials (0.883 to 1.029 V vs. RHE) comparable to Pt/C catalysts (Table A4) [116-119].

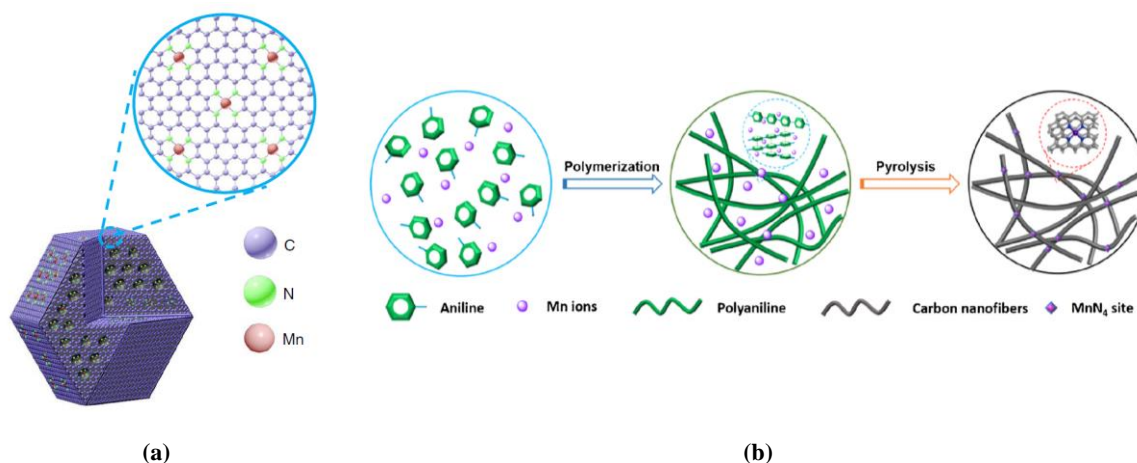


Figure 2.14. Schematic of (a) the synthesis of atomically dispersed Mn-N active sites in ZIF-8 (Adapted from [101]) and (b) Mn-N-C catalysts synthesized by the polymerization and pyrolysis of polyaniline hydrogel [108].

2.2.2.2. MACROCYCLE AND NITROGEN DOPED REDUCED GRAPHENE OXIDE

Nitrogen-chelated transition metal ($M-N_4$, $M = Fe, Co, Mn, Cu, \dots$) aromatic macrocyclic molecules are common complexes in nature and are known for their efficient catalytic activity on biological redox reactions that resulted in a growth of great interest especially on the biomimetic area [123]. The $M-N_4$ electrocatalysts contribution as cathodes on the ORR has been investigated and recent advances in the study of oxygen reduction on the $M-N_4$ molecules showed notable catalytic activity compared to metal-free macrocycles [124].

The interaction of aromatic macrocycles with the conjugated π electronic system of the graphene structure is essential to ensure the functionalization of the carbon material, preventing aggregation of GO sheets that would adversely affect the ORR electrocatalytic activity. Since Jasinski's reported work on the ORR electroactivity of cobalt phthalocyanine in 1964, extensive studies on metallophthalocyanines and porphyrins have been developed containing different central transition metals in neutral, alkaline and acidic media (Table A5) [103, 120, 123, 125-141]. Although metallophthalocyanines exhibit high activity towards the ORR, our state of art and study will be restricted to metalloporphyrins. Among the $M-N_4$ macrocycle structures, iron and cobalt as core metals of porphyrins have been considered the most electroactive metalloporphyrins cathode for ORR.

In previous reports on the development of new aromatic electrocatalysts for ORR, it has been shown that the incorporation of an axial ligand to the metal center in an aromatic macrocycle can enhance the catalytic activity of the material [137, 141]. In fact, the electrochemical study of Zagal *et al.* [142] on the ORR activity of vitamin B₁₂ in pyrolytic graphite boosted the interest on biomimicking vitamin B₁₂, which is highly active for ORR and promotes the 4-electron route whereas all the CoN_4 molecules have shown a 2-electron transfer pathway [141]. The high activity of vitamin B₁₂ has been assigned to the axial back ligand (Figure 2.15(a)) and, thus, the synthesis and ORR activity of FeP and CoP axially coordinated to pyridine anchored to carbon materials have been investigated [137, 138].

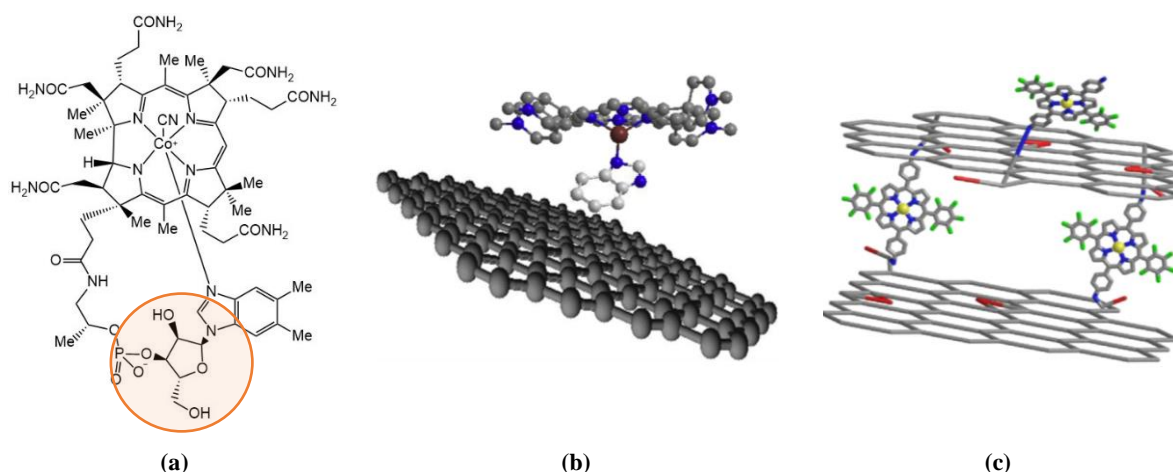


Figure 2.15. Schematic of (a) vitamin B₁₂ molecule, highlighting the axial back ligand, (b) FeTMPyP/BIm@rGO catalysts, emphasizing the interaction between the BIm and rGO [137] and (c) ERGO-Co-APFP catalyst [138].

In the report of Snitkoff *et al.* [137], the surface of reduced graphene oxide is firstly decorated with benzoimidazole (BIm) that is physically adsorbed, followed by the adsorption of the iron porphyrin (FeTMPyP) in the carbon structure (Figure 2.15(b)). It would be expected that only π - π interactions were in the basis of its adsorption, but actually EPR measurements showed that there was a direct linkage between the iron metal center of the porphyrin and the nitrogen atom from BIm [137]. The coordination of the axial ligand and the iron porphyrin on the rGO surface determines the ORR mechanism that shift from the predominant 2-electron to 2+2-electron reduction with FeTMPyP/BIm@rGO, because of the stabilization of reaction intermediates by the axial ligand that lowers the activation energy of 2+2-electron pathway [137]. In a similar work, You *et al.* [138] developed an electrochemical method for the functionalization of graphene oxide with a cobalt porphyrin (cobalt[5,15-(*p*-aminophenyl)-10,20-(pentafluorophenyl)porphyrin, CoAPFP) using EDC hydrochloride (*N*-(3-dimethylaminopropyl)-*N*'-ethylcarbodiimide hydrochloride) as an amide-coupling reagent, as shown in Figure 2.15(c). According to the RDE voltammograms, the reduction of oxygen is observed by a two-step mechanism for ORR that can be caused by synergistic effect of both carbon support and cobalt porphyrin [138]. This behaviour is also evidenced by the dependence of the number of electrons, n , on the potential, showing a higher n for ERGO-Co-APFP catalyst ($n > 3.8$) [138]. Similar results were reported using covalent triazine frameworks synthesized by the incorporation of cobalt porphyrin and subsequent thermalization $n = 3.92$ - 3.97 ; E_{onset} is 0.92 V vs. RHE in 0.1 M KOH).

Instead of embedding an axial ligand on the carbon structure, Wang *et al.* [140] reported a method of intercalating cationic MtTMPyP (Mt = Fe (III), Co(II) and Mn(III)) into negatively charged GO sheets by noncovalent bonds as π - π stacking and electrostatic interactions. The intercalation of metalloporphyrins in GO facilitates the electronic transfer between the two components of the catalyst, which is essential for the enhancement of ORR performance, in alkaline medium ($n = 3.88$; E_{onset} is -0.52 V vs. Ag/AgCl).

Taking advantage of the high ORR catalytic activity of vitamin B₁₂ and the particular features of single metal atom, Liu *et al.* [125] developed a simple strategy to doped carbon black with metallic Fe nanoparticles-doped vitamin B₁₂ that improves remarkably the ORR activity of the bimetallic catalysts ($n = 3.93$; E_{onset} is 1.00 vs. RHE). The outstanding ORR performance of Fe-VB₁₂/C material is associated to Fe-N_x and Co-N_x active sites and not only to one of the components of the catalysts. Furthermore, the introduction of iron is essential for the improvement of the ORR, not only for the catalytic activity of iron itself, but also for the interaction between iron species and Co-N_x active sites [125].

Experimental details and methods

The experimental details and methods used during this work are presented in this chapter. The presentation of all the chemicals used and the detailed protocol of the synthesis of graphene oxide (GO), as well as, the electrocatalysts based on the doping of GO with 2 or 10 wt % transition metal oxides (rGO/M 2 % and rGO/M 10 %) and metalloporphyrins (rGO/P 2 %) is presented. Next, the electrochemical characterization of catalysts is described, by means of hydrodynamic convective systems using rotating disk and rotating ring-disk electrodes, followed by Atomic Force Microscopy, BET analysis and further physical and elemental analysis of all the electrocatalysts. Finally, all the characterization and measurements set up are specified.

3.1. SYNTHESIS OF ELECTROCATALYSTS

3.1.1. CHEMICALS

Unless otherwise specified, all chemicals were obtained from commercial source, with analytical grade and used directly without further purification. All the aqueous solutions were prepared using ultrapure water from a Milli-Q system (18 M Ω cm at 25 °C). In the following description, the dry chemicals precursors used in the preparation of the **rGO/M 2 %** catalysts are presented: commercial graphene nanoplatelets (Steam Chemicals, Inc.), copper(II) dihydrate (CuCl₂·2H₂O, 99.0 %, R. P. Normapur), nickel(II) chloride hexahydrate (NiCl₂·6H₂O, 99 %, Janssen Chimica), manganese(II) chloride tetrahydrate (MnCl₂·4H₂O, 98 %, Sigma-Aldrich), cobalt(II) chloride anhydrous (CoCl₂, 97 %, Aldrich-Chemie), iron(III) chloride hexahydrate (FeCl₃·6H₂O, 99 %, Riedel-de Haën), rhodium(III) chloride hydrate (RhCl₃·H₂O, Sigma-Aldrich). For the preparation of **rGO/M 10 %** catalysts, the subsequent dry chemicals precursors were used (all purchased from Merck): iron(II) chloride tetrahydrate (FeCl₂·4H₂O, 99 %), nickel(II) chloride hexahydrate (NiCl₂·6H₂O, 98 %), cobalt(II) chloride hexahydrate (CoCl₂·6H₂O, 99.0-102 %), copper(II) chloride dihydrate (CuCl₂·H₂O, 99 %). Finally, the synthesis of **rGO/P 2 %** was achieved using the following dry chemicals: vitamin B₁₂ crystalline (VB₁₂, Roche), cobalt(II) meso-Tetra(4-sulfonatophenyl) porphine chloride (CoP, Frontier Scientific), iron(II) meso-Tetra(4-sulfonatophenyl) porphine tetrasodium chloride (FeP, Frontier Scientific) and manganese(II) porphyrin (MnP, synthesized in the University of Aveiro in the group of Professor José Cavaleiro, Appendix B).

In the following description, the liquid chemicals used in intermediate steps of the synthesis of both rGO/M 2 % and rGO/M 10 % are listed: sulfuric acid (H₂SO₄, 95.0-97.0 %, ACS), hydrogen peroxide (H₂O₂, 34.5-36.5 %, Sigma-Aldrich), 2-propanol (**i.** 99.7 %, Sigma and **ii.** \geq 99.9 %, José Manuel Gomes dos Santos, Lda.), Nafion (**i.** D520, Dupoit and **ii.** perfluorinated resin solution, 37 % water, Aldrich) and nitric acid (69.5 %, Carlo Erba).

The electrolyte solutions were prepared using potassium hydroxide (KOH, 85 %, Riedel-de Haën), phosphate-buffered saline (PBS pH 7.4, 8.0 mM Na₂PO₄; 1.14 mM KH₂PO₄; 138 mM NaCl; 2.7 mM KCl, Merck) and sulfuric acid (H₂SO₄, 95.0-97.0 %, ACS).

For the calibration of the RRDE, potassium hydroxide (KOH, 85 %, Riedel-de Haën) and potassium ferricyanide(III) ($K_3[Fe(CN)_6]$, Merck) were used.

3.1.2. CATALYSTS PREPARATION

3.1.2.1. SYNTHESIS OF GO

The graphene oxide (denoted as GO) was prepared by suspending commercial graphene (16 g) in sulfuric acid (400 mL). The mixture was stirred for 7 hours at 200 °C. The obtained suspension was transferred to two beakers, followed by its decantation using water; this process was repeated three times. Then, the obtained black paste was separated by filtration and washed with water until pH 5-6.

In order to oxidize the graphene structure, a piranha solution composed by a mixture of H_2SO_4 : H_2O_2 in 1:1 (1 L) was prepared, added to the GO residue and stirred for 3 hours at room temperature. Then, the resulting suspension was transferred to a beaker, decanted using water and filtrated and washed with water until pH 5-6. The obtained compound was a black paste (denoted as GO wet) composed by 82-77 % water and 23-18 % dry graphene. A schematic illustration the synthesis of the GO is shown in Figure 3.1.

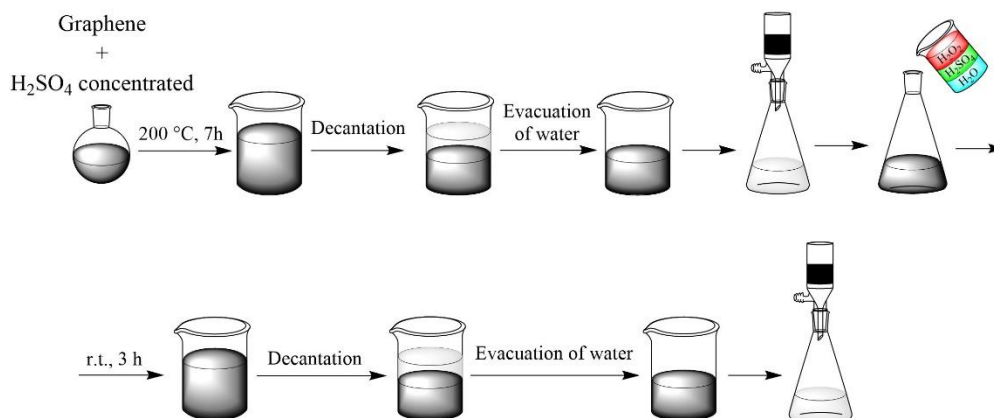


Figure 3.1. Schematic of the synthesis of GO via commercial graphene.

3.1.2.2. GO DOPING WITH NITROGEN AND TRANSITION METALS

Solutions containing metal precursors were prepared by the addition of 2 or 10 wt % of metal in dry graphene. Therefore, a calculated amount of several metal chlorides (Table 3.1) was dissolved in the minimum quantity of water.

Table 3.1. Calculated values for x wt % ($x = 2$ and 10) metal precursors used for doping of graphene.

Metal chloride	% metal on the complex	For 2 wt% in 2 g of dry graphene	For 10 wt% in 0.25 g of dry graphene
		m_{complex} (g)	m_{complex} (g)
$FeCl_3 \cdot 6H_2O$	20.6	0.194	0.121
$NiCl_2 \cdot 6H_2O$	24.8	0.161	0.101
$MnCl_2 \cdot 4H_2O$	27.8	0.144	0.090
$CuCl_2 \cdot 2H_2O$	37.3	0.107	0.067
$CoCl_2$ anhydrous	45.4	0.088	—
$RhCl_2 \cdot 6H_2O$	32.5	0.123	—
$FeCl_2 \cdot 6H_2O$	28.1	—	0.089
$CoCl_2 \cdot 6H_2O$	24.8	—	0.101

To a solution containing wet graphene suspended in water (200 mL) was added the metal solution and the resulting mixture was sonicated for 2 hours, followed by 1 hour stirring. After that, the solution was lyophilized for 2 days in order to dehydrate the product by sublimation.

Simultaneous nitrogen doping and reduction of the graphene oxide was performed by two methods: **(M1)** the resulting black powder was placed inside of an oven at 200 °C with argon flux for 24 hours; thereafter, the ammonia flux was introduced to have a mixture of ammonia and argon of 1:1. After the stabilization of the flux, the temperature of the oven was increased to 400 °C and so was the ammonia flux. Then, after 3 hours, the temperature was increased up to 700 °C and turned off after 7 hours of continuous flux; **(M2)** The obtained black powder was treated in a low-pressure plasma reactor using a N₂ atmosphere. The low-pressure plasma generator (Diener electronic GmbH + Co.KG) operated at 0.3 mbar while the microwave power was set at 10 W for 20 minutes. It must be noted that the M1 method was applied to all the rGO/M 2 % and rGO/Ni 10 % materials and the M2 was used in all the rGO/M 10 %.

For each 2 mg of catalyst, a solution of sulfuric acid 0.5 M (1 L) was added to the obtained powder and the resulting mixture was stirred for 1 hour at 60 °C. Finally, the produced black paste was separated by filtration and washed with water until pH 5-6. The obtained powder is denoted as rGO/M *x* % M_y, M = Fe, Co, Mn, Cu, Ni and Rh, *x* = 2 or 10 wt % and *y* is the doping/reducing method: M1 is the thermal reduction and M2 is plasma reduction.

A schematic illustration the synthesis of the rGO/M catalysts is shown in Figure 3.2.

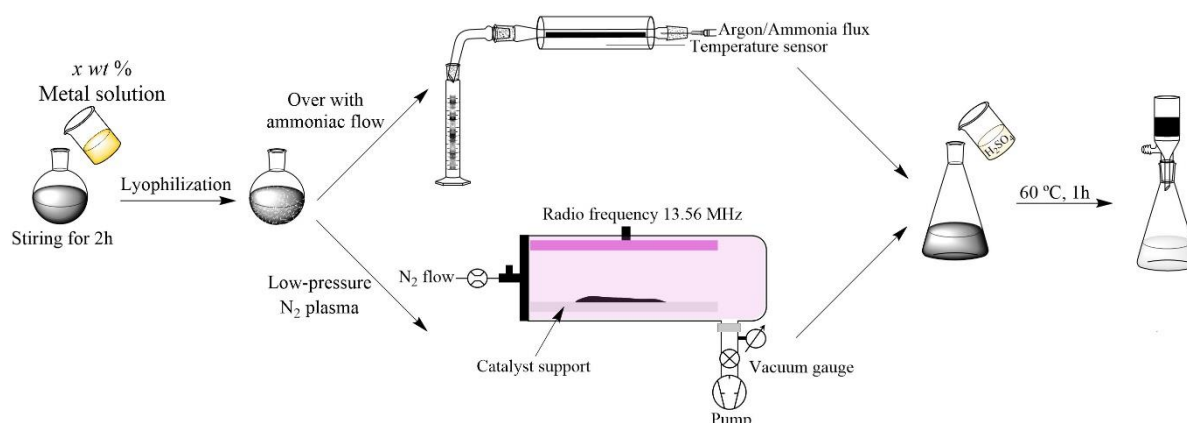


Figure 3.2. Schematics of the synthesis of rGO/M 2 and 10 % electrocatalysts catalysts.

3.1.2.3. INCORPORATION OF PORPHYRINS IN GO

The following procedure for the incorporation of porphyrins in GO is based on [125]. Solutions containing 2 wt % porphyrin and GO in water (20 mL) were dispersed uniformly and stirred overnight at room temperature (the calculated amount of porphyrin and GO is shown in Table 3.2). Then, the resultant powder was obtained through drying of the solution at 80 °C. Afterwards, the powder was pyrolyzed to 750 °C at a rate of 10 °C/min and then held at 750 °C for 2 hours in a ceramic tube, under nitrogen atmosphere. The final powder is denoted as rGO/P 2 %, P = FeP, CoP, VB₁₂ and MnP.

Table 3.2. Metalloporphyrins precursors used for 2 wt % doping of graphene. The values in brackets is the mass weighted of wet graphene.

Metal chloride	% metal on the complex	For 2 wt% in 2 g of dry graphene	
		m_{complex} (g)	$m_{\text{dry GO}}$ (g)
Cyanocobalamin (VB ₁₂)	4.35	0.9195	2 (11.0173)
Iron porphyrin	4.32	0.4630	1 (5.6024)
Cobalt porphyrin	5.74	0.0697	0.20 (1.1162)
Manganese porphyrin	6.34	0.0249	0.079 (0.4388)

3.2. CHARACTERIZATION TECHNIQUES

3.2.1. ELECTROCHEMICAL CHARACTERIZATION

The characterization of the electrochemical behaviour of the materials is an important aspect in the study of chemical systems by measuring signals such as potential, charge or current to study the electroactivity of the catalysts. In this subchapter, a briefly the potential sweep method, as well as the Nernst diffusion layer and the hydrodynamic method of convective diffusion systems using a rotating disk electrode (RDE) and rotating ring-disk electrode (RRDE) are described. Moreover, both Levich and Koutecký-Levich equations and their primary derivation are introduced.

3.2.1.1. POTENTIAL SWEEP METHODS: CYCLIC VOLTAMMETRY

The potential-time sweep techniques are used to monitor the electrode current as the electrode potential is varied between two limits at a specific scan rate. The resulting current-potential curve is known as voltammogram and it is useful for evaluating electrode processes. One of the potential sweep methods is *linear sweep voltammetry* (LSV) in which the potential sweeping occurs between the potential limits E_1 and E_2 , as shown in Figure 3.3(a).

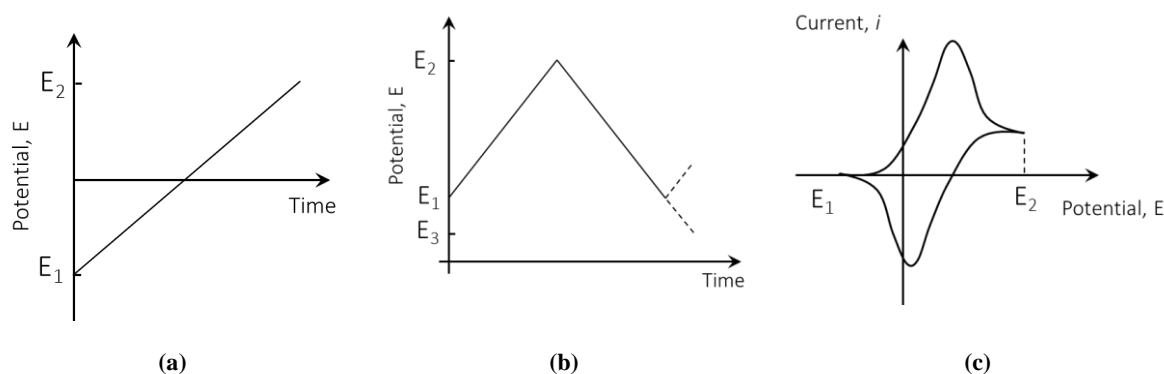


Figure 3.3. Potential-time profiles: (a) linear sweep voltammetry and (b) cyclic voltammetry and (c) a cyclic voltammogram for a reversible charge-transfer reaction.

Despite the simplicity of this process, the LSV technique is not applied to all electrochemical studies due to of the limited information, especially in preliminary mechanistic investigations. On reaching the potential E_2 , in *cyclic voltammetry* (CV), the potential sweep can be reversed back to potential E_1 or alternatively continued to E_3 (usually at the same scan rate) (Figure 3.3(b)) [143-145]. The obtained cyclic voltammogram for a reversible reaction is shown in Figure 3.3(c). The cyclic voltammetry has been the most used technique in primary studies of several investigation due to its facility of get an electrochemical “fingerprint” of the system.

3.2.1.2. HYDRODYNAMIC METHODS: CONVECTIVE DIFFUSION SYSTEMS

The electrodic events at the interface are considered to be the essence of electrochemistry and the transport of both electron acceptor and donors becomes an essential process to the continuation of the charge transfer. Thus, the electrochemical system is dependent on the ion transference in solution through mass transport processes and the charge transfer at the interface.

Among others mass transport processes, *convection* plays an important role in electrochemical systems and it is defined by the movement of species due to an external mechanical force. In such convective diffusion systems, the movement of the electrode relatively to the solution is used in order to achieve specific conditions such as the motion of electrodes for itself (*e. g.* rotating disk electrode, rotating wires and vibrating electrodes) or the pressure of the solution flow through the electrode surface, as shown in Figure 3.4. It should be noted that the convection is only effective if there is already a concentration gradient in the diffusion layer close to the electrode surface.

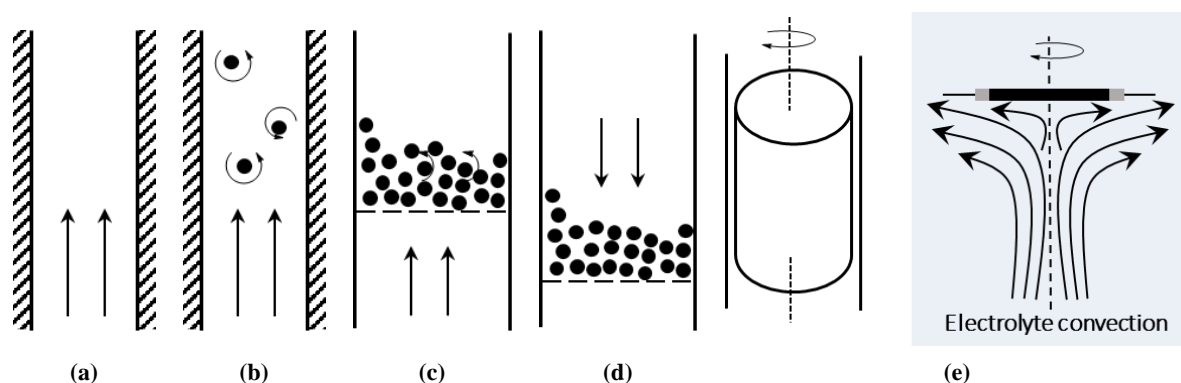


Figure 3.4. Convective diffusion systems (a) flow through channel, (b) flow through channel with turbulence promoter, (c) fluidized bed electrode, (d) packed bed electrode; (e) rotating disk electrode with a concentric tube and a schematic illustration of flow patterns created by the RDE. Adapted from [143, 145].

Methods involving convective mass transport of species in solution are designated by *hydrodynamic methods*. The advantage of this procedure is that a steady state is reached rather quickly and, in these conditions, all the changes in the electric double layer are not significant to the measurement. In order to consider hydrodynamic methods, it is essential to understand the design of the experimental element that can provide the transport of species from the bulk solution towards the electrode surface and how hydrodynamic methods provide information about the system.

The technique of the *rotating disk electrode* (RDE) is the most popular system among several techniques based on a stationary convective mass transfer and it is one of the few systems for which the convective-diffusion and hydrodynamic equations have been solved rigorously. Figure 3.4(e) shows a schematic illustration of the movement of flow patterns created by the RDE.

Consider that the mass transport follows a single and perpendicular direction to the surface in the x axis. Under stationary conditions in the electrolyte, and assuming only diffusion as transport process, the flux J_i involved per unit area and time is given by Fick's first law,

$$J_i = -D_i \frac{\partial C_i}{\partial x} \quad (3.1)$$

where D_i is the diffusion coefficient and $\partial C_i(x)/\partial x$ is the concentration gradient [144]. When the electrolyte begins to circulate to compensate density changes, a convective flux $C_i v$ is generated and the flux along the x -coordinate is given by Equation (3.2):

$$J_i = -D_i \frac{\partial C_i}{\partial x} + C_i v \quad (3.2)$$

Although the convection of the electrolyte is characterized by a laminar flow, the mass transport in the stagnant layer adjacent to the electrode is controlled by the concentration gradient in this layer. Thus, using Fick's law of diffusion, it is obtained:

$$J = -D \left(\frac{dc}{dx} \right)_{x=0} = \frac{j}{nF} \quad (3.3)$$

Consider the perturbation time long. The transport of molecules by convection dominates at the end of the diffusion layer δ , so that the concentration of ions reaches its initial bulk value within the distance δ and, over small distances from the interface, there is a linear variation of concentration (Figure 3.5). This is the theoretical basis proposed by Nernst in which is assumed that the continuous flux of material allows the separation of the zones for convection and diffusion: near the electrode surface ($x < \delta$), where the solution is stagnant, $\partial C_0 / \partial t = 0$, and only diffusion is observed; in the bulk solution ($x > \delta$), the process by convection dominates and the solute concentration is maintained at a value to its initial one at any time.

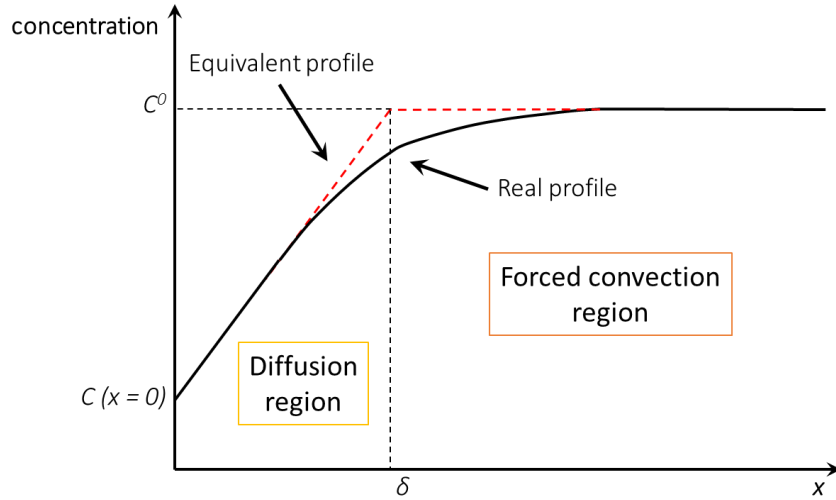


Figure 3.5. Steady state concentration profile for the electroactive species using Nernst diffusion layer model.

Assuming the extrapolation of the linear part of the concentration profile until it intersects the bulk value of the concentration at some distance δ from the interface [144]. At $x = 0$, the concentration gradient is given by $(c^0 - c_{x=0})/\delta$ and $(dc/dx)_{x=0}$ is replaced in Equation (3.3) to give.

$$J = -D \frac{c^0 - c_{x=0}}{\delta} = \frac{j}{nF} \quad (3.4)$$

In this approximation, one can consider that the diffusion occurs across a region parallel to the surface, *i.e.*, across a *Nernst diffusion layer* of effective thickness δ [144]. The diffusion layer is a concept that allow the simplification of the space variation of concentration in the interface; although there is concentration gradient that varies linearly with x , in the real case, the thickness of the layer is not defined, even in the steady-state conditions. In order to study the oxygen reduction reaction, a forced convection by the rotation of the electrode is applied; in this case, the movement of species due to convective transport is much faster than in natural convection and the concentration gradients extend over a much shorter distance δ [144]. Thus, the precise value of the diffusion layer thickness depends

largely on the effectiveness of forced convection, *i.e.*, the δ is much smaller as the angular velocity of the electrode is increased:

$$\delta = 1.61D^{1/3}\nu^{1/6}\omega^{-1/2} \quad (3.5)$$

where ν is the kinematic viscosity, ω is the angular velocity and D is the diffusion coefficient of oxygen.

Upon the electrochemical reaction at the interface ($x = 0$), the transport flux is described by the Fick's law of diffusion (Equation 3.6). Moreover, assuming that the concentration gradient reaches its maximum value for $c_{x=0} = 0$, it is obtained:

$$\lim_{c_{x=0} \rightarrow 0} \left(\frac{dc}{dx} \right)_{x=0} = \lim_{c_{x=0} \rightarrow 0} \frac{c^0 - c_{x=0}}{\delta} = \frac{c^0}{\delta} \quad (3.6)$$

The maximum concentration gradient corresponds to the maximum current density or *limiting current density*, denoted by j_L :

$$j_L = - \frac{DnFc^0}{\delta} \quad (3.7)$$

From (3.5) and (3.7), it is possible to obtain the *Levich equation*:

$$j_L = 0.62nFD^{2/3}\omega^{1/2}\nu^{-1/6}c^{\infty} \quad (3.8)$$

For a given redox reaction, j_L is considered to be the maximum attainable current density because the transport process in the electrolyte bulk is incapable of supplying the electron acceptor to the interface at a faster rate. Experimentally, the relationship between the measured current and the potential is shown in Figure 3.6, for the following equation:

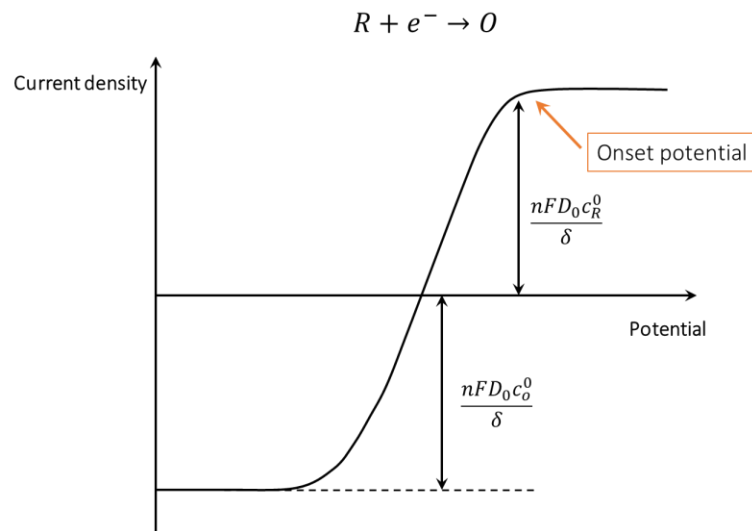


Figure 3.6. Complete I-E curves over a wide range of overpotentials.

As the potentials gets more negative than the equilibrium value, the reduction of O to R occurs and then increases in rate as the overpotential becomes larger, causing the surface concentration of O to decrease. Eventually, the surface concentration of O will approach zero, and mass transport will become the rate determining step in the sequence making up the overall electrode reaction. The current will reach a plateau at the given value by Equation (3.8).

Levich equation is the ideal response of a reversible mechanism, *i.e.* kinetically fast electron-transfer processes. However, for irreversible systems (kinetically slow), the electrode current i_K is defined as:

$$i_K = nFAk_f c^0 \quad (3.9)$$

in which, k_f is the heterogeneous rate constant for electron transfer [146]. Combining Equations (3.8) and (3.9), one can obtain the *Koutecký-Levich equation* that describes a mixed transport-kinetic control mechanism:

$$\frac{1}{j} = \frac{1}{j_K} + \frac{1}{j_L} = \frac{1}{j_K} + \frac{1}{0.62nFD_i^{2/3} \nu^{-1/6} c^0 \omega^{1/2}} \quad (3.10)$$

where, j_K is defined as the current density controlled by kinetic processes, *i.e.* in the absence of any mass-transfer effects. From the experimental data, the representation of $1/j$ vs. $1/\omega^{1/2}$ is a linear plot that allows the determination of the apparent number of transferred electrons from the slope and the kinetic current from the line interceptions with the origin.

Although the number of electrons calculated from Koutecký-Levich equation is an acceptable way of determining the ORR mechanism, the extent to which each of 2- and 4-electron reactions are involved in the electrode surface is usually accomplished by the rotating ring-disk electrode (RRDE) that measure the rate of formation of peroxide species on the disk (Figure 3.7.(a)). In order to detect peroxide, the ring electrode is set at a potential assigned to the oxidation of peroxide. An example of a cathodic current using a RRDE is shown in Figure 3.7(b).

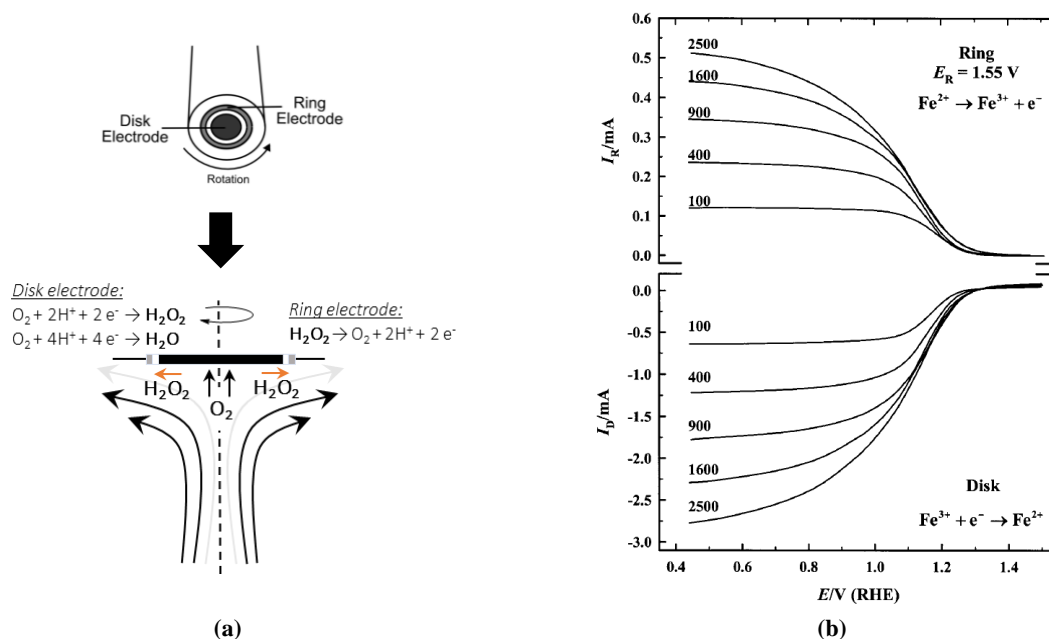


Figure 3.7. (a) Rotating ring-disk electrode system and (b) an example for a RRDE curve, in which the reaction in the ring and the disk are marked in the Figure [147].

Consider the current density measured on the disk j_D and its two contribution from 2- and 4-electron pathway, described by.

$$j_D = j_{D2} + j_{D4} \quad (3.11)$$

The ring current density j_R is obtained by the 2-electron transfer due to the formation of peroxide species in the disk electrode. Thus, the j_{D2} contribution is given by:

$$j_{D2} = \frac{j_R}{N} \quad (3.12)$$

where N is the collection coefficient that is characteristic of a RRDE system. In order to calculate the average number of electrons involved in the ORR process and, by rearranging in terms of n_e , it is possible to determine the average number of electrons transferred (Equation 3.13) and peroxide species yield generated in the disk electrode (Equation 3.14):

$$\frac{j_D}{n} = \frac{j_{2e}}{2} + \frac{j_{4e}}{4} \Leftrightarrow n = \frac{4j_D N}{j_R + j_D N} \quad (3.13)$$

$$\%H_2O_2 = \frac{200j_R}{j_R + j_D N} \quad (3.14)$$

3.2.1.3. KINETICS OF ORR

The quantitative description of kinetics at the interface of the electrode is given by the Butler-Vomer equation that relates the overpotential and the net current:

$$j = j_0 \{ e^{-\alpha n \eta F / RT} - e^{(1-\alpha) n \eta F / RT} \} \quad (3.15)$$

where j_0 is the exchange current density, η the overpotential, n the number of electrons transferred in the rate-determining step and α is the transfer coefficient (usually, $\alpha = 0.5$). The equation is composed by two terms that are assigned to the cathodic and anodic current, respectively. Moreover, in this equation, it is considered stirred solutions and/or low currents that defines the concentration in the bulk solution similar to the concentration in the surface of the electrode.

Due to the high irreversibility nature of the oxygen electrode reaction, the generated oxygen reaction currents at higher overpotentials ($|\eta| > 50$ mV) would more appropriately be described as the following derivation, in which the current density becomes an exponential:

$$e^{-\alpha n \eta F / RT} \gg e^{\frac{(1-\alpha) n \eta F}{RT}} \Leftrightarrow j_c = j_0 e^{-\alpha_c n \eta F / RT} \quad (3.16)$$

Rearranging Equation (3.16) and for a given constant temperature, a correlation between the exchange current density and the overpotential is obtained. The logarithmic version of (3.17) is known as *Tafel plot*:

$$\eta = a - b \log j \Leftrightarrow \eta_c = \frac{2.303RT}{nF\alpha_c} \log j_0 - \frac{2.303RT}{nF\alpha_a} \log j \quad (3.17)$$

3.2.1.4. EXPERIMENTAL SECTION

Catalyst ink was prepared by mixing *ca.* 2 mg of catalyst with 30 μ L of 5 wt % nafion and 1000 μ L of 2-propanol and the resulting mixture was sonicated until the complete suspension of the material. Before the deposition of the ink, the GC disk was polished to a mirror-like finish using alumina suspensions (5, 1 and 0.3 μ m, Buehler Alpha Micropolish) on polishing cloths (Buehler Microcloth) and then washed with ethanol and water. Then, a 5 μ L of the suspension was pipetted onto the rotating electrode and dried in air, resulting in a loading of catalyst of 142 μ g cm^{-2} .

Electrochemical measurements were performed using a Vertex.One (Ivium Technologies) potentiostat and a three-electrode cell employing a glassy carbon rotating disk electrode (RDE),

geometry area of 0.196 cm², EG&G, model 616) as working electrode, a platinum foil as counter electrode and saturated calomel electrode (SCE: 0.242 V vs. RHE for a saturated KCl solution at 25 °C) as reference electrode (Figure 3.8). The electrolyte solutions were nitrogen- or air-saturated phosphate-buffered saline (0.01 M PBS), 0.1 M sulfuric acid and 0.1 M potassium hydroxide solutions. Before the assay, the electrolyte was deaerated or aerated with pure nitrogen flow or air pump, respectively.

The measurements with a rotating gold ring-gold disk electrode (RRDE, gold disk geometry area of 0.416 cm²; gold ring area of 0.061 cm²) were performed using an EG&G model 366 bipotentiostat, coupled to an Oxford Electrodes Motor Controller and a Yokogawa recorder (A3 X-Y1-Y2, model 3023). A three-compartment glass cell was used with a platinum foil as counter electrode and saturated calomel electrode (SCE: 0.242 V vs. RHE for a saturated KCl solution at 25 °C) as reference electrode. The electrolyte solution was air-saturated 0.1 M sulfuric acid. Prior to and during RRDE experiments, the electrolyte was aerated with continuous air bubbling from an air pump.

Cyclic voltammetry curves were recorded at low scan rate of 10 mV s⁻¹ to reduce non-Faradaic current generated by the catalyst. ORR polarization curves of RDE and RRDE were obtained at a rotation of 400 to 2400 rpm. In the RRDE, the ring potential was set to 0.9 V vs SCE.

In this work, the onset potential, E_{onset} , for the materials was calculated considering the potential at which the current density reaches 5 % of the diffusion limiting current density and the half-wave potential, E_{half} , was determined by the difference of current density between -1.0 and 0.4 V vs. SCE in alkaline and neutral solutions and -0.8 and 0.4 V vs. SCE in acid media.

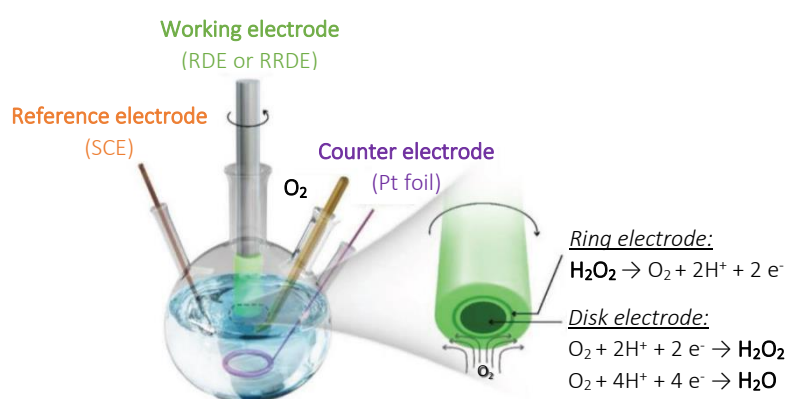


Figure 3.8. Schematic of a rotating ring-disk electrode in a single compartment cell. Adapted from [148]. Copyright 2018, American Chemical Society.

3.2.2. ATOMIC FORCE MICROSCOPY

3.2.2.1. INTRODUCTION TO SCANNING PROBE MICROSCOPY

Since his iconic talk entitled “There is Plenty of Room in the Bottom” in 1959, R. P. Feynman saw the potential of the arrangement of atoms on a nanoscale and the new properties that it would provide to materials at a time the technology for imaging and controlling matter has not been invented [149]. With the development in electronic microscopy and the acquisition of nanoscale images, nowadays Scanning Probe Microscopy (SPM) is a high-resolution technique that enables the acquisition of an image through the mapping of the surface with a small sharp probe. The SPM technique can be divided into Scanning Tunneling Microscopy (STM) and Atomic Force Microscopy (AFM), according to the operation of the probe. In STM, a fine metal tip is used as a probe; when it is applied voltage between

the tip and the conducting sample, a constant tunneling current is detected shortly before the tip and the sample come into direct contact (*ca.* 0.5-1 nm), along the surface in x and y directions. Although its high resolution, one huge drawback of STM is that it can only be used if the sample is conductive or semi-conductive due to tunneling current.

The AFM methodology is an alternative to STM due to its versatility regarding the material. This technique is based on the measurement of the force between the tip and the samples surface through repulsive/attractive atomic forces and van der Waals interactions, depending on the operation mode used. Figure 3.9 shows a schematic of the operation of an AFM. The force sensor consists of a laser focused to a spot on the back of a reflective cantilever; the beam is then reflected onto a split photodiode, which measures the position of the laser spot [150]. Briefly, the piezoelectric transducer moves the tip over the sample surface and the force that the transducer senses between the tip and the surface is reaches the feedback controller that manages the signal in order to maintain a fixed force between the tip and the sample [149, 151].

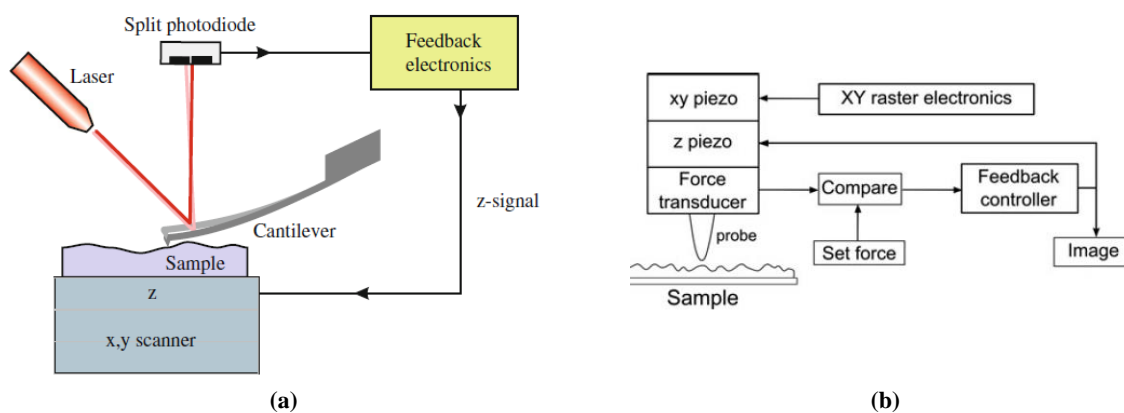


Figure. 3.9. (a) Schematics of atomic force microscopy apparatus [149] and (b) Qualitative sketch of the force between tip and sample as function of tip-sample distance and respective regimes [151].

3.2.2.2. AFM TOPOGRAPHIC MODES

Considering the qualitative plot of the interaction forces as a function of the tip-samples distance in Figure 3.10. At large distances between the tip and the surface of the sample, the *attractive forces* are negligible and the cantilever have zero deflection; further approach of the cantilever towards the surface leads to the first contact between the tip and the sample due to attractive forces; when the distance is very small, the interaction changes to *repulsive regime* and the tip and sample apply opposite forces [149].

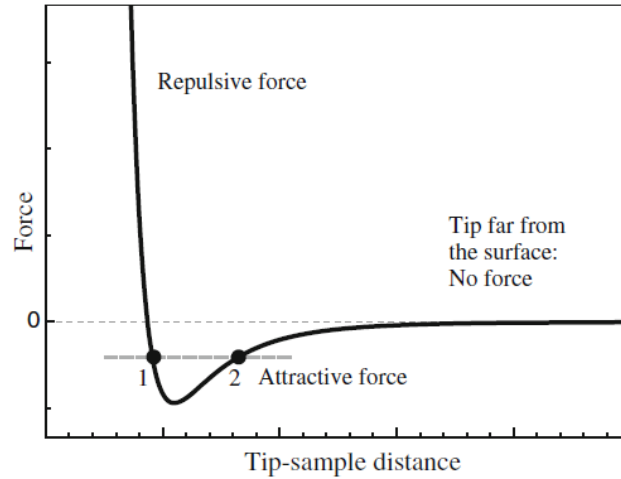


Figure. 3.10. Qualitative plot of the interaction force between the tip and the sample as a function of the distance to the surface [149].

Within the repulsive regime, it is assigned a ‘set-point’ in which a *static-mode* or *contact-mode* imaging occurs. In this operation mode, the tip and the sample are constantly touching each other and, the contact-mode is widely used, specially, for its extremely high resolution (Figure 3.11(a)). However, it has been suggested that contact-mode AFM is not appropriated for soft materials [151].

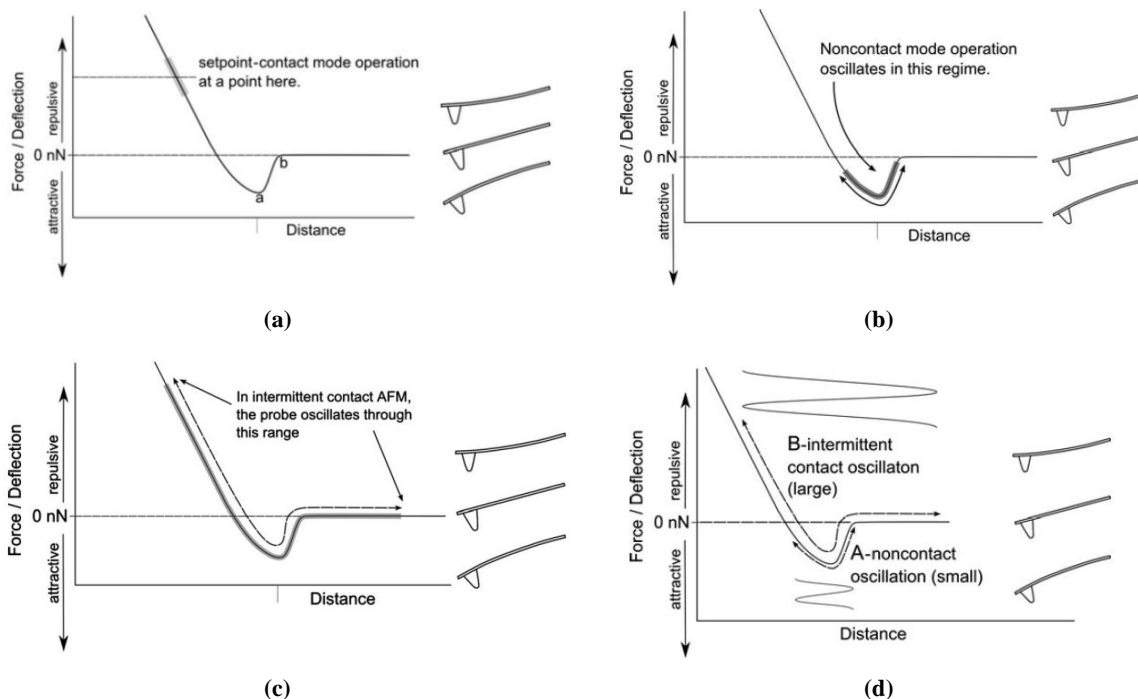


Figure. 3.11. Schematics of a force-distance curve showing (a) contact in a repulsive region, (b) non-contact AFM, (c) intermittent-contact regime and (d) different operating regimes for oscillating AFM modes: A – small amplitude and B – large amplitude of oscillation.

The atomic force microscope can also operate in *dynamic modes* that are mostly used due to its signal-to-noise benefits associated with modulated signals, obtaining images with a small probe-sample force and high sensitivity [151]. This operation mode is characterized by an oscillating cantilever that changes its resonant frequency upon the sample surface due to the interaction of the probe and the force field on the sample [149, 151]. For example, using a small oscillation amplitude, it is obtained practically maintain the cantilever in its equilibrium position in the attractive regime which corresponds

to the *non-contact AFM mode* (Figure 3.11(b)). During this operation, the tip has to be close enough to ensure high sensitivity, without touching the surface and jumping to the repulsive regime (although it is possible to observe changes in the oscillation amplitude and phase) [151]. Such effects are caused by attractive forces (*e.g.* van der Waals) between the tip and the surface. Non-contact AFM is widely used technique capable of imaging any material, from delicate samples, such as DNA molecules, biological materials to immersed samples in liquid. However, this AFM mode is limited to hydrophobic surfaces and the presence of a contaminated layer on most surfaces in air [151].

On the other hand, when the oscillation amplitude is increased, the distance between the tip and the surface increase to the extent that the interactions tip-sample are negligible, and the probe moves from non-interacting to attractive interaction and then repulsive regime, resulting in an *intermittent contact* (Figure 3.11(c)). This particular movement of the tip-sample interaction along the regimes has important implication on the intermittent contact mode because **(i)** it is possible to eliminate lateral forces; **(ii)** the tip can go through the contamination layer and **(iii)** some sample properties can be sensed due to the contact between tip and sample. The adjustment of the oscillation amplitude along the scan in air is the main feature of this mode, but also the possibility of analysis soft materials.

3.2.2.3. EXPERIMENTAL DETAILS

The morphology of the obtained samples was characterized by AFM and the topographic images were acquired in air by an atomic force microscope Nanoscope V coupled to a Multimode 8HR (DI, Veeco) using peak force tapping, with silicon nitride probes (TESP, Bruker) with a spring constant of ca. 0.4 N/m. 40 μ L of diluted samples were drop cast onto freshly cleaved mica or highly oriented pyrolytic graphite (HOPG) substrate, and imaged dried.

3.2.3. BET SPECIFIC SURFACE AREA ANALYSIS

The estimation of the total catalytic surface area available for gas- or liquid-phase reactants is essential in the interpretation of the catalytic behaviour of the material. In this subchapter, a brief description of the process of physical adsorption (or physisorption) of a vapor in the surface of a porous material and the development of the Brunauer-Emmett-Teller (BET) theory based on Langmuir isotherm method.

3.2.3.1. THE LANGMUIR ISOTHERM AND PHYSICAL ADSORPTION

The arrangement of atoms or molecules on the surface of a material through adsorption and desorption processes can be considered one of the main characterization techniques to study the texture of porous materials. The physical adsorption is defined as the contact of an adsorbable gas with a solid surface through intermolecular forces, *e.g.* van der Waals forces, as the temperature approaches the boiling point of the gas [152]. Usually, the presentation of adsorption data is done by *isotherms* that relate the quantity adsorbed against pressure, fugacity, activity or chemical potential at fixed temperature. When measuring adsorption isotherms, the normalized number of molecules adsorbed is substituted for the standard volume adsorbed in an ideal gas at standard temperature and pressure (STP).

The process of adsorption can be described by the *Langmuir adsorption* equation or isotherm. The Langmuir isotherm is considered to be the simplest model for the description of the equilibrium of a gas *A* on the surface sites *M*, at a constant temperature. The Langmuir adsorption isotherm results from the following assumptions:

1. The surface consists of a homogeneous two-dimensional array;
2. There are no lateral interactions between nearby molecules, so the fraction of occupied sites is independent on the number of molecules;
3. The activation energy for desorption is equal to the heat of adsorption, Q ;
4. The vapor phase behaves ideally;
5. It is not possible the formation of a multilayer surface.

Based on these assumptions, it is obtained the Langmuir adsorption isotherm on a uniform surface,

$$\Theta = \frac{aP\kappa}{x_m\nu e^{-Q/kT} + a\Lambda P} = \frac{bP}{1 + bP} \quad (3.18)$$

where, a is the probability of a molecule to stick on the surface, P is the pressure of the gas, κ the proportionality constant between flux and pressure for an ideal gas, x_m is the number of surface sites per unit area, ν is the frequency of vibration along the reaction coordinate that results in desorption, k Boltzmann's constant and T temperature and $b = a\kappa/(x_m\nu e^{-Q/kT})$ [152].

The Langmuir adsorption isotherm assumes that adsorption proceeds from zero up the saturation of the surface, in physical adsorption, in which the entire surface is composed by active sites. Intuitively, one would assume that the saturation of the surface would be the closest packing. However weak forces between adsorbed species and the surface and the free movement of these species contribute to the formation of more than a single layer – multilayer system. As the pressure increases, larger pores are filled, and the adsorbate gas condenses inside the pores, being possible to estimate the pore volume, size and distribution (Figure 3.12).

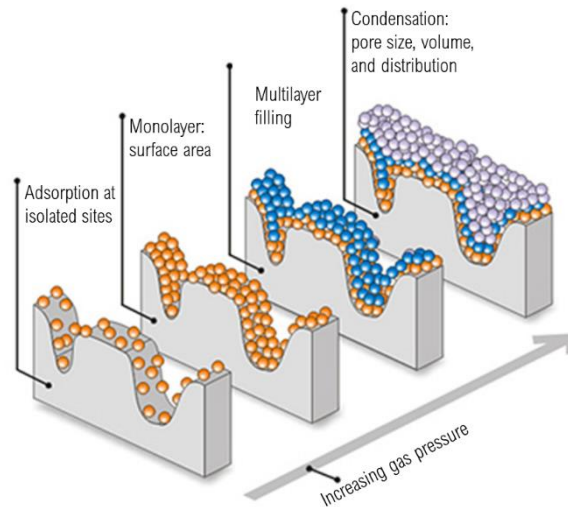


Figure 3.12. Surface area and porosity in a porous material. Adapted from <https://www.particletesting.com/surface-area/>

3.2.3.2. BET THEORY

The Brunauer-Emmett-Teller (BET) method is the most widely used procedure to study the surface area of porous materials by the multilayer adsorption model. The BET theory was developed to describe the simultaneous formation of mono and multilayer of adsorbed species, based on the following assumptions:

1. The samples' surface is characterized by the formation of multilayer;
2. "The energy of interaction between Nth and N+1st layers for N ≥ 2 and as N → ∞ is the same as the heat of condensation" [152], *i.e.*, the energy of interaction (heat of adsorption) between the adsorbing species and the surface is strongest in the first layer and then decreases as more layers are formed;
3. The attempt frequencies and the probability of adsorbing on the surface a_i for the 2nd and higher layers are the same as for the 2nd layer;
4. The volume of each adsorbed layer is similar which makes the surface flat;
5. At the saturation pressure, $p = p_0$, the number of layers is considered to be infinite, and the adsorbate density becomes identical to that of the bulk.

Based on the correlation between the rate of condensation and evaporation of adsorbed molecules in the Langmuir isotherm, in the BET theory it is possible to adapt that relation and express the formation of a monolayer considering the rate of adsorption and desorption. Therefore,

$$a_i P \kappa (1 - \Theta_i) = x_m \nu_i e^{-Q_i/kT} \Theta_i \quad (3.19)$$

in which Θ_i is the coverage of the fraction of empty site ($i=0$) and of those sites covered in the 1st layer and so on ($i = 1, 2, \dots$), Q_i is the heat of adsorption in i layer and x_m is the number of surface sites per unit area.

Considering the assumptions above, the BET adsorption isotherm is described as:

$$\frac{n}{n_m} = \frac{C p/p_0}{(1 - p/p_0)(1 + (C - 1) p/p_0)} \quad (3.20)$$

where n is the total number of molecules adsorbed and n_m is the total number of sites in the sample (monolayer capacity). The constant C ($C = \alpha/\beta$) is a parameter that reflect the differences between the formation of the first layer, $\alpha = \Theta_1/\Theta_0$, and the subsequent layers, *e.g.* 1st and 2nd layer $\beta = \Theta_2/\Theta_1$. In order to estimate the number of molecules in one monolayer, that is proportional to the surface area, it is convenient to rearrange Equation (3.20) to be easier to be plotted. Equation (3.21) is known as the BET equation and the plot of $(p/p_0)/(n(1 - p/p_0))$ versus p/p_0 , it is obtained a straight line with slope $C - 1/n_m C$.

$$\frac{p/p_0}{n(1 - p/p_0)} = \frac{1}{n_m C} + \frac{C - 1}{n_m C} p/p_0 \quad (3.21)$$

Thus, the surface area, SA_{BET} , and the constant C (from now on written as C_{BET}) are given in the terms of the slope S_{BET} and the intercept I_{BET} :

$$SA_{BET} = \frac{A_m}{S_{BET} + I_{BET}} \quad (3.22)$$

$$C_{BET} = 1 + \frac{S_{BET}}{I_{BET}} \quad (3.23)$$

where, A_m is the area that one molecule occupies on the surface.

3.2.3.3. EXPERIMENTAL SECTION

The BET adsorption isotherm was obtained using a Quantachrome NovaWin – Data Acquisition and Reduction, NOVA instruments with boiling temperature of nitrogen (77.3 K). The specific surface area and pore size were deduced from an analysis of the isotherm in the relative pressure range of 0.003 to 0.9. The specific surface area was estimated through the BET plot and the total pore volume was calculated from the amount of nitrogen adsorbed at a relative pressure of 0.94. The primary mesoporous volume (V_m) and external surface area (S_{ext}) were estimated using the *t-plot* statistical thickness method. This method is usually used on the study of microporous and mesoporous materials and determinates the volumes associated to each of the porous. This method is based on the use of standard isotherm which correlates the statistical thickness $t(P)$ of the surface with relative pressure [153].

3.2.4. FURTHER CHARACTERIZATION

The morphology and topography of the synthesized samples were analysed by AFM (as mentioned before). The structures of the samples were determined on an X-ray diffractometer (XRD, PANalytical EMPYREAN), using a Co $K\alpha$ radiation source ($\lambda = 1.789 \text{ \AA}$), in mode id fix divergent slit. The graphitization degree of the graphene catalysts was determined by unpolarized Raman spectra, recorded on a Renishaw inVia™ confocal Raman microscope at room conditions using a 633 nm argon laser light, with an incident power of 0.11 mW (1 % filter) and a 50x objective lens. The acquisition time of Raman spectra was set as 10 s and with 6 scans to get a first study and then the time was extended to 100-3200 s with 3 scans with a Raman shift range of 100 to 3500 cm^{-1} . The Fourier-transform infrared (FT-IR) spectra of the samples was recorded on a Nicolet™ iS50 - Spectrometer, Thermo Scientific™, in a nitrogen atmosphere, using potassium bromide pellets in the range 400 to 4000 cm^{-1} . An X-ray photoelectron spectrometer (XPS, PHI, Versa Probe II), with a monochromatized Al $K\alpha$ x-ray source (1486.6 eV) focalized to a spot of 100 μm and $\Theta = 45^\circ$ as an electron take-off angle was used to determine the surface elemental composition chemical states. Data were processed using MultiPak data reduction software. All spectra were calibrated with respect to sp^2 C1s signal at 284.3 eV and a background offset was applied before being deconvoluted. For the Inductively Coupled Plasma – Optical Emission Spectrometry (ICP-OES) analysis, the samples were calcinated at 800 °C and then dissolved in nitric acid and hydrofluoric acid in a platinum plate. The quantification of transition metals in the synthesized compounds were done in a Perkin Elmer Model 2000DV. The thermogravimetric analysis (TGA, Setaram TGA 93-12) was performed under O_2 atmosphere in a 1 bar chamber heating at an isocratic level at 30 °C for 30 min and then from 30 °C to 800 °C a rate of 5 °C/min.

Results and discussion

Since the birth of Green Chemistry almost two decades ago, the biggest challenge during the development of an innovative and efficient method of synthesis is the usage of green solvents. In this chapter, the method of synthesis of the prepared transition metal and macrocycle doped rGO by several physical, chemical and elemental techniques is discussed. Hereafter, the electrocatalytic characterization of the materials is presented and analysed by the RDE polarization curves; Moreover, the Koutecký-Levich equation enables the determination of the number of electrons transferred in the reaction in acidic, alkaline and neutral media that are confirmed by RRDE measurement. At last, the Tafel plots obtained by the polarization curves are addressed as the bridge between the obtained results and the proposed mechanism for ORR.

4.1. ANALYSIS OF THE SYNTHESIS OF GRAPHENE OXIDE

Commercial graphene nanoplatelets aggregates with a thickness of 5 to 10 nm and surface area of $750 \text{ m}^2 \text{ g}^{-1}$, shown in Figure 4.1, are used as starting carbon material of the synthesis described in Chapter 3. Despite their unique size and electrical and thermal properties, graphene aggregates present insufficient oxygen content ($< 2 \text{ wt } \%$) and low d -spacing between carbon layers.

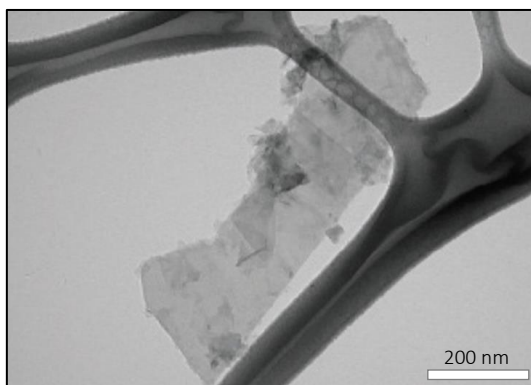


Figure 4.1. Transmission electron microscopy (TEM) image of nearly transparent graphene nanoplatelet aggregates. Adapted from [154].

One of the main keys to the synthesis of modified rGO electrocatalysts are, firstly, to obtain an exfoliated graphene with a wider d -spacing between layers about 3.41 \AA . Although van der Waals interactions between carbon layers are weak enough to allow their separation, attraction forces are the responsible for the collapse of several graphene sheets. Thus, for a successful exfoliation process, the oxidation of graphene layers is a method to overcome attraction forces by expanding the distance between layer. The addition of functional groups such as hydroxyl and epoxide to un-defected regions and carboxyl, carbonyl and phenol groups to the edges to the carbon framework allows the increasing of the d -spacing from 3.41 \AA to 7.0 \AA through the transformation of the planar sp^2 -hybridized carbon into a distorted sp^3 -hybridized structure [155, 156] and it is possible to obtain single layers of graphene, as shown in Figure 4.2.

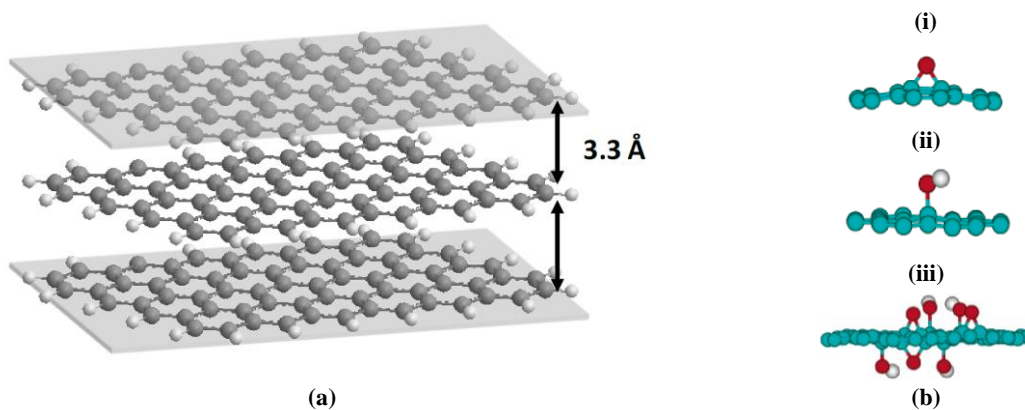


Figure 4.2. (a) Schematic representation of graphite, highlighting the thickness of the graphene layers [157] and (b) Atomistic model of two oxygen containing functional (i) epoxy (ii) hydroxyl groups and (iii) epoxy and hydroxyl groups on both sides of the graphene sheet. Adapted from [156].

The treatment of the extra-exfoliated graphene with a piranha solution ($\text{H}_2\text{SO}_4 : \text{H}_2\text{O}_2 = 1:1$) enables not only the creation of porosity on the carbon structure but also assures the oxidation of the carbon sheet. The formation of pores might result from structural instabilities of C-C bonds of the aromatic structure of graphene, due to the formation of reactive oxygen species [158]. The resulting material is known as graphene oxide (GO). Figure 4.3(a) and (b) shows an atomic force microscopy (AFM) morphologic image of GO dry and GO wet, respectively, highlighting the thickness of the graphene sheets.

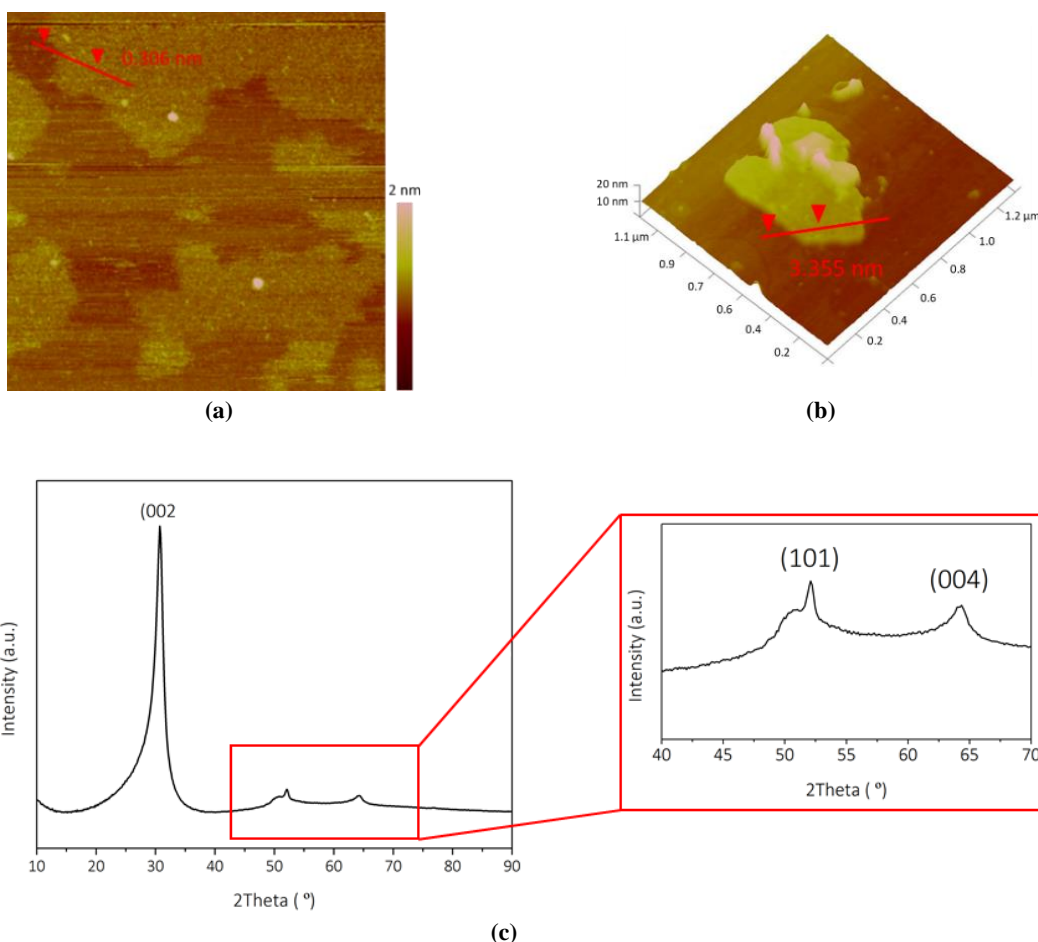


Figure 4.3. Morphologic image from AFM of (a) graphene oxide wet (550.8 x 550.8 nm), (b) graphene oxide dry (550.8 x 550.8 nm) and (c) X-ray diffraction patterns of graphene oxide and an expanded window between $2\Theta = 40$ and 70° (inset graph).

By AFM images, the measured thickness of GO wet (3.06 Å) is in agreement with the thickness of a single graphene layer (3.41 Å). The exfoliation and the thickness of the graphene is confirmed by the X-ray diffraction (XRD) pattern (Figure 4.3(c)). However, the same is not observed in the GO dry sample due to the collapse of graphene layer forming a multi-layered material of *ca.* 10 layers. Upon the drying of the GO wet, some water molecules between graphene layers are removed and there is the assembly and aggregation of several layers, due to van der Waals interactions. In order to understand the interactions on the GO wet, it was performed an analysis using a highly oriented pyrolytic graphite (HOPG) substrate, as shown in Figure 4.4(b), in which it is observed a well-dispersed nanofilm of graphene oxide with several aggregates in the surface.

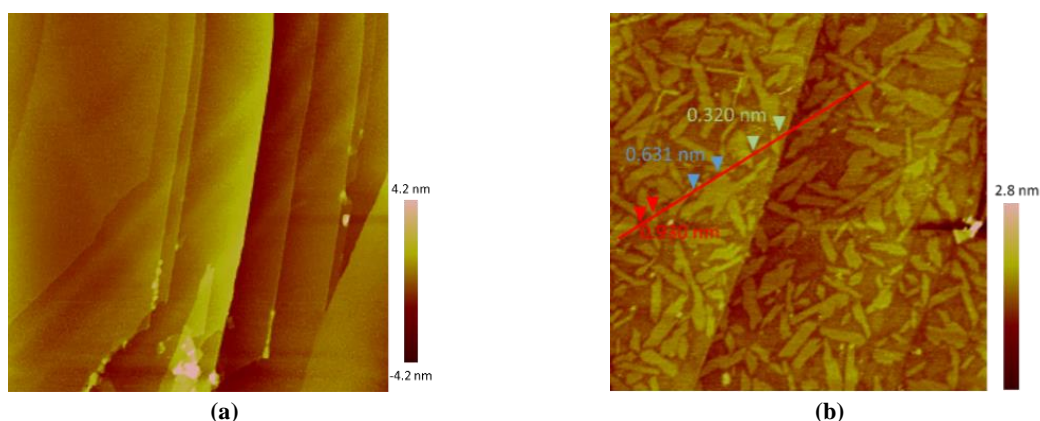


Figure 4.4. Morphologic 2D image from AFM of (a) HOPG and (b) graphene oxide wet in HOPG (1.1 x 1.1 μm).

The successful oxidation of the extra-exfoliated graphene is ensured by infra-red spectroscopy (FT-IR) (Figure 4.5(a)). A broad band at 3439 cm⁻¹ is assigned to O-H stretching vibrations from hydroxyl groups and water molecules. Moving forward, the IR peaks at 2978 and 2923 cm⁻¹ correspond to symmetric and asymmetric CH₂ stretching of the graphene oxide, respectively. Usually, these peaks are also present in graphite structure and correspond to impurities or chemical defects in the framework [159]. Then, the IR peak at 1637 cm⁻¹ is assigned to C=C stretches from unoxidized graphene, while the peak at 1584 cm⁻¹ corresponds to the vibration of non-aromatic C=C. Some function groups typically from oxygen-containing groups are visible at 1384 cm⁻¹ (C-OH), 1227 cm⁻¹ (C=O carboxylic acid), 1084 cm⁻¹ (C-O-C stretching), 1043 cm⁻¹ (C-O alkoxy) and 877 cm⁻¹ (epoxy groups).

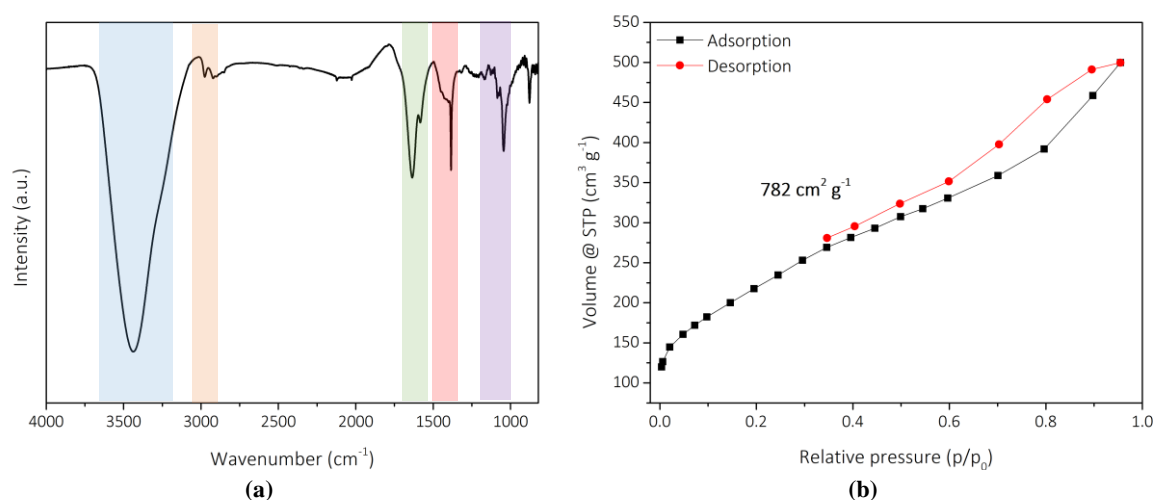


Figure 4.5. (a) FT-IR spectrum of graphene oxide, highlighting the presence of different oxygen containing functional groups and (b) N₂ adsorption-desorption isotherm of graphene oxide.

The specific surface of the synthesized graphene oxide was also analysed by nitrogen adsorption-desorption isotherm. Figure 4.5(b) shows a combined type I and IV hysteresis characteristic of the presence of micro and mesoporous structure. The obtained Brunauer–Emmett–Teller (BET) surface area for GO is $782 \text{ m}^2 \text{ g}^{-1}$, slightly higher than the value for commercial graphene nanoplatelets which implies the creation of porosity on the material that increased the surface area of GO. However, additional measurements are needed.

4.2. ROLE OF THE SURFACE STRUCTURE AND N-DOPED rGO ON ORR

In the previous section, the morphologic and structural analysis of the synthesis of graphene oxide was presented. After the synthesis of GO, the incorporation of 2 and 10 wt % transition metals, followed by the nitrogen-doping simultaneously reducing the graphene oxide were performed. Moreover, the incorporation of 2 wt % aromatic macrocycle on the surface of graphene oxide was also studied.

4.2.1. ATOMICALLY DISPERSED TRANSITION METALS IN rGO

Recently, several investigations have shown high ORR activity of iron and cobalt nitrogen doped carbon materials in neutral, alkaline and acidic solutions, although the performance of these electrocatalysts is unsatisfactory in acidic medium [6, 12, 18, 35-42, 105-107, 109-112, 114]. Thus, our experimental work is focused on the development of atomically dispersed iron and cobalt atoms on reduced graphene oxide for ORR in all the mentioned electrolytes. Moreover, it is also analysed the ORR catalytic activity of other 3d transition metals: manganese, copper, nickel and rhodium.

Upon the reduction of graphene oxide, the removal of some of the oxygen functionalities and other structural defects and the renovation of conjugated π -network are essential to ensure high catalytic activity towards ORR. Furthermore, doping carbon materials with heteroatoms, particularly nitrogen, is considered a suitable method for the incorporation of highly active sites for ORR performance (Figure 4.6). Thus, simultaneous reduction and nitrogen-doping of graphene oxide has been implemented as an alternative method that combines both of the reactions of interest. Here, a simultaneous reduction and N-doping of graphene oxide via thermal (method 1, M1) and plasma (method 2, M2) reduction is reported.

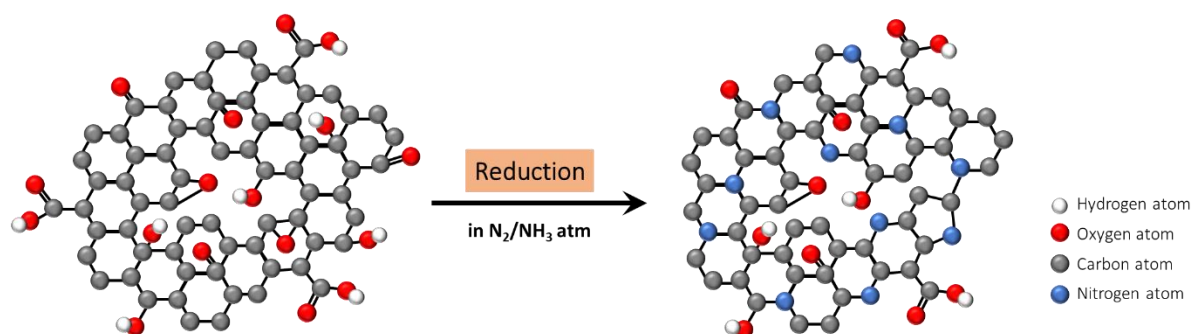


Figure 4.6. Schematic representation of the oxygen and nitrogen containing functional groups on reduced graphene.

The preservation of the carbon structure of graphene oxide after the 3d metals and nitrogen co-doping and reduction of graphene oxide is investigated to understand the process of simultaneous doping and reduction. Firstly, it is analysed the thickness of the graphene sheets and the homogeneity of the sample. Figure 4.7 shows an AFM morphologic image of rGO/M 2 and 10 wt %, M = Fe and Co with the corresponding thickness of the graphene sheets.

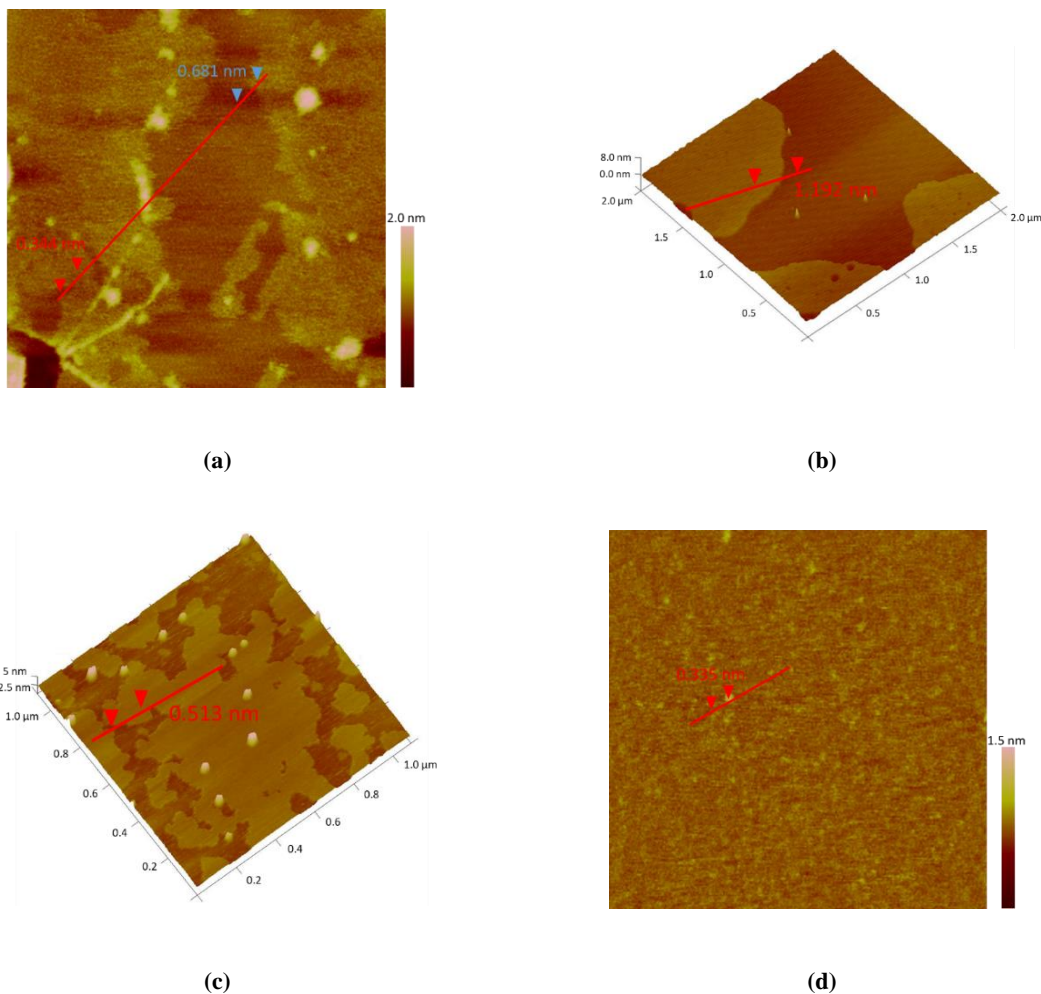


Figure 4.7. Morphologic image from AFM of (a) rGO/Fe 2 % (820.3 x 820.3 nm), (b) rGO/Fe 10 % (c) rGO/Co 2 % and (d) rGO/Co 10 % (830.8 x 830.8 nm).

Based on the AFM profiles obtained for modified rGO catalysts, it is observed a well-dispersed nanofilm of rGO-based catalyst composed by very small sheets of graphene. Concerning the agglomeration of the graphene layers, the thickness of the materials varies between *c.a.* 0.3 nm and 1 nm, which implies the collapse of some of the graphene layers. This could be explained by the reduction of oxygen containing functionalities that are essential for the separation of graphene layers.

The thickness of the materials estimated by AFM images is confirmed by XRD pattern, in which the main diffraction peak at $2\Theta = 30.7^\circ$, corresponding to the crystal plane (002), translates a d -spacing of 3.36 \AA (Figure 4.8). The two smaller peaks observed in the XRD pattern at $2\Theta = 52.1^\circ$ and 64.3° are assigned to (101) and (004) crystal planes.

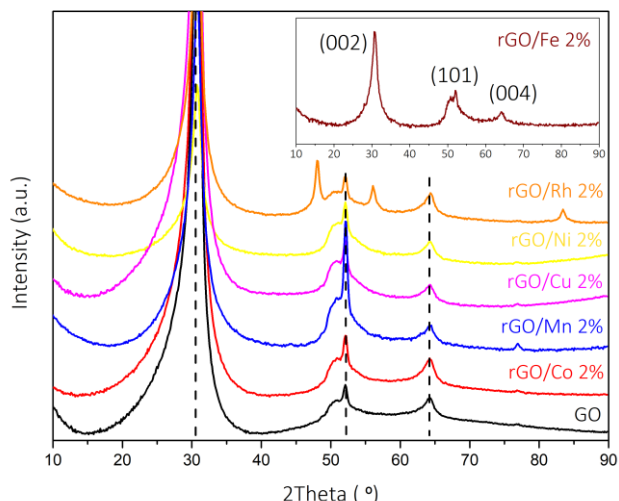


Figure 4.8. X-ray diffraction patterns of modified rGO electrocatalysts (inset graph of rGO/Fe 2 %).

In order to support the doping of reduced graphene oxide with transition metals and nitrogen, Figure 4.9 shows the FT-IR spectra of rGO/M 2 and 10 wt %. Similar to IR spectrum from GO, several oxygen containing functional groups are observed at *ca.* 3445 cm^{-1} , 2920-2975 cm^{-1} , 1384 cm^{-1} and 1043 cm^{-1} , assigned to O-H stretching vibrations from hydroxyl groups and water molecules, symmetric and asymmetric CH_2 stretching of carbon structure, C-OH and C-O alkoxy stretching, respectively. However, the intensity of these bands is lower than the one observed in GO spectrum. Furthermore, in both spectra of rGO/M, some bands of non-aromatic C=C (at 1580 cm^{-1}), C=O carboxylic acid (at 1227 cm^{-1}), C-O-C stretching (at 1084 cm^{-1}) and epoxy groups (at 877 cm^{-1}) are not observed, which can be due to the reduction of graphene oxide. The doping of amino functional groups in the carbon framework can be demonstrated by the peaks at 1634 cm^{-1} , assigned to stretching of C=N. Moreover, the wide band between 3664 and 3106 cm^{-1} can also correspond to the stretching vibration of N-H. The presence of transition metals inside of the carbon material is not observed in FT-IR spectra due to low quantity incorporated and sensitivity of the technique.

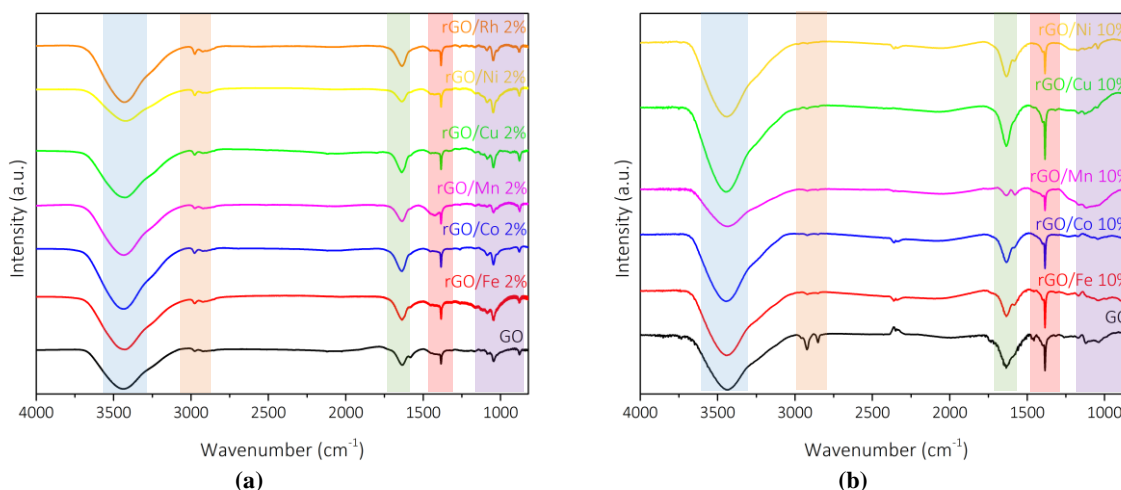


Figure 4.9. FT-IR spectra of (a) rGO/M 2 wt % under argon atmosphere from 4000 to 400 cm^{-1} and (b) rGO/M 10 wt % under air atmosphere, highlighting the presence of different oxygen and nitrogen containing functional groups, from 4000 to 1000 cm^{-1} .

The Raman spectra of a crystalline graphite derived material is characterized by the presence of two strong peaks centered at 1500 cm^{-1} and 2500 cm^{-1} designated D and G bands, respectively. The D-band reflects the sp^3 defects of disorder on the carbon structure, while the G-band corresponds to the

in-plane vibration of sp^2 carbon framework [42, 160]. The ratio of the intensities of D and G bands, I_D/I_G , is used to describe the graphitization degree, which is defined as the conversion of a pre-ordered carbon material into a three-dimensionally ordered graphitic structure material. In the context of ORR, the ratio I_D/I_G is an important parameter because it can be related to the catalytic performance of an electrocatalyst, *i.e.*, if a material exhibits a low I_D/I_G value, it presents a high graphitic degree due to the formation of an order structure. Figure 4.10 shows Raman spectra of graphene oxide and 2 and 10 wt % doped rGO. The ratio of I_D/I_G for the catalysts was calculated and is marked in the spectra.

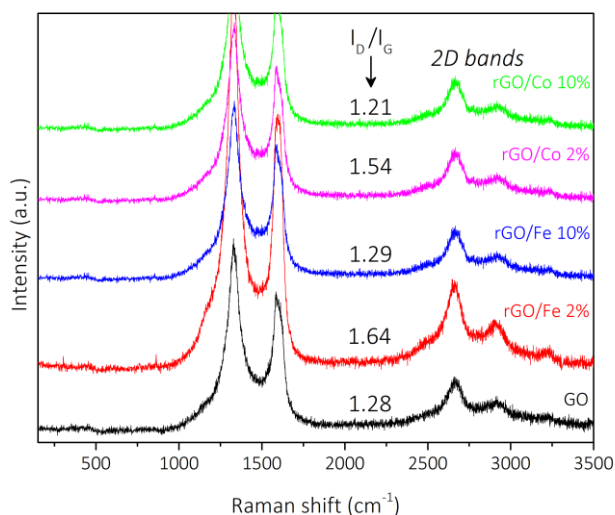


Figure 4.10. Raman spectra of graphene oxide and reduced graphene oxide doped with 2 and 10 wt % Fe and Co and corresponding ratio I_D/I_G .

According to Figure 4.9, the I_D/I_G values of GO and modified rGO catalysts are distinct, revealing different graphitization degree. Firstly, graphene oxide and rGO/Co and Fe 10 % show similar I_D/I_G values. This observation can be due to the low temperature plasma treatment that do not allow the organization of the graphene sheets. On the other hand, rGO/Co and Fe 2 % reveal higher I_D/I_G values, which is characteristic of a defected carbon material. The defects incorporated into the graphene structure are assigned to the doping with heteroatoms during the M1 treatment rather than the M2. Concerning the ORR, it has been already shown that the porosity of the material is essential for the high ORR activity as the diffusion of reactants and their accessibility to active sites are favoured. [161]. Thus, it is expected that the electrocatalytic activity of rGO/Co and Fe 2 % towards ORR is significative with a direct or indirect 4-electron pathway. In addition to the D and G bands, a couple of well-defined peaks centered at 2700 cm^{-1} can be assigned to 2D bands, characteristic of few-layered graphene-based materials.

Apart from the surface structure, the role of nitrogen and metal doping is also studied. The content and status of C, N and O were evaluated by XPS. Being a carbon material subject to an oxidation, it is predicted that both C and O elements are observed in all of the materials at 284 and 532 eV, respectively, as shown in Figure 4.11(a).

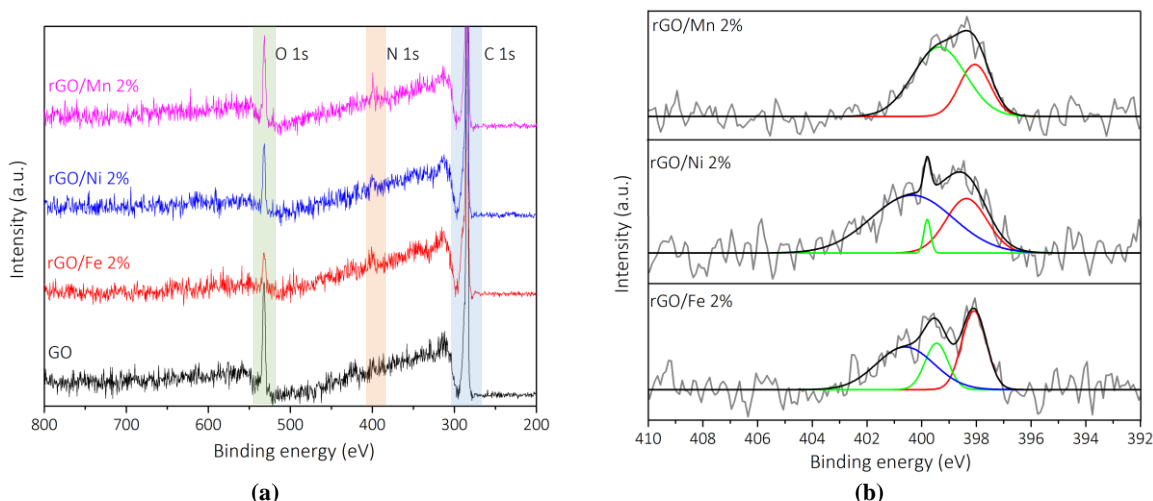


Figure 4.11. (a) XPS full and (b) high-resolution N 1s spectra of GO and rGO/M 2 %, M = Fe, Ni and Mn 2 %.

The reduction of GO can be illustrated through the decreasing of intensity of O 1s peaks in modified rGO catalysts in relation to GO. The low O1s peak intensity can be confirmed through the calculation of atomic concentration of oxygen (Table 4.1) that demonstrates the decreasing of O 1s concentration after the reduction of GO. Furthermore, at *ca.* 400 eV, it is observed a peak assigned to N 1s in rGO-based catalysts due to the N-doping of GO. Several investigation have shown that different nitrogen status, *i.e.* bonding feature between nitrogen atoms and carbon atoms, can result in a distinct catalytic activity of the material [17, 23, 59-61]. Figure 4.11(b) shows high-resolution N 1s spectra. The deconvoluted N1s peaks at *ca.* 398.3, 399.6, 400.4 and 402.2 eV that are assigned to pyridinic-N, M-N_x active site, pyrrolic-N and graphitic-N/pyridine-N-oxide, respectively. As mentioned in Chapter 2, it is considered that both pyridinic-N and graphitic groups are responsible for the enhancement of ORR activity, although this issue remains unclear. With this in mind, it will only be considered the total amount of nitrogen in the carbon material. From Table 4.1., the total amount of nitrogen increases from 0.62 *at %* to *ca.* 2 *at %* upon the N-doping of modified rGO materials. Compared with previous reports [6, 12, 18, 35-42, 105-107, 109, 111, 112, 114], the atomic concentration of nitrogen inside the rGO/M 2 % materials is quite low, which may be reflected in the ORR activity.

Table 4.1. Atomic concentration, *at %*, of C 1s, N 1s and O 1s in the samples GO, rGO/M 2 %, M = Fe, Ni and Mn 2 % determined by XPS. The values inside brackets are assigned to the calculated weight percentage, *wt %*.

Sample	<i>at %</i> of C1s	<i>at %</i> of N1s	<i>at %</i> of O1s
GO	88.93 (85.85)	0.62 (0.70)	10.46 (13.45)
rGO/Fe 2 % M1	95.42 (94.34)	2.27 (2.62)	2.31 (3.04)
rGO/Mn 2 % M1	90.78 (88.28)	1.40 (1.59)	7.82 (10.13)
rGO/Ni 2 % M1	92.13 (90.01)	1.53 (1.74)	6.34 (8.25)

On this experimental work, simultaneous N-doping and reduction of graphene oxide was achieved by both thermal and plasma reduction treatments. As mentioned in Chapter 2, the degree of reduction and porosity is temperature dependent and several investigations have shown highly doped materials [66, 67, 72]. On the other hand, the excited species in plasma treatment allow the conservation of the carbon framework upon the introduction of nitrogen atoms in the structure [85]. Thus, it is essential to study both of the used methods in the formation of a N-doped rGO material.

Firstly, thermogravimetric analysis (TGA) was performed to assess the graphitization degree and the chemical stability of the materials (Figure 4.12). The TGA curves were obtained under oxidizing

atmosphere from 30 to 800 °C and it is expected the formation of oxide metal species, M_xO_y . Thus, a higher oxidation resistance temperature is indicative of a better crystallinity of the material [35].

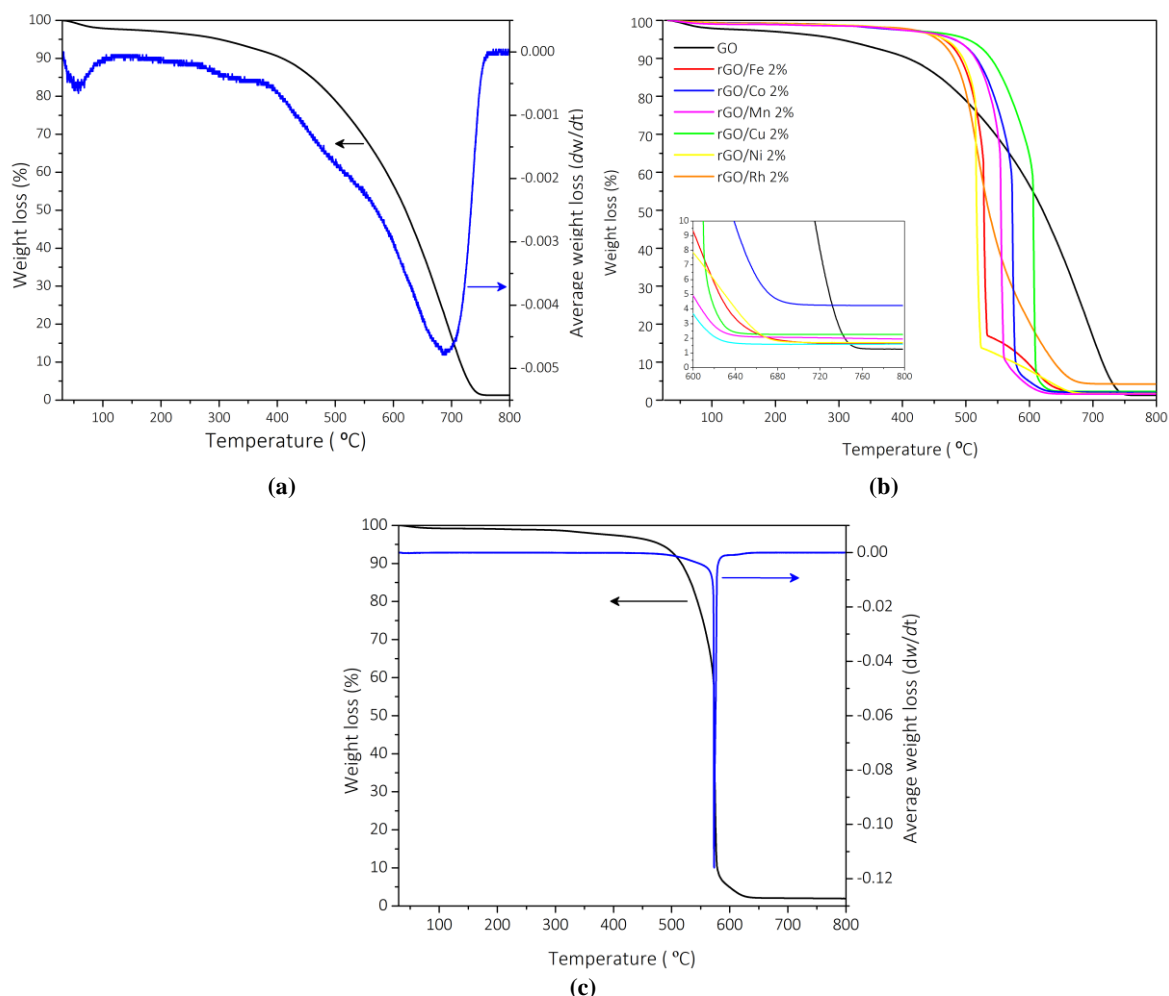


Figure 4.12. TGA and DTG curves of (a) graphene oxide, (b) TGA curves of graphene oxide and modified rGO 2 wt % materials and an expanded window between 600 and 800 °C (inset graph) and (c) rGO/Co 2 %.

The DTG curve is the difference thermogravimetric ratio of the measured weight loss over time, dw/dt . Usually, the steps of pyrolysis of the material are overlapped and a reliable quantitative and/or qualitative analysis from the TGA curve is hampered. Thus, the DTG profile provide information about the rate of mass loss and can also be used for the precise determination overlapping processes. Two apparent weight loss steps can be observed in the DTG curve: the release of adsorbed water in the structure with a total loss *ca.* 6.98 % (30 to 350 °C) followed by the decomposition of the carbon structure of 98.52 % above 750 °C, remaining only traces of non-organic material such as CO, H₂O and CO₂, as shown in Table 4.2.

Table 4.2. TGA minimum weight loss in % of graphene oxide and rGO/M 2 % electrocatalysts.

Sample	Minimum weight loss (%)
GO	1.259
rGO/Fe 2 % M1	1.628
rGO/Co 2 % M1	1.953
rGO/Mn 2 % M1	1.601
rGO/Cu 2 % M1	2.259
rGO/Ni 2 % M1	1.710
rGO/Rh 2 % M1	4.228

Consider the TGA curves of modified rGO 2 wt % materials shown in Figure 4.12(b). The similar TGA curves of rGO/M 2 % may imply an analogous doping method of the graphene oxide. Furthermore, the TGA profile curve of these materials is different from the one seen of GO, which can imply a different composition of the carbon framework. The degradation of rGO-based 2 wt % samples was carried out in three main steps: **(i)** the removal of light volatiles that account for 1.89 % of weight loss at 350 °C, followed by **(ii)** the pyrolysis of transition metals from 400 to 650 °C and finally **(iii)** the carbonization of the carbon structure at temperatures above 750 °C, which corresponds to 95.99 % of carbon material. Finally, the DTG profile of rGO/Co 2 % as an example of the decomposition of the prepared materials is depicted in Figure 4.12(c). According to the DTG profile, the pyrolysis of the material follows a one-step decomposition through a glassy state at 570 °C. Subsequently, the sample weight remains almost constant after 750 °C with a total degradation of average *ca.* 2.22 % of the initial sample weight up to 800 °C. The remaining traces of non-organic materials in all the modified rGO catalysts are suggestive of the formation of oxide metal species and other combustion resulting molecules.

As mentioned before, the crystallinity of the material can be related to the resistance of oxidation processes during the increasing of temperature. Assuming that the maximum temperature for highly stable material is up to 570 °C, the heat treatment of M1 (up to 700 °C) may have resulted in a decreasing of crystallinity of the structure. However, the analysis of Raman spectra of rGO/M 2 % materials showed a high ratio I_D/I_G that is characteristic of a crystalline structure material, comparable to results reported in previously [39, 103, 111, 113].

The estimation of the BET surface area is essential to understand the catalytic behaviour of the material. The specific surface area of the rGO/M 2 and 10 wt % was analysed by nitrogen adsorption-desorption isotherm. The surface area has been used as a criterion of high ORR performance of electrocatalysts [6, 18, 39-41, 106, 109, 112, 114]. A large surface area creates more active sites exposed and the hierarchical porous structure facilitates the mass transport of oxygen molecules to the active sites on the catalyst surface, enhancing the ORR activity. In order to study the effect of simultaneous doping/reducing process via thermal and plasma reduction, the porous structure volume and BET surface area of the synthesized nickel materials were analysed by nitrogen adsorption-desorption isotherm (Figure 4.13). In this work, the porous structure is composed by mesoporous, defined as a pore with a radius between 2 and 50 nm and micropores, whose pore radius is 2 nm or less.

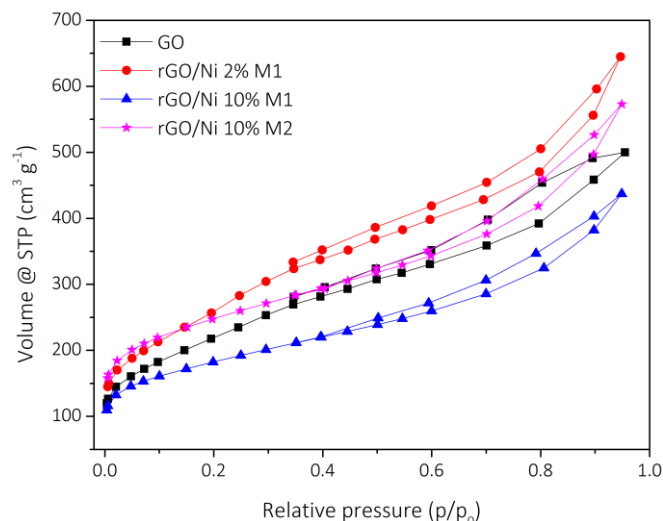


Figure 4.13. Nitrogen adsorption-desorption isotherm of the GO, rGO/Ni 2 % M1, rGO/Ni 10 % M1 and rGO/Ni 10 % M2.

Similar to the isotherm of GO depicted in Figure 4.5(b), isotherm curves show a mixture of type I and IV hysteresis (Figure 4.13), suggesting the presence of micro- and mesoporous structures in all the catalysts, which matches with the corresponding pore structures in Table 4.3. The rGO/Ni 2 % M1 catalyst exhibits the highest BET surface area of $923 \text{ m}^2 \text{ g}^{-1}$, followed by rGO/Ni 10 % M2 and rGO/Ni 10 % M1. The N activation process enhanced the surface area of rGO/Ni 2 % M1, due to the interaction of N with disordered carbon matrix, resulting in the creation of highly porous material capable of accommodate ORR active sites [6, 12]. This observation is in disagreement with previous reports that had shown the collapse of pore structure during the thermal reduction process, resulting in a decrease of surface area [41, 112]. The BET surface area of rGO/Ni 10 % M2 (*ca.* $886 \text{ m}^2 \text{ g}^{-1}$) is similar to those obtained for rGO/Ni 2 % M1 (*ca.* $923 \text{ m}^2 \text{ g}^{-1}$) that indicates the formation of an identical porous surface.

Table 4.3. BET surface area and pore structures of the electrocatalysts GO, rGO M2, rGO/Ni 2 %, rGO/Ni 10 % M1 and rGO/Ni 10 % M2.

Sample	$S_{\text{BET}} (\text{m}^2 \text{ g}^{-1})$	$A_{\text{micropore}} (\text{m}^2 \text{ g}^{-1})$	$V_{\text{total pore}} (\text{m}^3 \text{ g}^{-1})$	$V_{\text{micropore}} (\text{m}^3 \text{ g}^{-1})$	$V_{\text{mesopore}} (\text{m}^3 \text{ g}^{-1})$
GO	782	211	0.773	0.103	0.670
N-rGO M2	773	219	0.779	0.108	0.671
rGO/Ni 2 % M1	923	224	0.997	0.114	0.883
rGO/Ni 10 % M1	651	257	0.676	0.114	0.562
rGO/Ni 10 % M2	886	397	0.886	0.175	0.711

Elucidating the percentage of incorporated transition metal in the carbon structure is determining for the development of new doping techniques. Therefore, an elemental analysis was performed by Inductively Coupled Plasma – Optical Emission Spectrometry (ICP-OES) in several steps of the synthesis of modified rGO catalysts. Recalling Figure 3.2 from Chapter 3, the following stages are assigned to the different analysed samples: GO/M x %, N-rGO/M x % and rGO/M x %, $x=2$ and 10 wt % (Figure 4.14). It should be noted that the elemental analysis incorporated both of the reduction methods studied in this work (M1 – thermal reduction and M2 – plasma treatment) and the conclusions taken from rGO/Ni x wt % are extrapolated for all the synthesized compounds.

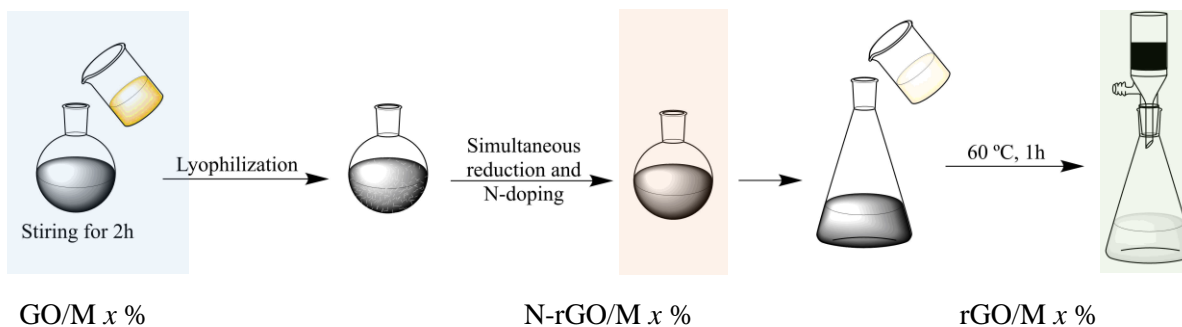


Figure 4.14. Brief schematics of the synthesis of rGO/M 2 and 10 % electrocatalysts catalysts, highlighting the different steps used in the ICP-OES analysis.

The elemental composition of nickel as an example of the analysis is shown in Table 4.4. According to the composition of each of the stages, the incorporation of transition metal is the first step for the doping process of GO, in which a solution containing a metal salt is added to an aqueous solution of graphene oxide and then stirred. This process is enabled the incorporation of *ca.* 83 % and 43 to 44 % of 2 and 10 *wt* % metal inside of the carbon structure, respectively. The remaining metal that was not integrated on the graphene can be located between carbon layers.

Table 4.4. Elemental composition in *wt* % of nickel in reduced graphene oxide doped catalysts synthesized by M1 and M2, according to the different steps highlighted in Figure 4.14.

Stage synthesis Sample doped with:	GO/Ni x <i>wt</i> % $x = 2$ or 10	N-rGO/Ni x <i>wt</i> % $x = 2$ or 10	rGO/Ni x <i>wt</i> % $x = 2$ or 10
2 <i>wt</i> % M1	1.65	1.90	0.41
10 <i>wt</i> % M1	4.31	7.11	0.32
10 <i>wt</i> % M2	4.42	3.36	0.046

Upon the N-doping and reduction of GO/M x % by M1 and M2, it is expected that some of the non-incorporated metal bonds with nitrogen, forming an ORR active site M-N_{*x*} and increasing the amount of embedded metal atoms. The quantity of metal incorporated is *ca.* 95 % and 71 % for M1. However, during plasma treatment M2, the elemental composition decreases 11 %, which can imply low N-doping.

The goal of the washing with an acidic solution is to remove excess of non-incorporated metal in the graphene structure, which is achieved, according to the elemental composition of the final compound, rGO/Ni x %. Compared to previous results reported in the literature [6, 18, 35-39, 41, 42, 105-107, 109, 111, 112, 114], the rGO/M x %, $x = 2$ and 10 % exhibited comparable atomic concentration of transition metal, with the incorporation of 20.5 % and 3.2 to 0.46 % of 2 and 10 *wt* % of metal in the structure, respectively.

4.2.2. THE EFFECT OF AROMATIC METALLOPORPHYRIN IN rGO

The ORR electrocatalytic activity of metallophthalocyanines and porphyrins has been the hotspot of several reports [35-54]. The interaction of aromatic M-N₄ molecules with the conjugated π -system of graphene structure is essential to ensure the functionalization and prevention of aggregation of GO sheets that would adversely affect the ORR activity. In our research, the incorporation and ORR activity of tetramethoxyphenyl porphyrins are investigated, particularly iron, cobalt and manganese M-N₄ macrocycles (Figure 2.15(a) and 4.15).

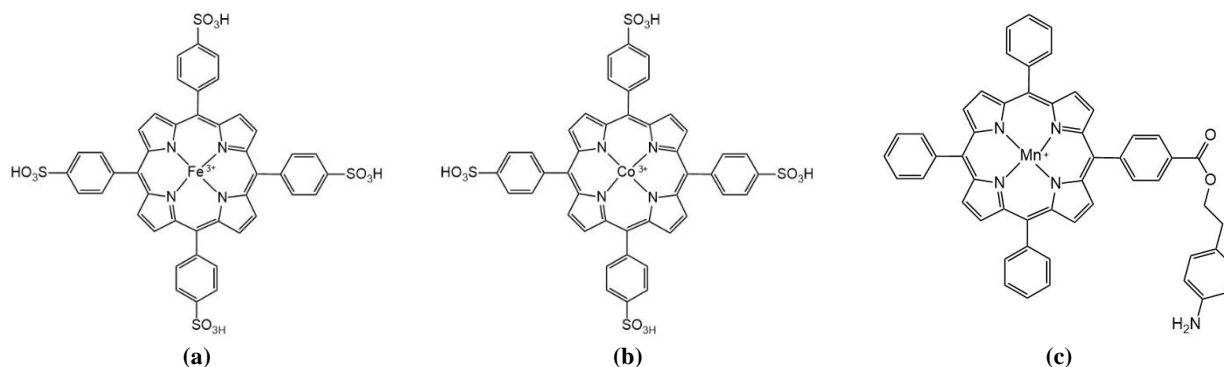


Figure 4.15. Schematic of (a) iron and (b) cobalt tetramethoxyphenyl porphyrins and (c) manganese metalloporphyrin.

The synthesis of rGO/P 2 %, P = FeP, CoP, VB₁₂ and MnP is based on the procedure reported on [125] that takes advantage of the π interaction between the aromatic structure of the macrocycle and the electronic π -system of graphene (Figure 4.16(a)). The nature of the active center of the catalysts is directly affected during the pyrolysis treatment because of the possibility of dispersing the macrocycle on the carbon structure by a chemisorption process, remaining intact the metal center [162]. Concerning the carbon framework, it is expected the preservation of the graphene structure. Although the optimal pyrolysis temperature is between 400 to 800 °C, the heat treatment at *ca.* 750 °C under nitrogen atmosphere is high enough to induce the reduction of graphene oxide and the collapse of graphene layers. Moreover, the graphene sheets can also aggregate in small clusters, as shown in the AFM image in Figure 4.16(b). After pyrolysis, the material was not subject to an acid wash and remaining metalloporphyrins are observed in the AFM image.

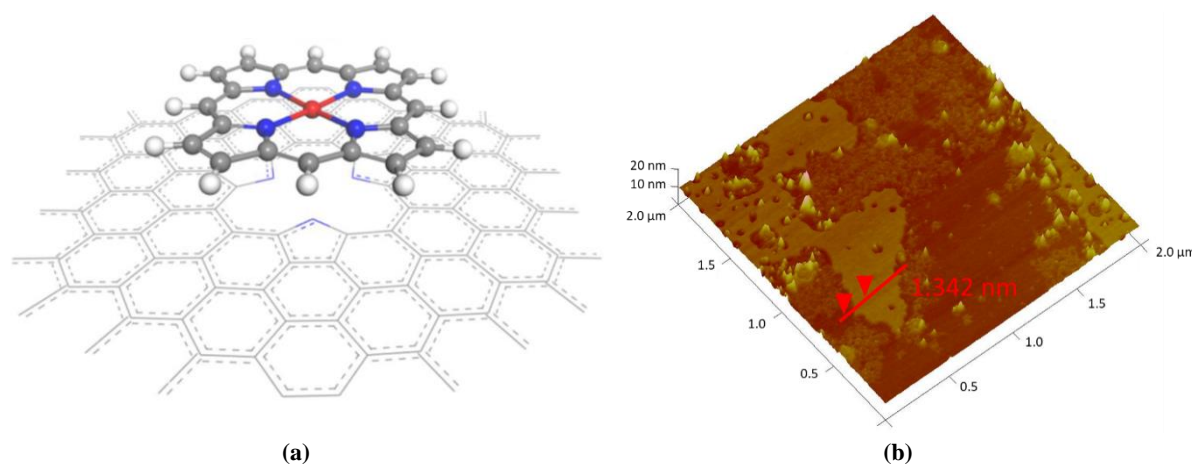


Figure 4.16. (a) Schematic illustration of π interaction between the aromatic structure of the macrocycle and the electronic π -system of graphene [163] and (b) morphologic AFM 3D image of rGO/CoP.

Despite the presence of nitrogen in the structure of porphyrins, the pyrolysis of iron and cobalt porphyrins under a nitrogen atmosphere can catalyze the formation of N-doped carbon material. The confirmation of the N-doping of reduced graphene oxide was achieved using FT-IR spectroscopy and the FT-IR spectra of rGO/P 2 % are shown in Figure 4.17(a). As an oxidized carbon support material, the presence of oxygen-containing functional groups is imperative at *ca.* 3425 cm⁻¹, 2975 cm⁻¹, 1384 cm⁻¹ and 1043 cm⁻¹, assigned to O-H stretching vibrations from hydroxyl groups and water molecules, asymmetric CH₂ stretching of carbon structure, C-OH and C-O alkoxy stretching, respectively. Moreover, the bands at *ca.* 1579 cm⁻¹, 1096 cm⁻¹ and 877 cm⁻¹ are characteristic of a reduced graphene oxide material, corresponding to the non-aromatic C=C, C-O-C stretching and epoxy groups, respectively. Concerning the N-doping and the immobilization of metalloporphyrins in the carbon framework, the low intensity of amino functional groups in the structure is not significant.

enough to consider more than one peaks at 1634 cm^{-1} , assigned to the stretching of C=N bond and possible overlapping of O-H and N-H stretches at 3425 cm^{-1} . Similarly to rGO doped with transition metal, the presence of the metal in the center of porphyrin is not detected.

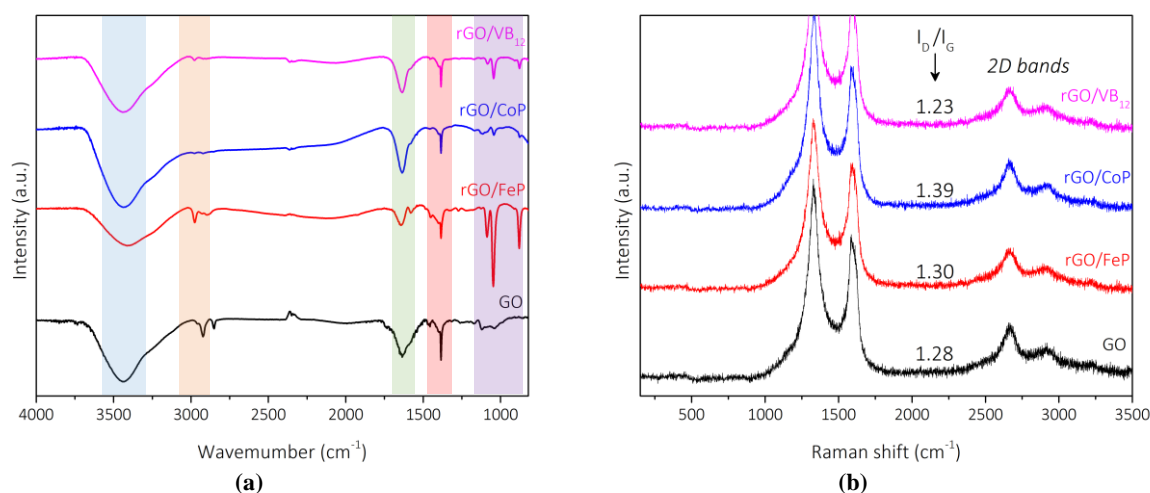


Figure 4.17. (a) FT-IR and (b) Raman spectra of graphene oxide and doped rGO with macrocycle molecules.

Analogous to the analysis of the crystallinity of rGO-transition metals, Raman spectroscopy was used to determine the degree of graphitization of porphyrin-based reduced graphene oxide. Figure 4.17(b) shows Raman spectra of the obtained materials and the corresponding ratio of I_D/I_G . Although the pyrolysis at high temperature, the I_D/I_G values of GO and rGO/P 2 % catalysts are similar, which implies similar graphitization degree of the carbon structure.

During the pyrolysis under nitrogen atmosphere, the rGO/P 2 % materials were subjected to a heat treatment at $750\text{ }^\circ\text{C}$ for 2 hours. Comparing this procedure with the simultaneous N-doping and reduction of GO using M1, the exposition period is relatively small which can induce lower nitrogen doping in the structure and, thus, lower I_D/I_G values for porphyrin-based materials, as it is observed. In fact, the ratio I_D/I_G of all the porphyrins is similar to those determined to rGO/M 10 %, which implies the same crystallinity of the support material. Moreover, a few couple of bands centered at 2700 cm^{-1} are also observed in rGO/P 2 % samples, corresponding to few-layered graphene-based materials.

4.3. ELECTROCHARACTERIZATION OF MODIFIED rGO MATERIALS TOWARDS ORR

The physical, chemical and elemental analysis described in the previous subchapter was the first step to understand the electrocatalytic activity of the synthesized material as ORR catalyst. Concerning the study of the mechanism of ORR, the activity of the modified rGO materials as electrocatalysts towards ORR in aqueous acidic, alkaline and neutral solutions is discussed, using the rotating disk electrode (RDE) and the rotating ring-disk electrode (RRDE) as tools to achieve the goal of this work.

The primary motivation for the development of electrocatalysts for ORR is to determine the number of electrons n in the reaction that can be associated to the ORR mechanism. Recalling the mechanism of oxygen reduction mentioned in Chapter 2, the ORR in aqueous solution occurs mainly by three theoretical processes: (i) direct 4-electron transfer through the formation of water molecule, (ii) 2+2 electron pathway that is characterized by the formation of peroxide species that are reduced to water and (iii) 2 electron pathway that forms only peroxide species, as shown in the Figure 4.18.

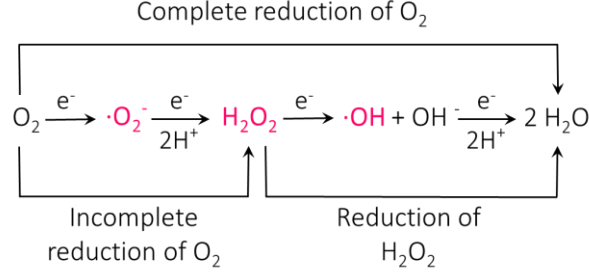


Figure 4.18. Schematic of the possible mechanism of oxygen reduction by the transfer of 2, 4 or 2+2 electrons.

The apparent number of electrons transferred during ORR, n , was determined by the Koutecký-Levich (K-L) equation at different potentials (Equation 4.1). The selected potential range comprehends the mixed kinetic-diffusion controlled area to calculate the electron transfer number.

$$\frac{1}{i} = \frac{1}{i_K} + \frac{1}{i_L} = \frac{1}{i_K} + \frac{1}{B \omega^{1/2}} \quad (4.1)$$

$$B = 0.62nFD_i^{2/3}\nu^{-1/6}c^0 \text{ at } 25 \text{ }^\circ\text{C}$$

The experimental parameters diffusion coefficient D_i , molar oxygen concentration c^0 , and kinematic viscosity ν , are dependent on the aqueous solution used in the measurement. Table 4.5 shows the experimental parameters used in the K-L equation depending on the aqueous solution used in the ORR measurement.

Table 4.5. Experimental parameters used in the Koutecký-Levich equation for the determination of the number of electrons, according to the electrolyte used in the measurement.

Electrolyte solution	0.1 M H ₂ SO ₄ [164]	0.1 M KOH [165]	PBS pH 7.4 [166]
Experimental Parameter			
c^0	2.9×10^{-4} M at 22 °C	2.4×10^{-7} M	2.4×10^{-7} M
D_i	1.7×10^{-5} cm ² s ⁻¹ at 22 °C	1.73×10^{-5} cm ² s ⁻¹	1.73×10^{-5} cm ² s ⁻¹
ν	0.01 cm ² s ⁻¹ at 22 °C	0.01 cm ² s ⁻¹	0.01 cm ² s ⁻¹

Theoretically, most of iron and manganese complexes catalyse the ORR through a 4-electron transfer pathway, while cobalt and nickel materials reduce oxygen to peroxide species by 2-electron pathway [33, 167]. Unfortunately, the ORR performance of these new catalysts shows a more complex interpretation of the number of electrons determined by K-L equation. Usually, the ORR catalytic performance of a transition metal doped N-rGO might be the result of joint effects: **(i)** the overall N content/active N content, **(ii)** metal residue and **(iii)** the surface area of the carbon structure. Assuming that the average number of electrons n is composed by two contributions: a % from 4-electron pathway + b % from 2-electron route, hereafter, the determination of each contribution is achieved by the following equation:

$$\begin{cases}
 2a_{4\text{-electron}} + 4b_{4\text{-electron}} = n \\
 a_{4\text{-electron}} + b_{2\text{-electron}} = 1
 \end{cases} \quad (4.2)$$

This methodology considers the number of electrons transferred by N and C active sites that were previously reported in the literature, *i.e.*, 4- and 2-electron pathway respectively [33, 87-90].

4.3.1. THE EFFECT OF pH OF THE ELECTROLYTE: A BRIEF ANALYSIS

The study of the ORR mechanism is complicated not only for the diversity of possible electron transference reaction but also for the impact from the pH of the electrolyte solution [168]. The development of new materials capable of act as electrocatalysts in an effective and durable way in acidic medium is one of the challenges of this work. It was been reported the low activity towards ORR in acid electrolyte due to the protonation of nitrogen sites and degradation of the carbon material [37-39].

Extensive investigation on the ORR catalytic activity of a material under alkaline conditions has been reported, not only due to the less corrosive environment compared to acidic media, but also because of the reduction of adsorption energies of the reactants on the electrode surface and faster kinetics [168]. Thus, the activity of the electrocatalysts towards ORR can be easier verified in alkaline medium rather than in acidic solution. Lastly, the study of ORR in neutral solutions is of great interest on the development of power supplies for implantable medical devices, despite fewer reported investigation of the issue [120]. The ORR activity in neutral electrolytes is expected to be in the middle of the performance observed in alkaline and acidic media.

Figures 4.19, 4.20 and 4.21 show the ORR polarization curves of rGO/M 2 and 10 % and rGO/P 2 % in the three electrolyte solutions, respectively. Table 4.6 presents the onset, E_{onset} , and half-wave, E_{half} , potentials for all the synthesized electrocatalysts, in acidic, alkaline e neutral aqueous solutions.

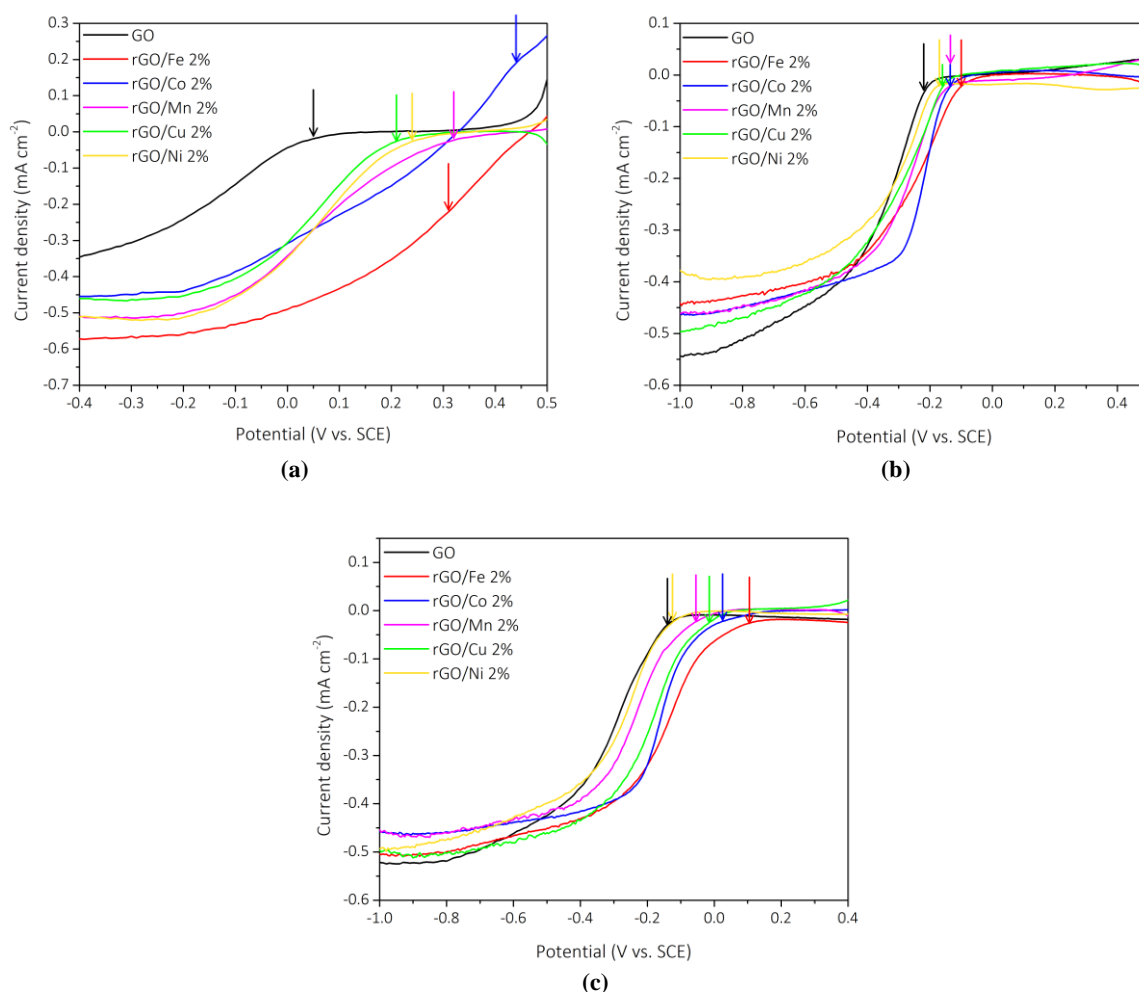


Figure 4.19. Comparison of the ORR polarization curves of **rGO/M 2 %** in air-saturated (a) 0.1 M H₂SO₄, (b), 0.1 M KOH and (c) 0.01 M PBS electrolytes recorded at 800 rpm on GC modified electrode at 10 mV s⁻¹.

In a first analysis of the LSVs obtained for all the synthesized catalysts, as expected, the ORR onset potential is adjusted with the pH of the electrolyte solution. For example, the electrocatalysts rGO/Fe 2 % exhibits an onset potential of 0.42 V vs. SCE in acidic medium that shifts by *c.a.* 600 and 500 mV to -0.22 V and -0.14 V vs. SCE in alkaline and neutral media, respectively. The potential shift can be explained by the high overpotential required for O₂/O₂^{•-} redox couple in acidic medium that is correlated to the high free energy of adsorption of O₂ of the catalysts [26]. This feature of the electrocatalysts is essential to distinguish the most suitable catalysts for ORR as the contribution for the catalytic activity is assigned to intrinsic activity of the material. Thus, the ORR performance increases in acidic medium with the catalytic activity increases in the following order: GO < rGO/Cu 2 % < rGO/Ni 2 % < rGO/Mn 2 % ~ rGO/Fe 2 % < rGO/Co 2 %.

Table 4.6. Electrocatalytic activity of the GC rotating disk electrode modified rGO materials in aqueous 0.1 M H₂SO₄, 0.1 M KOH and 0.01 M PBS solutions. The potentials values correspond to the onset and half-wave potential values vs. SCE. The values inside brackets are assigned to the E_{onset} and E_{half} potential values vs. reversible hydrogen electrode (RHE).

Sample	Acidic electrolyte		Alkaline electrolyte		Neutral electrolyte	
	E _{onset} /V ^a	E _{half} /V ^b	E _{onset} /V ^a	E _{half} /V ^b	E _{onset} /V ^a	E _{half} /V ^b
GO	0.05 (0.37)	-0.12 (0.56)	-0.22 (0.79)	-0.35 (0.33)	-0.14 (0.54)	-0.32 (0.36)
rGO/Fe 2 %	0.31 (0.63)	-0.34 (0.34)	-0.10 (0.91)	-0.26 (0.42)	0.11 (0.78)	-0.16 (0.52)
rGO/Co 2 %	0.44 (0.76)	0.18 (0.86)	-0.14 (0.87)	-0.23 (0.45)	0.03 (0.70)	-0.16 (0.52)
rGO/Mn 2 %	0.32 (0.64)	0.06 (0.74)	-0.14 (0.87)	-0.28 (0.40)	-0.06 (0.62)	-0.25 (0.43)
rGO/Cu 2 %	0.21 (0.53)	0.05 (0.73)	-0.16 (0.85)	-0.32 (0.36)	-0.02 (0.66)	-0.19 (0.49)
rGO/Ni 2 %	0.24 (0.56)	0.06 (0.74)	-0.17 (0.84)	-0.31 (0.37)	-0.13 (0.55)	-0.29 (0.39)
rGO/Fe 10 %	0.16 (0.48)	-0.13 (0.55)	-0.24 (0.77)	-0.23 (0.45)	-0.04 (0.64)	-0.28 (0.40)
rGO/Co 10 %	0.06 (0.38)	-0.09 (0.59)	-0.20 (0.81)	-0.31 (0.37)	-0.04 (0.64)	-0.30 (0.38)
rGO/Mn 10 %	0.07 (0.39)	-0.14 (0.54)	-0.23 (0.78)	-0.34 (0.34)	-0.12 (0.56)	-0.30 (0.38)
rGO/Cu 10 %	0.06 (0.38)	-0.11 (0.57)	-0.17 (0.84)	-0.33 (0.35)	-0.12 (0.56)	-0.31 (0.37)
rGO/Ni 10 %	0.12 (0.44)	-0.04 (0.64)	-0.19 (0.82)	-0.38 (0.30)	-0.14 (0.55)	-0.31 (0.37)
rGO/FeP 2 %	0.12 (0.44)	-0.10 (0.58)	-0.21 (0.80)	-0.34 (0.34)	0.06 (0.74)	-0.25 (0.43)
rGO/CoP 2 %	0.35 (0.67)	-0.13 (0.80)	-0.18 (0.83)	-0.27 (0.41)	0.025 (0.70)	-0.17 (0.51)
rGO/VB ₁₂ 2 %	0.40 (0.71)	0.20 (0.88)	-0.16 (0.85)	-0.32 (0.36)	-0.04 (0.64)	-0.20 (0.48)
rGO/MnP 2 %	0.10 (0.41)	-0.08 (0.60)	-0.17 (0.84)	-0.23 (0.45)	-0.11 (0.57)	-0.29 (0.39)
Pt/C 20 wt % [109] ^c	0.81 ^d	0.65 ^d	0.95 ^e	0.83 ^e	—	—

^a At -0.40 V vs SCE and 800 rpm, calculated considering the potential at which the current density reaches 5 % of the limiting current density.

^b Calculated by the average between the potential at 0.4 V and -0.40 V (in acidic media) and 0.4 V and -1.0 V (in alkaline and neutral media).

^c Pt/C 20 wt % catalysts with 0.1 mg cm⁻² loading in a glassy carbon electrode.

^d Onset and half-wave potentials vs. RHE in 0.1 M HClO₄ pH = 1.

^e Onset and half-wave potentials vs. RHE in 0.1 M KOH pH = 13.

This brief analysis of the polarization curves of the rGO/M 2 % catalysts and their ORR catalytic activity can be supported by physical and chemical characterization discussed in the previous subchapter. For example, the ratio of I_D/I_G calculated in Raman spectra translate the crystallinity of the material and previous reports have already shown that the increased ORR activity may be a result of a higher ratio of I_D/I_G [161]. As expected, rGO/Fe 2 % and rGO/Co 2 % exhibit a higher ORR activity compared to the remaining catalysts, in 0.1 M H₂SO₄ solution. Surprisingly, the reaction does not follow a 2 or 4-electron pathway, but a mixed 2+4 electron transfer due to several contributions on the material. This conclusion will be discussed in the subchapter 4.2.3. The enhancement of the specific surface area

induced by the highly porous structure on rGO/M 2 % also contributes for the increasing of the ORR activity. A larger surface area provides a more porous structure that facilitates de mass transport of oxygen molecules to the active site. Another surface analysis technique, such as XPS, is essential for the study of the composition of the material' surface, specially the content of nitrogen. The synergistic effect between pyridinic-N and graphitic-N with both transition metal and carbon structure is considered to be the most pronounced effect that results in the enhancement of the ORR activity. Although the atomic concentration of N 1s in the structure is quite low (*c.a.* 1.7 at %), the contribution of N-type groups for the ORR is clearly observed in the polarization curves.

Table 4.7. Number of electrons calculated by K-L plots for rGO/M 2 % materials in acidic, alkaline and neutral electrolyte solutions.

Material	Number of electrons		
	Acid	Alkaline	Neutral
rGO/Fe 2 %	2.95	3.03	3.04
rGO/Co 2 %	2.14	3.12	3.60
rGO/Mn 2 %	3.06	3.04	2.40
rGO/Cu 2 %	2.67	3.16	2.36
rGO/Ni 2 %	2.60	1.82	2.94

One of the main drawbacks of the ORR performance of an electrocatalysts in acidic solution is the protonation of nitrogen sites that contribute for the catalytic activity and are blocked by bonding with protons. Comparing the number of electrons in acidic and alkaline media shown in Table 4.7, it is observed an increase of the number of electrons from acidic to alkaline media that may correspond to the deprotonation of nitrogen sites, increasing the active sites of the material. Thus, in aqueous acidic solutions, the predominant contribution for the ORR activity comes from the active sites from the metal.

An analogous study can be done for both rGO/M 10 % catalysts. Similarly to rGO/M 2 %, the ORR onset potentials are dependent on the pH of the electrolyte solution, exhibiting a negative potential shift of *c.a.* 400 mV from alkaline to acidic medium (Figure 4.20). Once more, the negative shift of onset potential can be explained by the high overpotential for the first step of ORR that is correlated to the characteristic free energy of adsorption of the electrocatalysts. Therefore, the ORR activity increases in acidic solution in the following order for rGO/M 10 %: GO < rGO/Cu 10 % ~ rGO/Co 10 % < rGO/Mn 10 % < rGO/Ni 10 % < rGO/Fe 10 %.

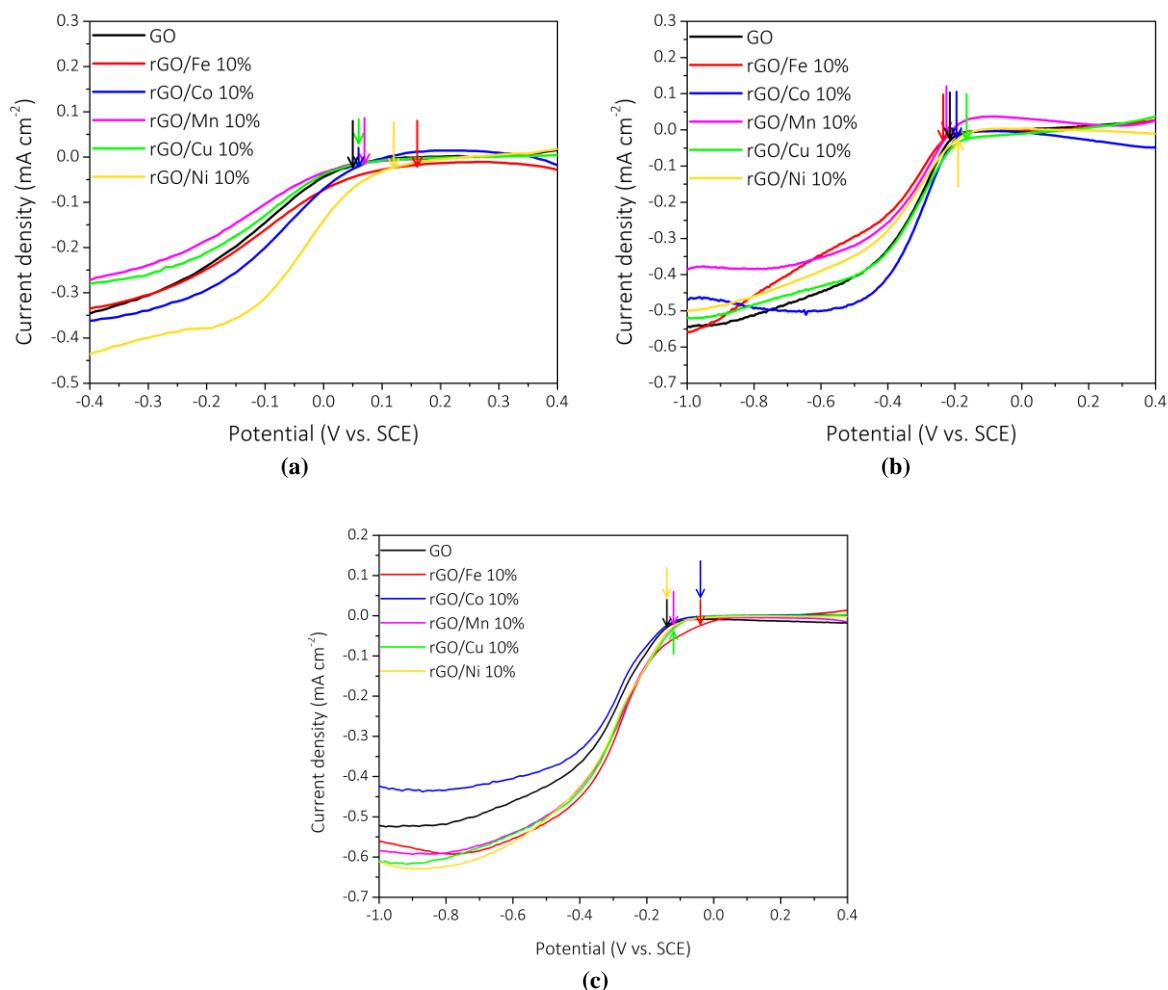


Figure 4.20. Comparison of the ORR polarization curves of **rGO/M 10 %** in air-saturated (a) 0.1 M H₂SO₄, (b) 0.1 M KOH and (c) 0.01 M PBS electrolytes recorded at 800 rpm on GC modified electrode at 10 mV s⁻¹.

Furthermore, it is also possible to check that the number of electrons calculated from acidic medium are lower than the ones from alkaline and neutral media, indicating possible protonation of nitrogen atoms in an acidic electrolyte that decreases N-active sites (Table 4.8).

Table 4.8. Number of electrons calculated by K-L plots for rGO/M 10 % materials in acidic, alkaline and neutral electrolyte solutions.

Material	Number of electrons		
	Acid	Alkaline	Neutral
rGO/Fe 10 %	2.52	3.10	2.77
rGO/Co 10 %	1.68	4.09	2.05
rGO/Mn 10 %	1.71	3.40	3.48
rGO/Cu 10 %	0.88	3.84	3.53
rGO/Ni 10 %	3.57	2.91	3.57

Figure 4.21 shows the polarization curves of rGO/P 2 % in acidic, alkaline and neutral solutions. According to Table 4.7, the negative potential shift of *c.a.* 400 mV is observed as a consequence of the decreasing of the overpotential required for O₂/O₂⁻ redox couple in acidic medium. The onset potential for rGO/P 2 % are similar to rGO/ M 2 %, although it would be expected lower ORR activity in acidic medium owing to low ratio I_D/I_G , as proved previously [161]. Therefore, the ORR activity of

metalloporphyrins is assigned to the intrinsic activity of these materials. In acidic medium, the ORR activity increases in the following order for rGO/P 2 %: GO < rGO/MnP < rGO/FeP < rGO/CoP < rGO/VB₁₂.

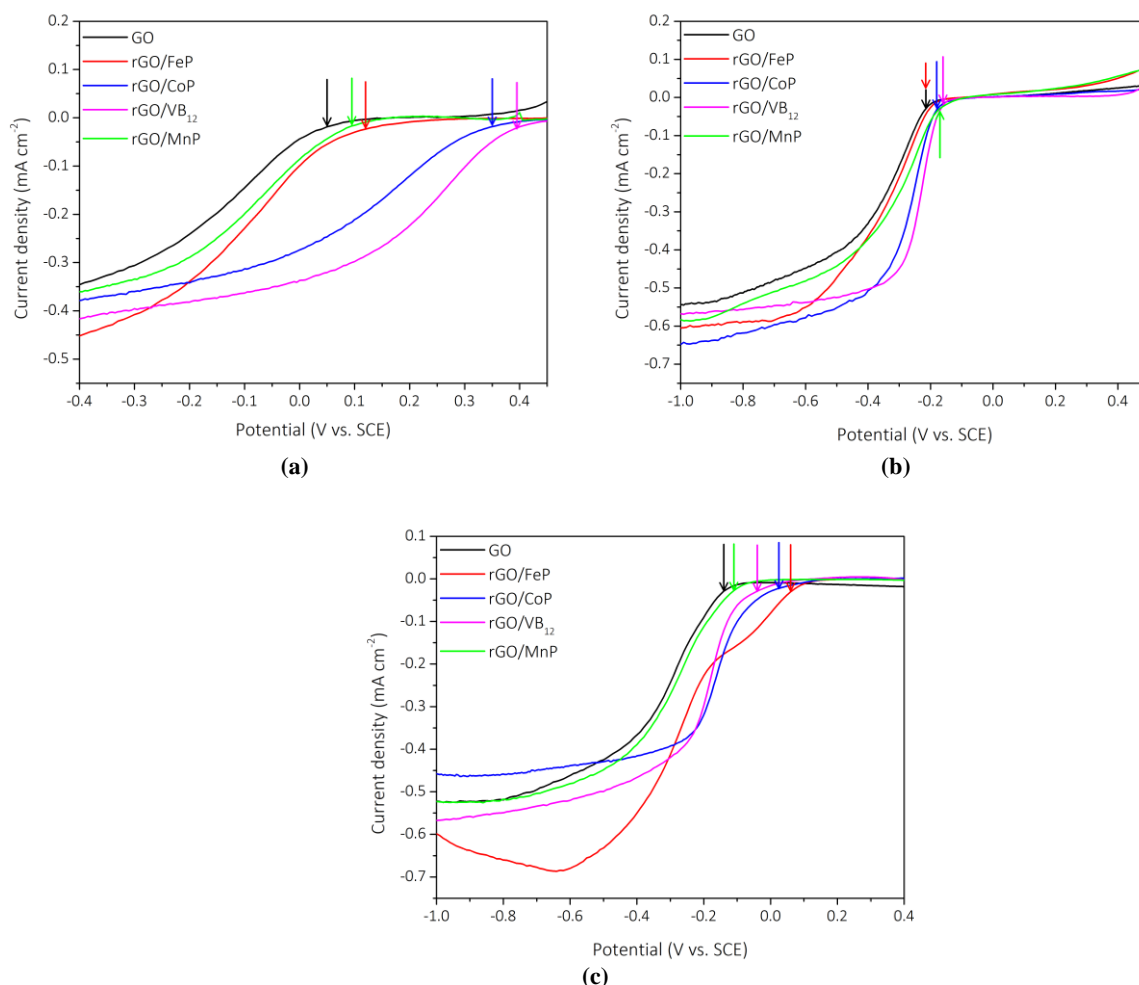


Figure 4.21. Comparison of the ORR polarization curves of rGO/P 2 % in air-saturated (a) 0.1 M H₂SO₄, (b) 0.1 M KOH and (c) 0.01 M PBS electrolytes recorded at 800 rpm on GC modified electrode at 10 mV s⁻¹.

The number of electrons calculated by K-L equation for all the electrolyte solutions are shown in Table 4.9. Analogous to other catalysts, the calculated number of electrons from acidic medium are lower than the ones from alkaline and neutral media, which is indicative for the protonation of N-active sites in the carbon structure.

Table 4.9. Number of electrons calculated by K-L plots for rGO/P 2 % materials in acidic, alkaline and neutral electrolyte solutions.

Material	Number of electrons in:		
	Acid	Alkaline	Neutral
rGO/FeP	3.85	4.07	4.07
rGO/CoP	2.13	3.88	3.60
rGO/VB ₁₂	3.34	3.74	3.24
rGO/MnP	1.69	3.63	2.96

Among all the synthesized materials, the most promising ORR performance is assigned to rGO/M and P 2 % catalysts, in which **iron** and **cobalt**-based electrodes exhibit the most encouraging results for

a deeper study towards ORR. Recalling that platinum-based electrodes are known for being the most efficient catalysts for ORR [24, 25], the comparison between a commercial Pt/C electrode and the produced catalysts is critical to draw conclusion about the ORR activity. Figure 4.22 shows the onset and half-wave potentials of Pt/C (20 wt % Pt on carbon black) [109] and the rGO/M and P 2 % electrocatalysts in acidic and alkaline medium.

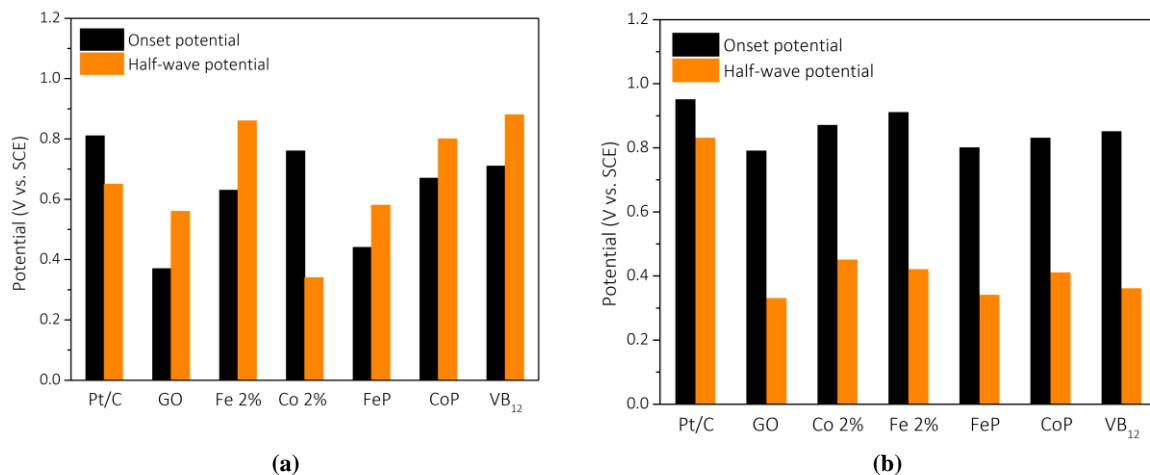


Figure 4.22. Comparison of the ORR onset and half-wave potentials between Pt/C and rGO/M and P 2 % electrocatalysts in (a) 0.1 M H₂SO₄ and (b) 0.1 M KOH solutions.

Despite its lower ORR activity in acidic medium, Pt/C electrode exhibits higher onset potential compared to rGO/M and P 2 % electrodes. On the other hand, in alkaline solution, a remarkable increase of all the onset potential values from the synthesized materials is observed that is comparable to commercial Pt/C, as shown in Figure 4.22(b).

4.3.2. ROLE OF GRAPHENE OXIDE

Before the incorporation and immobilization of transition metals and aromatic macrocycle in the graphene oxide structure, the ORR performance of the graphene oxide as a supporting material was investigated. Figure 4.23 shows the polarization curves of GO in an acidic electrolyte. Under an air-saturated 0.1 M H₂SO₄ solution, the current densities are increased as the rotation speed goes from 400 to 2400 rpm, that implies mass transport of O₂ to the electrode surface and the subsequent reduction reaction. The onset potential was determined to be 0.06 V, -0.22 V and -0.14 V vs. SCE in acidic, alkaline and neutral media, which is in agreement with the values in the literature [169].

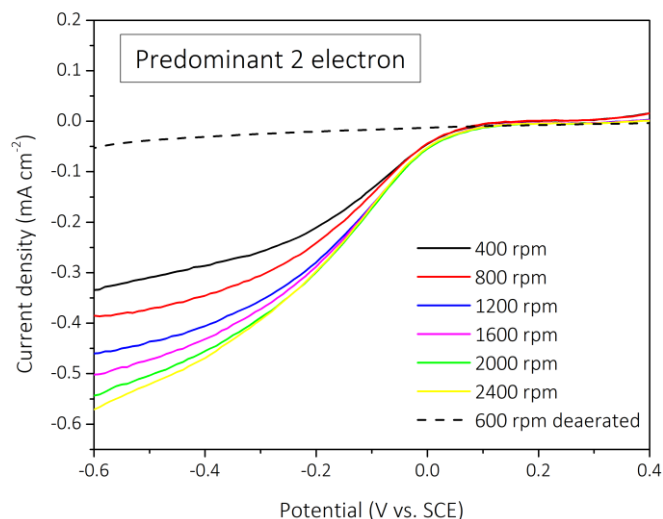


Figure 4.23. Polarization curves of graphene oxide in a GC rotating disk electrode recorded at different rotation rates for ORR N_2 and air-saturated $0.1\text{ M H}_2\text{SO}_4$ at 10 mV s^{-1} .

The ORR catalytic activity of graphene oxide is low studied in the literature. However, it is expected that the performance of GO is similar to other carbon structures, such as glassy carbon and carbon black that show a 2-electron pathway [33]. One of the main features of these carbon materials is their high oxygen content, creating a highly hydrophilic material (Figure 4.24(a)). It has been reported that hydrophilicity can assist on the transport of oxygen species to the material active sites via hydrogen bonds [170], which increases the catalytic performance of the carbon material. The corresponding Koutecký-Levich (K-L) plots at different potentials are depicted in Figure 4.24(b), from which it was calculated the number of electrons, n , at different potentials.

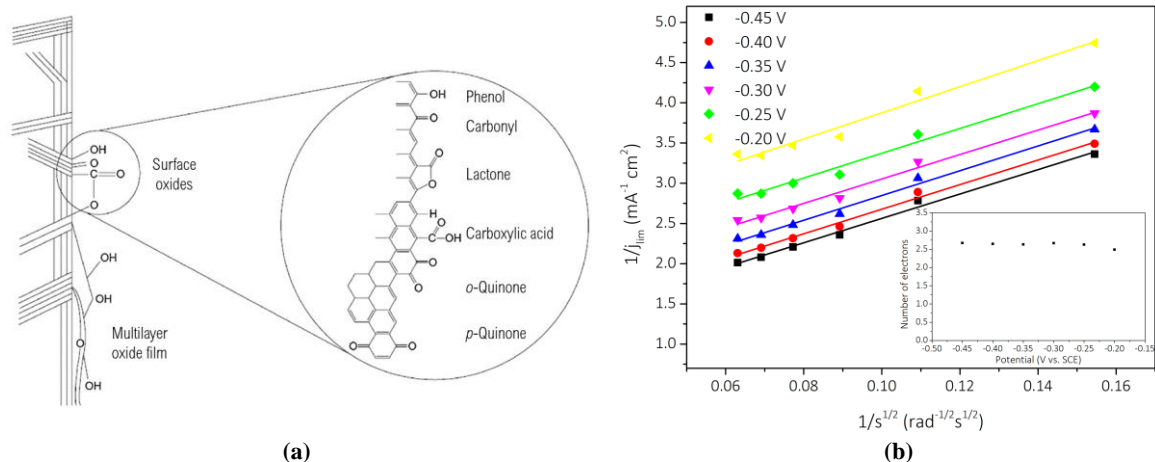


Figure 4.24. (a) Carbon surface features of relevance to the electrochemistry and details of some different oxygen-containing surface functional groups. Adapted from [28]. (b) Koutecký-Levich plots at different potentials. Inset graph: the variation of number of electrons with the potential.

From the slopes of the K-L plots from -0.20 to -0.45 V vs. SCE , the number of electrons transferred in this reaction was estimated to be 2.62, which indicates a predominant 2-electron reduction of oxygen. Moreover, the linear and parallel K-L plots are indicative of a first order reaction controlled by kinetics and mass transport of oxygen species to the electrode surface. An analogous polarization plots are observed for GO in alkaline and neutral solutions as shown in Figure 4.25(a) and (b), respectively. The average n was determined to be 2.77 and 2.75 in 0.1 M KOH and 0.01 M PBS , respectively.

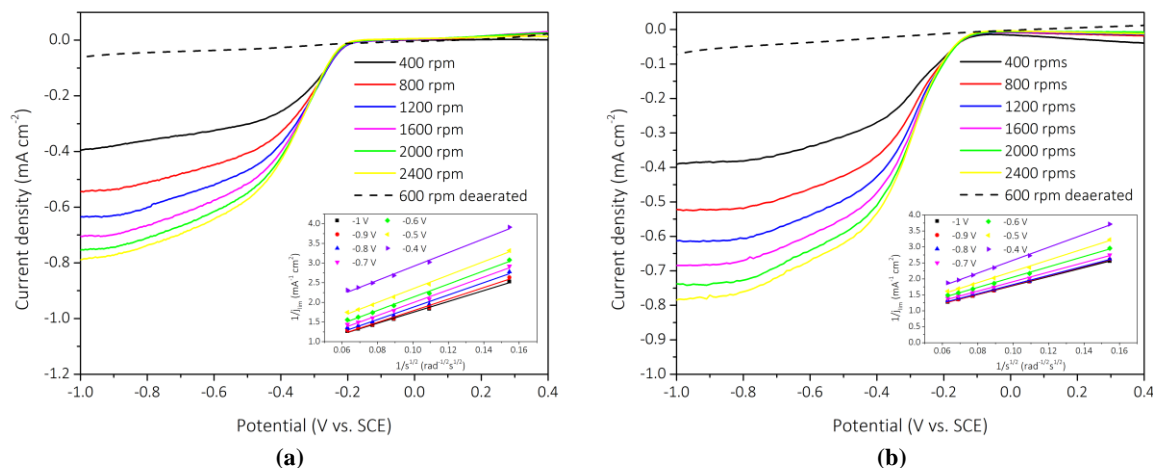


Figure 4.25. Polarization curves of graphene oxide in a GC rotating disk electrode recorded at different rotation rates for ORR N_2 and air-saturated (a) 0.1 M KOH and (b) 0.01 M PBS, at 10 mV s^{-1} . Inset: Koutecký-Levich plots at different potentials.

Considering that the GO reveals only a 2-electron pathway, the 4-electron route contribution can be assigned to the nitrogen groups inside of the carbon structure. Although low concentration (*c.a.* 0.69 wt %), the presence of nitrogen atoms on the GO enhances the ORR performance of the material, which is essential to understand the high activity of N-doped materials, in either acidic, alkaline or neutral media. It is assumed that, in acidic solutions, the protonation of nitrogen atoms decreases the ORR performance of the material, and the contribution of deprotonated nitrogen atoms is 31 % by Equation (4.2). However, the protonation of nitrogen atoms does not occur in all the nitrogen sites of the carbon structure, as shown in Figure 4.26, and, therefore, the contribution for the 4-electron pathway is may be assigned to graphitic-N active sites.

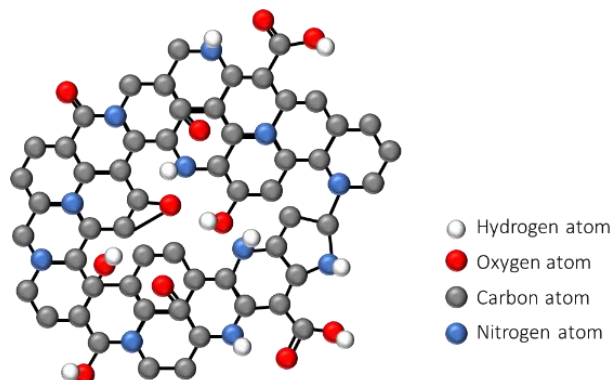


Figure 4.26. Protonation of nitrogen atoms upon the reduction of oxygen in aqueous acidic solution.

Increasing the value of pH of the electrolyte, the protonation is not significant, and it is expected that the ORR activity of the graphene oxide improves as more N-active sites are available for the reduction of oxygen. The number of electrons in alkaline and neutral media increased, and the calculated contributions of 2- and 4-electron pathway for ORR are shown in Table 4.10. As expected, the contribution of 4-electron pathway increased with the increasing pH, which implies more active sites available for this route. Assuming that the 31 % of the contributions in acidic solution is attributed to graphitic-N sites, 6 to 8 % of the contributions in alkaline and neutral media are assigned to pyridinic and pyrrolic-N sites.

Table 4.10. Contribution of ORR 2- and 4-electron pathway in GO in acidic, alkaline and neutral electrolyte solutions.

ORR pathway	Electrolyte solution		
	0.1 M H ₂ SO ₄	0.1 M KOH	PBS pH 7.4
2-electron pathway	69 %	62 %	63 %
4-electron pathway	31 %	39 %	37 %
<i>n</i> electrons	2.62	2.77	2.75

4.3.3. METAL AND N-DOPING OF GRAPHENE OXIDE

Recalling the mechanism proposed in Figure 4.18, the cathodic reduction of oxygen in aqueous electrolytes can proceed by two overall pathways: 4 and 2-electron transfer. However, experimentally, the ORR occurs in a more complex way, being composed by several contributions of functional groups in the electrocatalysts: (i) N-groups, namely pyridinic-N and graphitic-N groups, (ii) metal active sites and (iii) carbon active spots. Several reports have described high activity of N-rGO materials in alkaline and acidic media, obtaining a 4-electron pathway [87-90]. Interestingly, the catalytic behaviour of N-groups in N-rGO is similar to the ORR performance discussed for ORR, *i.e.*, in acidic medium, the protonation of N-groups on the edges of the basal plane is responsible for the low catalytic activity of these groups, leaving graphitic-N in the carbon structure active for ORR. Although it would be expected a low number of electrons transferred in acidic solution, the N-catalytic activity is significative.

Considering the ORR polarization curves of the rGO-doped materials with atomically dispersed metals, Figure 4.27(a) shows the LSV curves of rGO/Fe 2 % in 0.1 M H₂SO₄. Analogous to GO, the current densities in an air-saturated 0.1 M H₂SO₄ solution increase with the rotation speed that indicates the movement of oxygen species into the surface of the catalysts.

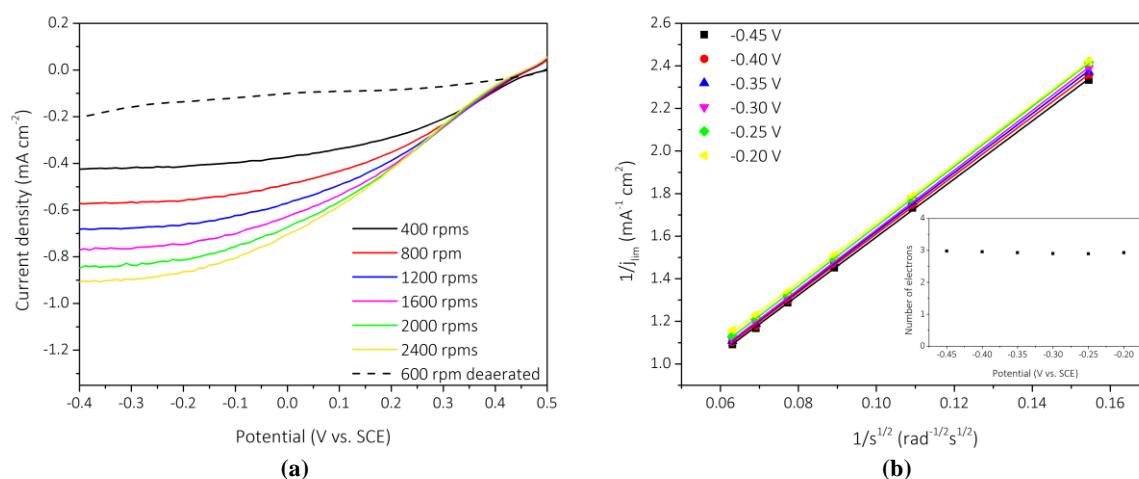


Figure 4.27. (a) Polarization curves of rGO/Fe 2 % on GC modified electrode in N₂ and air-saturated 0.1 M H₂SO₄ solution at different rotation speed at 10 mV s⁻¹ and (b) correspondent K-L plots at several potentials.

From the K-L plots at different potentials in Figure 4.27(b), it is possible to study the kinetics of the rGO/Fe 2 % as catalysts for ORR, resulting in a first order reaction controlled by kinetics and mass transport of reactants to the surface of the electrode. The estimated number of electrons transferred during ORR between -0.20 and -0.45 V vs. SCE is 2.95, in 0.1 M H₂SO₄.

A similar polarization curves are observed for rGO/Fe 2 % in alkaline and neutral media, as shown in Figure 4.28. The average *n* was determined to be 3.03 and 3.04 in 0.1 M KOH and 0.01 M PBS,

respectively. The slight increase of the number of electrons transferred is assigned to the increase of the metal and N-catalytic activity of the doped graphene in alkaline and neutral media.

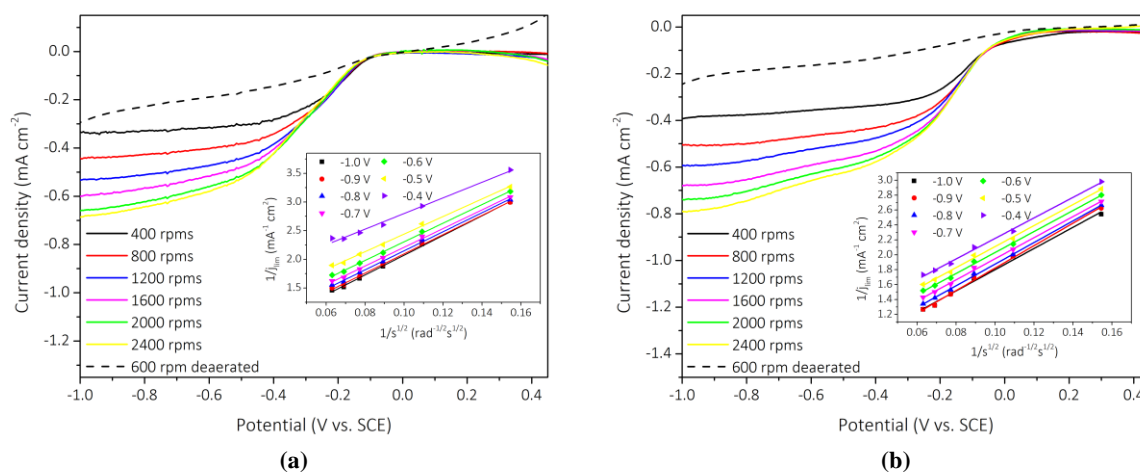


Figure 4.28. Polarization curves of rGO/Fe 2 % in a GC rotating disk electrode recorded at different rotation rates for ORR N₂ and air-saturated (a) 0.1 M KOH and (b) 0.01 M PBS, at 10 mV s⁻¹. Inset: Koutecký-Levich plots at different potentials.

The determined number of electrons by K-L plots is *c.a.* 3 for the three media that implies a mixed 2- and 4-electron reduction of oxygen and Table 4.11 shows the contributions of both routes calculated by Equation (4.2). As expected, in all the electrolyte solutions, the 2- and 4-electron pathway are *c.a.* 50/50 %, that described a highly active structure for the formation of peroxide species by carbon active sites (as discussed before) and water molecules. As the 4-electron contribution is not entirely associated to iron atoms activity but also to active N-sites, the attribution of each of these sites is only possible considering another metal system that reduces oxygen by a 2-electron pathway, such as a cobalt material.

Table 4.11. Contribution of ORR 2- and 4-electron pathway in rGO/Fe 2 % and rGO/Co 2 % in acidic, alkaline and neutral electrolyte solutions.

Material	ORR pathway	Electrolyte solution		
		0.1 M H ₂ SO ₄	0.1 M KOH	PBS pH 7.4
rGO/Fe 2 %	2-electron pathway	53 %	48 %	48 %
	4-electron pathway	47 %	52 %	52 %
	<i>n</i> electrons	2.95	3.03	3.04
rGO/Co 2 %	2-electron pathway	94 %	44 %	20 %
	4-electron pathway	6 %	56 %	80 %
	<i>n</i> electrons	2.13	3.12	3.60

Figure 4.29(a) illustrates the LSV of rGO/Co 2 % at different rotation speeds in aqueous acidic solution, showing similar curves at high overpotentials due to the mass transport of reactants to the surface of the electrode. The K-L plots are shown in Figure 4.29(b) and a first order reaction is ascribed to the rGO/Co 2 % electrode. Furthermore, by the K-L equation, the average number of electrons were estimated to be 2.13.

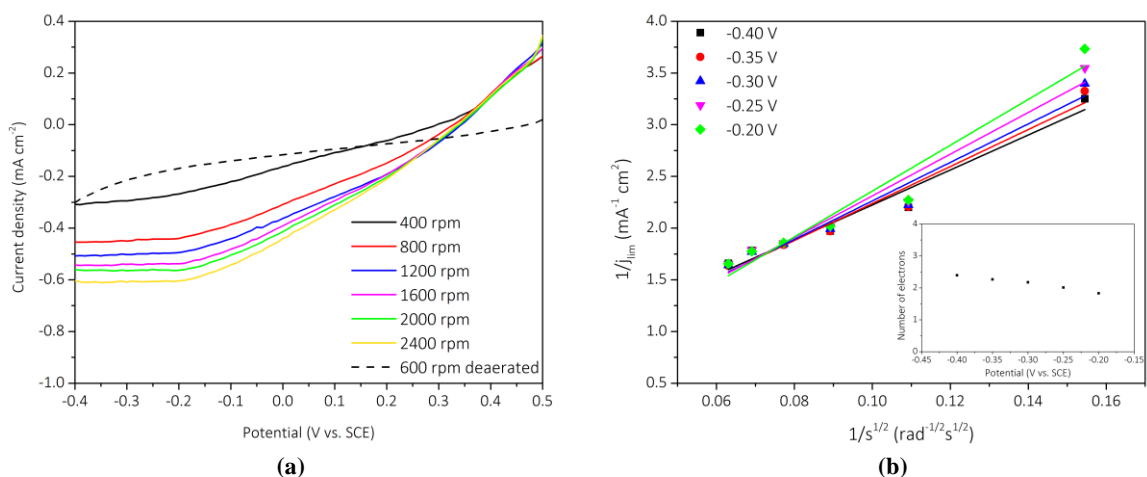


Figure 4.29. (a) Polarization curves of rGO/Co 2 % on GC modified electrode in N_2 and air-saturated 0.1 M H_2SO_4 solution at different rotation speed at 10 mV s^{-1} and (b) correspondent K-L plots at several potentials.

A similar ORR performance was done in alkaline and neutral solutions, using rGO/Co 2 % as electrode (Figure 4.30). The K-L plots correspondent to the polarization curves obtained allowed the determination of the number of electrons which are 3.12 and 3.60 in 0.1 M KOH and 0.01 M PBS, respectively. Considering a mixed 2- and 4-electron pathway, the contributions of both reactions are depicted in Table 4.11.

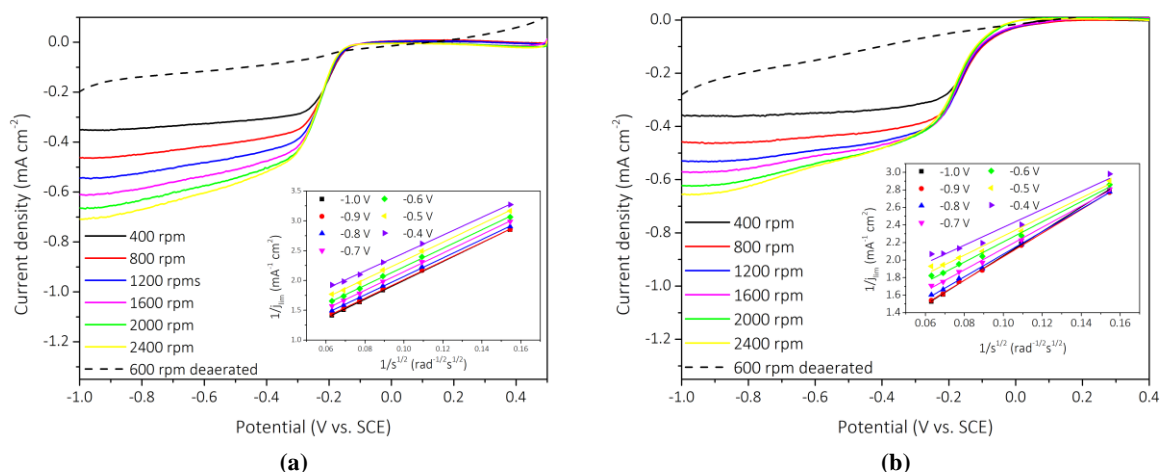


Figure 4.30. Polarization curves of rGO/Co 2 % in a GC rotating disk electrode recorded at different rotation rates for ORR N_2 and air-saturated (a) 0.1 M KOH and (b) 0.01 M PBS, at 10 mV s^{-1} . Inset: Koutecký-Levich plots at different potentials.

Considering the ORR contributions in acidic medium (Table 4.11) and assuming that both materials possess the same N-carbon structure, it is assumed that the 4-electron contribution in rGO/Co 2 % is entirely assigned to N-active sites, as cobalt and carbon only contribute with 2-electrons. Thus, the 4-electron contribution of the iron metal for the ORR can be calculated by:

$$b_{Fe} - b_{Co} = 47 \% - 6 \% = 41 \%,$$

and, in an analogous way, the determination of the 2-electron contribution of cobalt is given by

$$a_{Co} - a_{Fe} = 94 \% - 53 \% = 41 \%$$

Surprisingly, the contributions of iron and cobalt atoms are equal, which might imply same quantity of transition metal inside of the carbon structure. Table 4.12 shows the distribution of all the

contributions of metal, N- and C-active sites in the three electrolyte solutions for rGO/Fe 2 % and rGO/Co 2 %.

Table 4.12. Contribution of ORR 2- and 4-electron pathway in rGO/Fe 2 % and rGO/Co 2 % in acidic, alkaline and neutral electrolyte solutions. The metal, nitrogen and carbon contributions are denoted as *M*, *N* and *C*, respectively.

Material	ORR pathway	Electrolyte solution											
		0.1 M H ₂ SO ₄				0.1 M KOH				PBS pH 7.4			
		Total	M	N	C	Total	M	N	C	Total	M	N	C
rGO/Fe 2%	2-electron	53 %	41	6	53	48 %	4	48	48	48 %	28	24	48
	4-electron	47 %				52 %				52 %			
	<i>n</i> electrons		2.95				3.03				3.04		
rGO/Co 2%	2-electron	94 %	41	6	53	44 %	4	56	40	20 %	0	80	20
	4-electron	6 %				56 %				80 %			
	<i>n</i> electrons		2.13				3.12				3.60		

4.3.4. MACROCYCLE-DOPING OF GRAPHENE OXIDE

Biomimetics of biological molecules such as vitamin B₁₂ have been of great interest, not only because of their biocompatibility but also for their high activity towards ORR. It had been known that the type of the central metal atom is a dominant factor for the ORR performance, and in acid electrolyte, the reduction activity would decrease in the following order: Fe > Co > Ni > Cu > Mn [171]. Although more complex materials, the reduction of oxygen is analogous to the dispersed atom metals, as the reduction of oxygen is achieved by the contribution of the metal center, N-types and carbon sites. In this discussion, it will be assumed that the nitrogen atoms in the carbon structure inserted during the pyrolysis treatment under N₂ atmosphere contribute only with 4-electron pathway and the carbon structure reduces oxygen by 2-electron transference. Furthermore, the contribution of the remaining nitrogen atoms in the M-N₄ structure and the metal active sites will be determined comparing the macrocycle with the corresponding rGO/M material.

Considering the ORR polarization curves of the rGO-doped materials with M-N₄ molecules. Figure 4.31(a) shows the polarization curves of rGO/FeP 2 % in 0.1 M H₂SO₄. A typical LSV is observed for a RDE measurement, in which the current densities in an air-saturated 0.1 M H₂SO₄ solution increase with the rotation speed that indicates the movement of oxygen species into the surface of the catalysts. The corresponding K-L plots at different potentials are depicted in Figure 4.31(b), from which the number of electrons *n* was computed at different potentials.

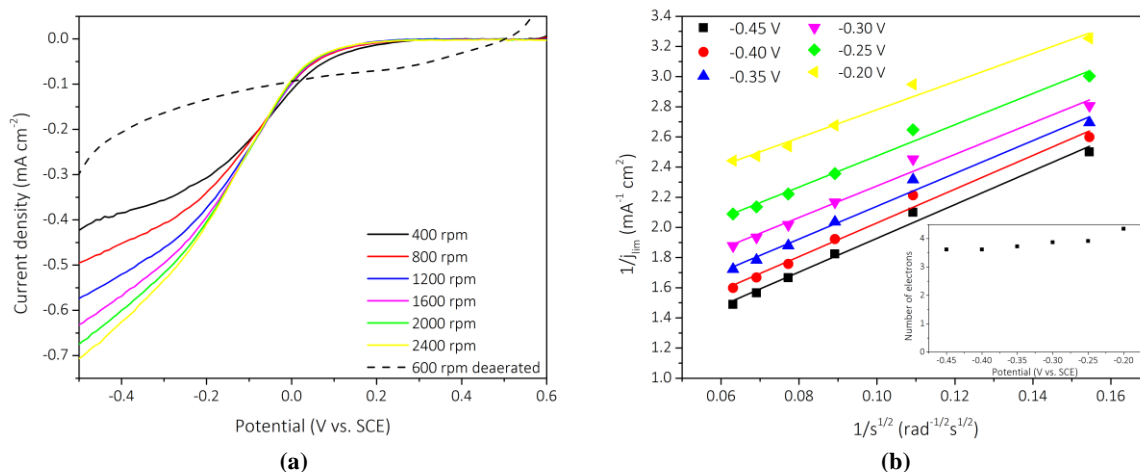


Figure 4.31. (a) Polarization curves of rGO/FeP 2% on GC modified electrode in N_2 and air-saturated 0.1 M H_2SO_4 solution at different rotation speed at 10 mV s^{-1} and (b) correspondent K-L plots at several potentials.

From the slopes of the K-L plots from -0.20 to -0.45 V vs. SCE, the average n transferred during ORR was estimated to be 3.85, which indicates a predominant 4-electron reduction of oxygen. The linearity and parallelism of the K-L plot imply a first order reaction controlled by kinetics and mass transport of oxygen species to the electrode surface. An analogous polarization plots are observed for rGO/FeP in alkaline and neutral solutions as shown in Figure 4.32(a) and (b), respectively. The average n was determined to be 4.07 for both electrolyte solutions.

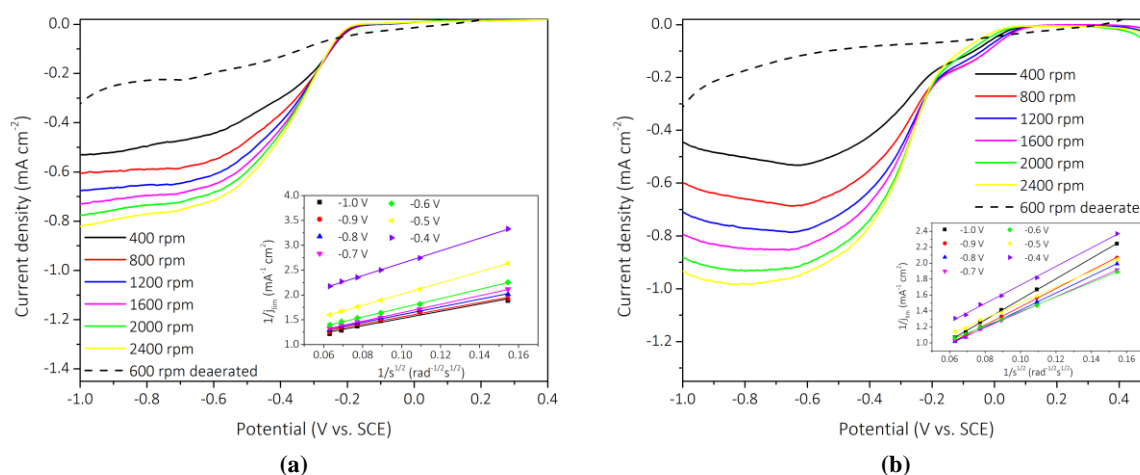


Figure 4.32. Polarization curves of rGO/FeP 2% in a GC rotating disk electrode recorded at different rotation rates for ORR N_2 and air-saturated (a) 0.1 M KOH and (b) 0.01 M PBS, at 10 mV s^{-1} . Inset: Koutecký-Levich plots at different potentials.

The average number calculated by the K-L plots is 3.85-4.07 that correspondent to a predominant 4-electron reduction of oxygen. Table 4.13 shows the possible contributions of both 2- and 4-electron pathway determined by Equation (4.2), showing a lower percentage of 2-electron pathway compared to 4-electron route (7% and 93%). The contribution of the 4-electron pathway is composed by two active sites: metal sites and N-active sites whose attribution of activity can only be assigned considering a 2-electron pathway metal system, such as cobalt. Furthermore, in order to distinguish N-doping graphene from N-active sites inside the M-N₄ molecule, a comparison between the activity of rGO/FeP with rGO/Fe 2%, whose N-atoms are only associated to the pyrolysis treatment, is performed.

Table 4.13. Contribution of ORR 2- and 4-electron pathway in rGO/FeP, rGO/CoP and rGO/VB₁₂ in acidic, alkaline and neutral electrolyte solutions.

Material	ORR pathway:	Electrolyte solution		
		0.1 M H ₂ SO ₄	0.1 M KOH	PBS pH 7.4
rGO/FeP	2-electron pathway	7 %	0 %	0 %
	4-electron pathway	93 %	100 %	100 %
	<i>n</i> electrons	3.85	4.07	4.07
rGO/CoP	2-electron pathway	85 %	6 %	20 %
	4-electron pathway	15 %	94 %	80 %
	<i>n</i> electrons	2.31	3.88	3.60
rGO/VB ₁₂	2-electron pathway	83 %	13 %	38 %
	4-electron pathway	17 %	87 %	62 %
	<i>n</i> electrons	2.34	3.74	3.24

Considering the polarization curves of rGO/CoP at different rotation speed in aqueous acidic medium, illustrated in Figure 4.33(a). At high overpotentials, the mass transport of oxygen species to the surface of the electrode is observed by the increasing of the diffusion-limiting current density as the rotation speed increases. The K-L plots at different potentials are shown in Figure 4.33(b), in which the slope of the curve is used for the determination of the average number of electrons transferred during the reduction. In acidic solution, *n* was determined to be 2.31 which implies a predominant 2-electron pathway.

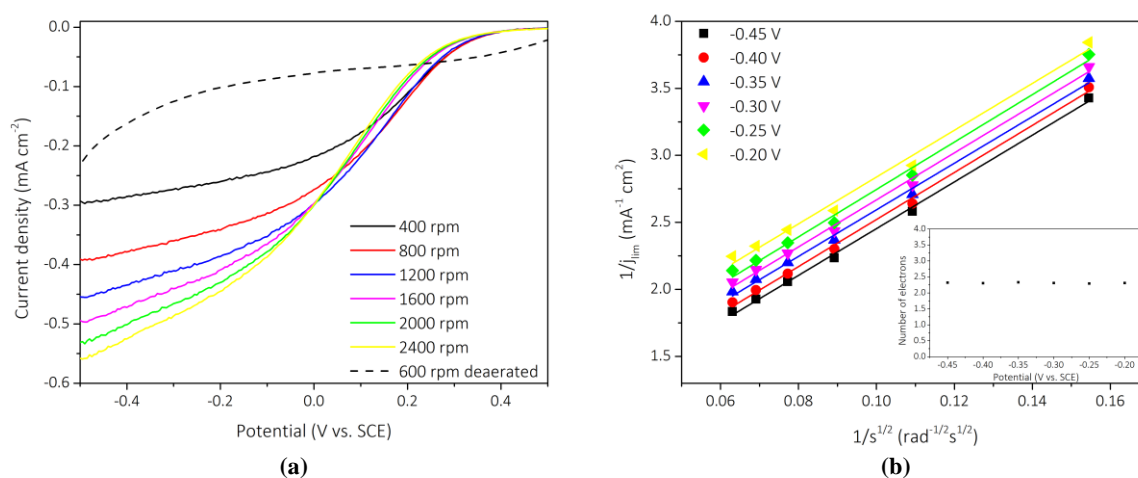


Figure 4.33. (a) Polarization curves of rGO/CoP 2 % on GC modified electrode in N₂ and air-saturated 0.1 M H₂SO₄ solution at different rotation speed at 10 mV s⁻¹ and (b) correspondent K-L plots at several potentials.

The polarization curves for rGO/CoP in alkaline and neutral media are shown in Figure 4.34. A similar shape is observed, although the limiting current density is higher than in acidic medium. The transferred number of electrons, calculated by the K-L equation, was 3.88 and 3.60 in alkaline and neutral media, respectively, which was expected as the increase of pH value allow the deprotonation of N-active sites, that are essential for the 4-electron transfer.

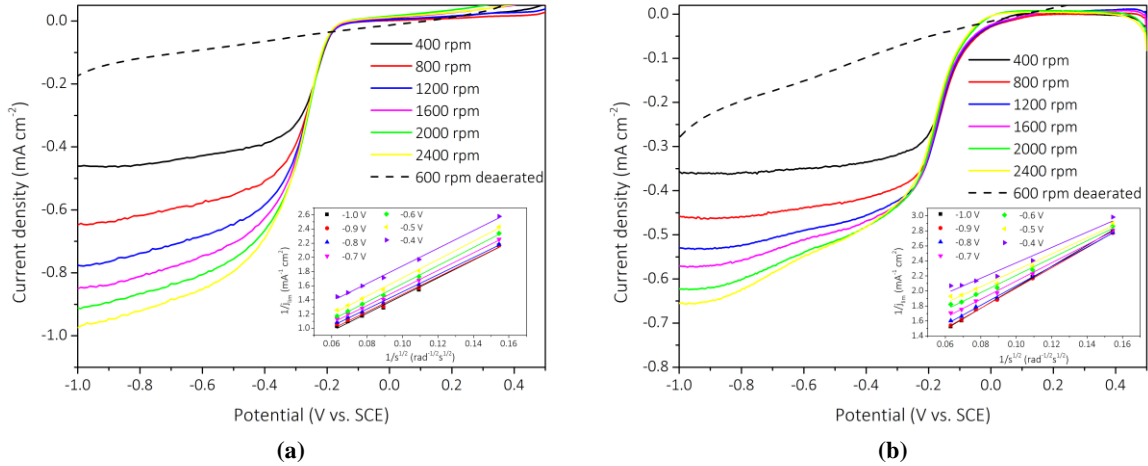


Figure 4.34. Polarization curves of rGO/CoP 2 % in a GC rotating disk electrode recorded at different rotation rates for ORR N₂ and air-saturated (a) 0.1 M KOH and (b) 0.01 M PBS, at 10 mV s⁻¹. Inset: Koutecký-Levich plots at different potentials.

Apart from the cobalt porphyrin, the hybrid material containing vitamin B₁₂ was also studied in the reduction of oxygen. The polarization curves of rGO/VB₁₂ and the corresponding K-L plots in acidic, alkaline and neutral media are depicted in the Figure 4.35. The average number of electrons calculated by K-L equation is 2.34, 3.74 and 3.24 in acidic, alkaline and neutral electrolyte solutions, respectively, which indicates a predominant 2-electron pathway in acidic medium and a 4-electron route in alkaline and neutral media. The contributions of the active sites in the rGO/VB₁₂ are shown in Table 4.13 and 4.14.

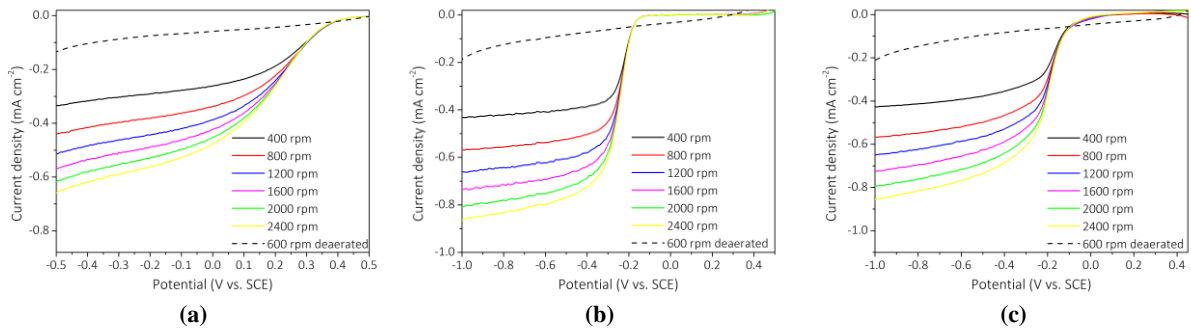


Figure 4.35. Polarization curves of rGO/VB₁₂ 2 % in a GC rotating disk electrode recorded at different rotation rates for ORR N₂ and air-saturated (a) 0.1 M H₂SO₄, (b) 0.1 M KOH and (c) 0.01 M PBS, at 10 mV s⁻¹. Inset: Koutecký-Levich plots at different potentials.

Although the predominance of 2- and 4-electron pathways, the contribution of both reactions in all the electrolyte solutions is shown in Table 4.13. Assuming similar carbon structure, the contribution of 4-electron pathway in rGO/CoP are entirely associated to N-active sites. Thus, the contribution of the iron metal center of the macrocycle is given by

$$b_{FeP} - b_{CoP} = 93 \% - 15 \% = 78 \%,$$

and, in an analogous way, the 2-electron pathway in rGO/FeP is assigned only to carbon structure, the contribution of cobalt is given by

$$a_{CoP} - a_{FeP} = 85 \% - 7 \% = 78 \%.$$

A similar calculation is done for the contributions of all the active sites in alkaline and neutral media for rGO/FeP, rGO/CoP and rGO/VB₁₂.

Table 4.14. Contribution of ORR 2- and 4-electron pathway in rGO/FeP, rGO/CoP and rGO/VB₁₂ in acidic, alkaline and neutral electrolyte solutions.

Material	ORR pathway:	Electrolyte solution											
		0.1 M H ₂ SO ₄				0.1 M KOH				PBS pH 7.4			
		Total	M	N	C	Total	M	N	C	Total	M	N	C
rGO/FeP	2-electron	7 %	78	15	7	0 %	13	87	0	0 %	100	0	0
	4-electron	93 %				100 %				100 %			
	<i>n</i> electrons		3.85			4.07			4.07				
rGO/CoP	2-electron	85 %	78	15	7	6 %	0	94	6	20 %	0	50	50
	4-electron	15 %				94 %				80 %			
	<i>n</i> electrons		2.31			3.88			3.60				
rGO/VB ₁₂	2-electron	83 %	76	17	7	13 %	5	87	8	38 %	0	50	50
	4-electron	17 %				87 %				62 %			
	<i>n</i> electrons		3.24			3.74			3.24				

So far, the contributions of the active sites were done by comparison of the 2- and 4-electrons pathway in similar materials. However, comparing the contributions of nitrogen between the rGO/M 2 % and the rGO/P 2 %, it is possible to access a new information about the N-doping of the carbon structure by pyrolysis. For example, considering that the carbon structure and the N-doping by pyrolysis of rGO/Fe 2 % and rGO/FeP are similar. It was already established that the contribution of N-type in the rGO/Fe 2 % and rGO/FeP is 6 % and 15 % respectively. Thus, the contribution of N-site from the macrocycle is given by

$$b_{FeP} - b_{Fe} = 15 \% - 6 \% = 9 \%,$$

and the contribution of N-doping corresponds to 6 %. Tables 4.15 shows the contributions of all the active sites, including the distinction of N-active sites for all the materials in 0.1 M H₂SO₄, 0.1 M KOH and 0.01 M PBS solutions.

Table 4.15. Electrocatalytic activity of the GC rotating ring-disk electrode modified with rGO-based materials in 0.1 M H₂SO₄ solution and the contributions of active sites in the material. The potentials values correspond to the onset potential and half-wave potential values vs. SCE (the potentials in brackets are assigned to the potentials vs. reversible hydrogen electrode (RHE) at 25 °C).

Sample	E _{onset} (V) ^a	I _{lim} (mA cm ⁻²) ^b	E _{half} (V) ^c	<i>n</i>	Contributions of active sites			
					4-electron			2-electron
					Metal	N-doping	M-N _x	C-sites
GO	0.05 (0.37)	-0.3459	-0.12 (0.20)	2.62	—	31 %	—	69 %
rGO/Fe 2 %	0.44 (0.76)	-0.5723	-0.34 (-0.02)	2.95	41 %	6 %	—	53 %
rGO/Co 2 %	0.31 (0.63)	-0.4544	0.18 (0.50)	2.13	41 %	6 %	—	53 %
rGO/FeP	0.12 (0.44)	-0.4520	-0.10 (0.22)	3.85	78 %	6 %	9 %	7 %
rGO/CoP	0.35 (0.67)	-0.3788	0.13 (0.44)	2.31	78 %	6 %	9 %	7 %
rGO/VB ₁₂	0.40 (0.71)	-0.4166	0.20 (0.52)	2.34	76 %	6 %	11 %	7 %

^a At -0.40 V vs SCE and 800 rpm, calculated considering the potential at which the current density reaches 5 % of the limiting current density.

^b Obtained at -0.40 V vs. SCE and 800 rpm.

^c Calculated by the difference between the onset potential and the potential at -0.40 V.

As a hydrodynamic electroanalytical technique, the rotating disk electrode has several advantages such as the fast establishment of a high rate of steady-state mass transport and easy and reproducible

controlled convection over a wide range of mass transfer coefficients [172]. However, the electrodes construction is complex, and the geometry of the RDE is critical to the quality of the results. The system in study is composed by a GC electrode modified with modified rGO materials, immobilized by drop casting method. Despite its simple procedure, the coating of the electrode surface and the thickness of the layer is not uniform (Figure 4.36). Moreover, the theoretical treatment requires the determination of the solution flow parameters, such as kinematic viscosities, densities and diffusion of oxygen in the solution [172].

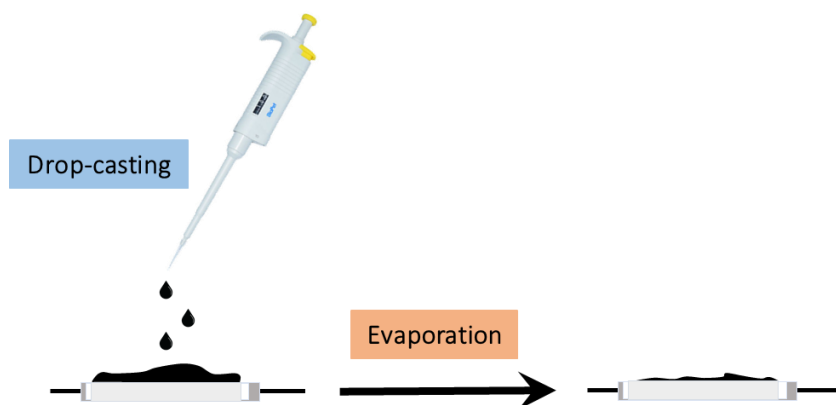
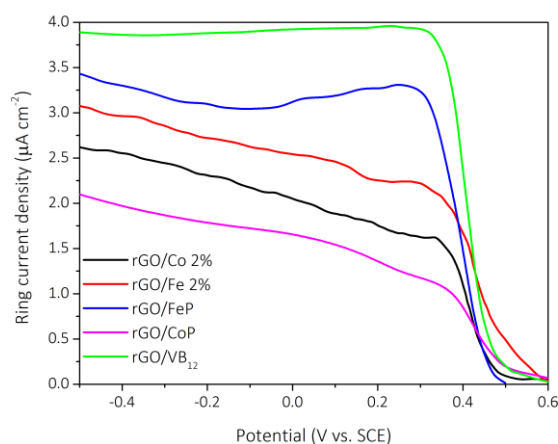


Figure 4.36. Schematic of the sequential steps of depositing modified rGO electrocatalysts in the surface of an electrode using drop-casting technique.

4.3.5. ROTATING RING-DISK ELECTRODE ON ORR

The detection and quantification of peroxide species formed in the disk is analysed by the rotating ring-disk electrode technique. The RRDE measurement was performed in the surface of an Au/Au RRDE modified with rGO/M 2 % and rGO/P 2 %, M= Fe and Co and P = FeP, CoP and VB₁₂, in an air-saturated 0.1 M H₂SO₄ solution. Figure 4.37 shows the polarization curves obtained by RRDE for the Au/Au rotating ring-disk modified electrode, at 600 rpm. The potential of the ring was set at 0.9 V vs. SCE, which is considered to be a sufficiently high potential to oxidize peroxide species.



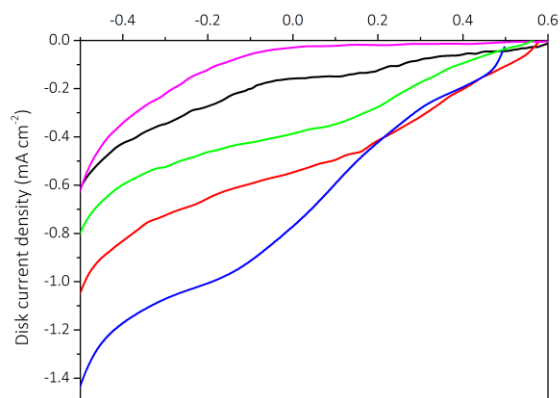


Figure 4.37. Polarization curves of rGO/M 2 % and rGO/P 2 %, M= Fe and Co and P = FeP, CoP and VB₁₂ in an Au/Au rotating ring-disk electrode recorded at 600 rpm for ORR in air-saturated 0.1 M H₂SO₄, at 10 mV s⁻¹ (Bottom figure); Ring potential 0.9 V vs. SCE (Upper figure)

A significant ring current density was observed for all the materials, corresponding to the formation of peroxide species during the reduction of oxygen, in acidic medium. However, the obtained ring current is not completely assigned to the material, as the deposited film of the catalysts on the Au is not homogeneous and, consequently, the Au electrode surface is not fully covered (Figure 4.38). This observation may be assigned to the high hydrophilicity of the modified rGO materials in the surface of the Au electrode.

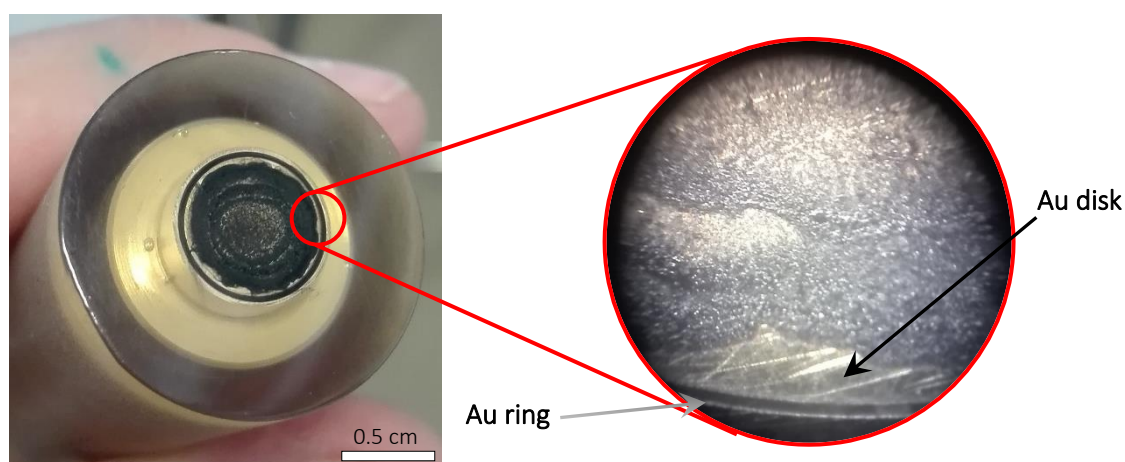


Figure 4.38. Picture of the Au/Au RRDE modified with a rGO/M electrocatalysts, highlighting a heterogeneous film of material in the disk electrode surface.

Comparing the disk polarization curves in Au/Au electrode and in the GC electrode of rGO/M and P 2 % materials, the disk current density in the modified Au disk is higher than the current measured for GC modified electrode, assigned to exposure of gold electrode that was not modified with the material. Furthermore, rGO/Fe 2 % and rGO/FeP exhibited the highest current density due to the 4-electron pathway.

4.3.6. ORR ELECTROCHEMICAL KINETICS

The Tafel slope has been used as a kinetic parameter in the mechanism of ORR, determining the feasibility of the electrode material used. At equilibrium, the kinetics of ORR follow the complete Butler-Volmer equation. At high overpotentials, $|\eta| > 50$ mV, the current density of oxygen reduction is described by the cathodic branch of the Tafel equation.

In the literature, several works have reported Tafel slopes from 32 to 125 mV dec⁻¹, as shown in Table A1 to A5, in which a low value of the slope, *c.a.* 60 mV dec⁻¹, corresponds to a multiple-electron reaction as the rate-determining step (RDS), whereas a high value of *b*, *c.a.* 120 mV dec⁻¹, suggests the first-electron reduction of oxygen as RDS. Figure 4.39 shows the Tafel plots of rGO/M 2 % and rGO/P 2 % in 0.1 M H₂SO₄. The determined Tafel slope is marked on the figure.

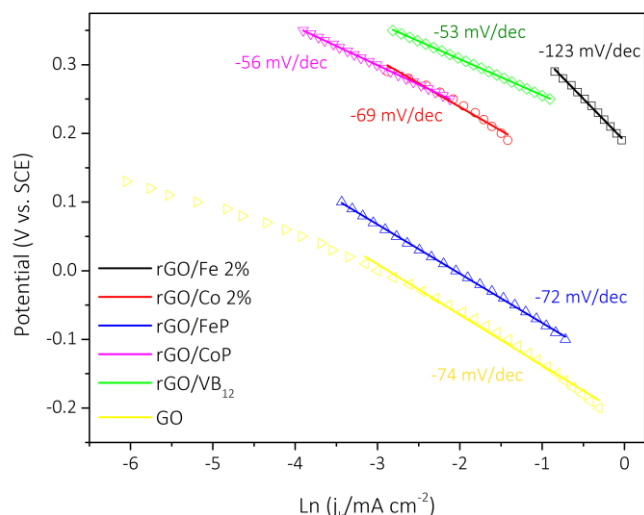


Figure 4.39. Tafel plots of rGO/M 2 % and rGO/P 2 %, M = Fe and Co and P = FeP, CoP and VB₁₂ in 0.1 M H₂SO₄ solution and at 800 rpm.

The obtained Tafel plots of GO is 74 mV dec⁻¹, while the rGO-doped materials exhibited a higher slope of 72, 69, 56 and 53 mV dec⁻¹ assigned to rGO/FeP, rGO/Co 2 %, rGO/CoP and rGO/VB₁₂, respectively, that is indicative of a multiple-electron transfer process of ORR on the electrode surface. The rGO/Fe 2 % exhibited a Tafel slope of 123 mV dec⁻¹ that is characteristic a first electron rate determining step. Comparing these results with the Tafel slope of a platinum-based electrode, such as Pt/C *c.a.* 92 mV dec⁻¹ [42], the mechanism of ORR on the modified rGO materials surface is kinetically similar.

Conclusions and future perspectives

In this work, new abiotic electrocatalysts incorporated on reduced graphene oxide, based on 2 and 10 wt % single metal atomically dispersed in the carbon structure for ORR were developed. The synthesis of the materials followed a simple and eco-friendly procedure, based on the production of a highly active surface mesoporous material capable of reducing oxygen. The produced modified rGO materials were obtained by the reduction of GO during a thermal process and plasma treatment that provided different materials, concerning nitrogen doping and GO reduction.

The insertion of macrocycle aromatic molecules in rGO was also performed using an adapted protocol described previously in literature. The π - π interactions between metalloporphyrins and the aromatic structure of rGO allowed the synthesis of stabilized rGO/P 2 % hybrid material. The reduction of the GO structure was analogous to the process of rGO/M x %, in which the materials were subjected to a pyrolysis treatment under N₂ atmosphere.

A full physical, chemical and elemental characterization techniques were performed in order to understand the rGO/M and P 2 and 10 wt % carbon structures, revealing a highly dispersed nanofilm of single graphene layers with *c.a.* 0.3 nm of thickness. The oxidation and reduction processes were monitored by FT-IR analysis, in which the intensity of peaks assigned to oxygen containing functional groups are evaluated. Furthermore, an enhanced specific surface area of the materials is observed, when compared to the commercial graphene, that is assigned to the creation of porosity during oxidation of the graphene. The nitrogen and metal content in the rGO structure were also investigated and a relatively low content of both species is estimated by XPS and BET analysis (*c.a.* 1.98 wt % N in M1 and 0.37 wt % in M1 and 0.046 wt % in M2 of metal).

Concerning the ORR, the electrochemical characterization of the materials was performed using hydrodynamic convective systems by RDE and RRDE in acidic, alkaline and neutral media. The polarization curves of the modified rGO materials showed high ORR catalytic activity of iron and cobalt based rGO-materials in all electrolyte solutions, concerning the onset potential and estimated number of electrons. The electrochemical performance was assigned to different functional groups in the electrocatalysts: the nitrogen, metal and carbon groups, that reduce oxygen differently, and the attribution of each functionality was possible. It is believed that synergistic effects between metal and nitrogen atoms was essential for the enhancement of the ORR performance. All the electrochemical analyses were supported by previous physical and chemical characterization.

Further research on the applicability of the modified rGO materials as electrocatalysts for the cathodic half-reaction of a biofuel cell is imperative. Firstly, a deeper insight of the developed synthesis of atomically dispersed transition metal in rGO is crucial to optimize the conditions of doping and reduction of GO, monitoring the procedure with physical and chemical characterization. Concerning the electrochemical reaction and taking in advantage of the interaction between carbon materials, the implementation of a new coating method of the GC electrode surface with the catalysts deserves to be studied as the RDE and RRDE methods depend on the homogeneity of the electrode surface.

Supplementary investigation on the mechanism of ORR catalysed by modified rGO catalysts is required for the improvement of new abiotic cathodes, as well as the study of the stability of such material in a long term.

Bibliography

1. Joung, Y. H., Development of Implantable Medical Devices: From an Engineering Perspective. *International Neurourology Journal* **2013**, *17*, 98-106.
2. Zebda, A.; Alcaraz, J. P.; Vadgama, P.; Shleev, S.; Minter, S. D.; Boucher, F.; Cinquin, P.; Martin, D. K., Challenges for Successful Implantation of Biofuel Cells. *Bioelectrochemistry* **2018**, *124*, 57-72.
3. Kakkar, V., An Ultra Low Power System Architecture for Implantable Medical Devices. *IEEE Access* **2018**, 1-1.
4. Lind, D. K., Understanding the Market for Implantable Medical Devices. *Insight on the Issues* **2017**, *129*.
5. Khan, W.; Muntimadugu, E.; Jaffe, M.; Domb, A. J., Implantable Medical Devices. In *Focal Controlled Drug Delivery* **2014**; 33-59.
6. Sanetuntikul, J.; Hyun, S.; Ganesan, P.; Shanmugam, S., Cobalt and Nitrogen Co-Doped Hierarchically Porous Carbon Nanostructure: A Bifunctional Electrocatalyst for Oxygen Reduction and Evolution Reactions. *Journal of Materials Chemistry A* **2018**, *6*, 24078-24085.
7. Falk, M.; Andoralov, V.; Blum, Z.; Sotres, J.; Suyatin, D. B.; Ruzgas, T.; Arnebrant, T.; Shleev, S., Biofuel Cell as a Power Source for Electronic Contact Lenses. *Biosensors and Bioelectronics*, **2012**, *37*, 38-45.
8. Bartsch, C.; Irnich, W., Aktive Implantierbare Medizinische Geräte. *Rechtsmedizin* **2011**, *21*, 493-504.
9. Bazaka, K.; Jacob, M., Implantable Devices: Issues and Challenges. *Electronics* **2012**, *2*, 1-34.
10. E. Meng, R. S., Insight: Implantable Medical Devices. *Lab on a Chip* **2014**, *14*, 3233-3240.
11. Amar, B., A.; Kouki, A. B.; Cao, H., Power Approaches for Implantable Medical Devices. *Sensors* **2015**, *15*, 28889-914.
12. Tan, H.; Li, Y.; Jiang, X.; Tang, J.; Wang, Z.; Qian, H.; Mei, P.; Malgras, V.; Bando, Y.; Yamauchi, Y., Perfectly Ordered Mesoporous Iron-Nitrogen Doped Carbon as Highly Efficient Catalyst for Oxygen Reduction Reaction in Both Alkaline and Acidic Electrolytes. *Nano Energy* **2017**, *36*, 286-294.
13. Cosnier, S.; Gross, A. J.; Goff, A. L.; Holzinger, M., Recent Advances on Enzymatic Glucose/Oxygen and Hydrogen/Oxygen Biofuel Cells: Achievements and Limitations. *Journal of Power Sources* **2016**, *325*, 252-263.
14. Cinquin P, Gondran C, Giroud F, Mazabrard S, Pellissier A, Boucher F, A Glucose BioFuel Cell Implanted in Rats. *PLoS ONE* **2010**, *5(5)* e10476
15. Falk, M.; Narvaez Villarrubia, C. W.; Babanova, S.; Atanassov, P.; Shleev, S., Biofuel Cells for Biomedical Applications: Colonizing the Animal Kingdom. *Chemphyschem* **2013**, *14*, 2045-58.
16. Cosnier, S.; Le Goff, A.; Holzinger, M., Towards Glucose Biofuel Cells Implanted in Human Body for Powering Artificial Organs: Review. *Electrochemistry Communications* **2014**, *38*, 19-23.
17. Si, F.; Zhang, Y.; Yan, L.; Zhu, J.; Xiao, M.; Liu, C.; Xing, W.; Zhang, J., 4-Electrochemical Oxygen Reduction Reaction. In *Rotating Electrode Methods and Oxygen Reduction Electrocatalysts*, Xing, W.; Yin, G.; Zhang, J., Eds. Elsevier, **2014**, 133-170.

18. Liu, Y.; Huang, B.; Zhang, X.; Huang, X.; Xie, Z., In-Situ Fabrication of Nitrogen-Doped Carbon Nanosheets Containing Highly Dispersed Single Iron Atoms for Oxygen Reduction Reaction. *Journal of Power Sources* **2019**, *412*, 125-133.
19. Premkumar, V.; Chandrasekaran, N.; Madasamy, K.; Kathiresan, M.; Kanagavalli, P.; Senthil Kumar, S., Iron Oxide Decorated N-Doped Carbon Derived from Poly(Ferrocene-Urethane) Interconnects for the Oxygen Reduction Reaction. *New Journal of Chemistry* **2018**, *42*, 15629-15638.
20. Karunagaran, R.; Coghlan, C.; Tung, T. T.; Kabiri, S.; Tran, D. N. H.; Doonan, C. J.; Losic, D., Study of Iron Oxide Nanoparticle Phases in Graphene Aerogels for Oxygen Reduction Reaction. *New Journal of Chemistry* **2017**, *41*, 15180-15186.
21. Abroshan, H.; Bothra, P.; Back, S.; Kulkarni, A.; Nørskov, J. K.; Siahrostami, S., Ultrathin Cobalt Oxide Overlayer Promotes Catalytic Activity of Cobalt Nitride for the Oxygen Reduction Reaction. *The Journal of Physical Chemistry C* **2018**, *122*, 4783-4791.
22. Kulkarni, A.; Siahrostami, S.; Patel, A.; Norskov, J. K., Understanding Catalytic Activity Trends in the Oxygen Reduction Reaction. *Chemical Reviews* **2018**, *118*, 2302-2312.
23. Kakaei, K.; Esrafil, M. D.; Ehsani, A., Chapter 6-Oxygen Reduction Reaction. In *Graphene Surfaces, Particles and Catalysts*. Kakaei, K.; Esrafil, M. D.; Ehsani, A., Eds. Elsevier **2019**, *27*, 203-252.
24. Huang, X.; Wang, Y.; Li, W.; Hou, Y., Noble Metal-Free Catalyst for Oxygen Reduction Reaction. *Science China Chemistry* **2017**, *60*, 19-22.
25. Zhong, H.; Gong, X.; Zhang, S.; Tang, P.; Li, D.; Feng, Y., Design and Synthesis of Cobalt-Based Electrocatalysts for Oxygen Reduction Reaction. *The Chemical Record* **2018**, *18*, 840-848.
26. Ramaswamy, N.; Mukerjee, S., Fundamental Mechanistic Understanding of Electrocatalysis of Oxygen Reduction on Pt and Non-Pt Surfaces: Acid Versus Alkaline Media. *Advances in Physical Chemistry* **2012**, *2012*, 1-17.
27. Lide, D. R., *Crc Handbook of Chemistry and Physics*, 90th Edition; CRC Press/Taylor and Francis, Boca Raton, Interned Version 2010.
28. Si, F.; Zhang, Y.; Yan, L.; Zhu, J.; Xiao, M.; Liu, C.; Xing, W.; Zhang, J., Electrochemical Oxygen Reduction Reaction. In *Rotating Electrode Methods and Oxygen Reduction Electrocatalysts*, Wei Xing, G. Y., Jiujun Zhang, Ed. Elsevie, **2014**, 133-170.
29. Sui, S.; Wang, X.; Zhou, X.; Su, Y.; Riffat, S.; Liu, C.-j., A Comprehensive Review of Pt Electrocatalysts for the Oxygen Reduction Reaction: Nanostructure, Activity, Mechanism and Carbon Support in Pem Fuel Cells. *Journal of Materials Chemistry A* **2017**, *5*, 1808-1825.
30. Tang, Z.; Wu, W.; Wang, K., Oxygen Reduction Reaction Catalyzed by Noble Metal Clusters. *Catalysts* **2018**, *8*, 65.
31. Norskov, J. K.; Rossmeisl, J.; Logadottir, A.; Lindqvist, L., Origin of the Overpotential for Oxygen Reduction at a Fuel-Cell Cathode. *The Journal of Physical Chemistry B* **2004**, *108*, 17887-17892.
32. Yeager, E., *Electrocatalysis on Non-Metallic Surfaces*; NBS Special Publication: U.S. Department of Commerce, Washington, DC, **1976**, 455, 203-219
33. Kinoshita, K., *Electrochemical Oxygen Technology*; John Wiley & Sons, INC, **1992**.

34. Wroblowa, H. S.; Pan, Y. C.; Razumney, G., Electro-Reduction of Oxygen: A New Mechanistic Criterion. *Journal of Electroanalytical Chemistry* **1976**, *69*, 195-201.
35. Li, J.-C.; Tang, D.-M.; Hou, P.-X.; Li, G.-X.; Cheng, M.; Liu, C.; Cheng, H.-M., The Effect of Carbon Support on the Oxygen Reduction Activity and Durability of Single-Atom Iron Catalysts. *MRS Communications* **2018**, *8*, 1158-1166.
36. Li, J.-C.; Yang, Z.-Q.; Tang, D.-M.; Zhang, L.; Hou, P.-X.; Zhao, S.-Y.; Liu, C.; Cheng, M.; Li, G.-X.; Zhang, F.; Cheng, H.-M., N-Doped Carbon Nanotubes Containing a High Concentration of Single Iron Atoms for Efficient Oxygen Reduction. *NPG Asia Materials* **2018**, *10*, e461.
37. Liu, Y.-L.; Xu, X.-Y.; Shi, C.-X.; Ye, X.-W.; Sun, P.-C.; Chen, T.-H., Iron–Nitrogen Co-Doped Hierarchically Mesoporous Carbon Spheres as Highly Efficient Electrocatalysts for the Oxygen Reduction Reaction. *RSC Advances* **2017**, *7*, 8879-8885.
38. Yan, Z.; Dai, C.; Zhang, M.; Lv, X.; Zhao, X.; Xie, J., Nitrogen Doped Porous Carbon with Iron Promotion for Oxygen Reduction Reaction in Alkaline and Acidic Media. *International Journal of Hydrogen Energy* **2019**, *44*, 4090-4101.
39. Yan, Z.; Dai, C.; Lv, X.; Zhang, M.; Zhao, X.; Xie, J., Iron Promoted Nitrogen Doped Porous Graphite for Efficient Oxygen Reduction Reaction in Alkaline and Acidic Media. *Journal of Alloys and Compounds* **2019**, *773*, 819-827.
40. Zhou, T.; Ma, R.; Zhang, T.; Li, Z.; Yang, M.; Liu, Q.; Zhu, Y.; Wang, J., Increased Activity of Nitrogen-Doped Graphene-Like Carbon Sheets Modified by Iron Doping for Oxygen Reduction. *Journal of Colloid and Interface Science* **2019**, *536*, 42-52.
41. Ratso, S.; Käärrik, M.; Kook, M.; Paiste, P.; Kisand, V.; Vlassov, S.; Leis, J.; Tammeveski, K., Iron and Nitrogen Co-Doped Carbide-Derived Carbon and Carbon Nanotube Composite Catalysts for Oxygen Reduction Reaction. *ChemElectroChem* **2018**, *5*, 1827-1836.
42. Lu, Z.; Liu, B.; Dai, W.; Ouyang, L.; Ye, J., Carbon Network Framework Derived Iron-Nitrogen Co-Doped Carbon Nanotubes for Enhanced Oxygen Reduction Reaction through Metal Salt-Assisted Polymer Blowing Strategy. *Applied Surface Science* **2019**, *463*, 767-774.
43. Sohail, M.; Saleem, M.; Ullah, S.; Saeed, N.; Afridi, A.; Khan, M.; Arif, M., Modified and Improved Hummer's Synthesis of Graphene Oxide for Capacitors Applications. *Modern Electronic Materials* **2017**, *3*, 110-116.
44. Kaur, M.; Kaur, H.; Kukkar, D., Synthesis and Characterization of Graphene Oxide Using Modified Hummer's Method. *AIP Conference Proceedings* **2018**, *1953*, 030180.
45. Zaaba, N. I.; Foo, K. L.; Hashim, U.; Tan, S. J.; Liu, W.-W.; Voon, C. H., Synthesis of Graphene Oxide Using Modified Hummers Method: Solvent Influence. *Procedia Engineering* **2017**, *184*, 469-477.
46. Dreyer, D. R.; Park, S.; Bielawski, C. W.; Ruoff, R. S., The Chemistry of Graphene Oxide. *Chemical Society Reviews* **2010**, *39*, 228-40.
47. Park, S.; Ruoff, R. S., Chemical Methods for the Production of Graphenes. *Nature Nanotechnology* **2009**, *4*, 217-24.

48. Toh, S. Y.; Loh, K. S.; Kamarudin, S. K.; Daud, W. R. W., Graphene Production Via Electrochemical Reduction of Graphene Oxide: Synthesis and Characterisation. *Chemical Engineering Journal* **2014**, *251*, 422-434.
49. Huang, C.; Li, C.; Shi, G., Graphene Based Catalysts. *Energy Environmental Science* **2012**, *5*, 8848-8868.
50. Filip, J.; Tkac, J., Is Graphene Worth Using in Biofuel Cells? *Electrochimica Acta* **2014**, *136*, 340-354.
51. Jo, J.; Lee, S.; Gim, J.; Song, J.; Kim, S.; Mathew, V.; Alfaruqi, M. H.; Kim, S.; Lim, J.; Kim, J., Facile Synthesis of Reduced Graphene Oxide by Modified Hummer's Method as Anode Material for Li-, Na- and K-Ion Secondary Batteries. *Royal Society Open Science* **2019**, *6*, 181978.
52. Cao, N.; Zhang, Y., Study of Reduced Graphene Oxide Preparation by Hummers' Method and Related Characterization. *Journal of Nanomaterials* **2015**, *2015*, 1-5.
53. Kumar, N. A.; Gambarelli, S.; Duclairoir, F.; Bidan, G.; Dubois, L., Synthesis of High Quality Reduced Graphene Oxide Nanosheets Free of Paramagnetic Metallic Impurities. *Journal of Materials Chemistry A* **2013**, *1*, 2789-2794.
54. Saleem, H.; Haneef, M.; Abbasi, H. Y., Synthesis Route of Reduced Graphene Oxide Via Thermal Reduction of Chemically Exfoliated Graphene Oxide. *Materials Chemistry and Physics* **2018**, *204*, 1-7.
55. Chang, W.-T.; Chao, Y.-H.; Li, C.-W.; Lin, K.-L.; Wang, J.-J.; Kumar, S. R.; Lue, S. J., Graphene Oxide Synthesis Using Microwave-Assisted Vs. Modified Hummer's Methods: Efficient Fillers for Improved Ionic Conductivity and Suppressed Methanol Permeability in Alkaline Methanol Fuel Cell Electrolytes. *Journal of Power Sources* **2019**, *414*, 86-95.
56. Hummers, W. S.; Offeman, R. E., Preparation of Graphitic Oxide. *Journal of the American Chemical Society* **1958**, *80*, 1339.
57. Bosch-Navarro, C.; Coronado, E.; Marti-Gastaldo, C.; Sanchez-Royo, J. F.; Gomez, M. G., Influence of the Ph on the Synthesis of Reduced Graphene Oxide under Hydrothermal Conditions. *Nanoscale* **2012**, *4*, 3977-82.
58. Dimiev, A. M.; Tour, J. M., Mechanism of Graphene Oxide Formation. *ACS Nano* **2014**, *8*, 3060-3068.
59. Liang, J.; Jiao, Y.; Jaroniec, M.; Qiao, S. Z., Sulfur and Nitrogen Dual-Doped Mesoporous Graphene Electrocatalyst for Oxygen Reduction with Synergistically Enhanced Performance. *Angewandte Chemie International Edition* **2012**, *51*, 11496-11500.
60. Kim, H.; Lee, K.; Woo, S. I.; Jung, Y., On the Mechanism of Enhanced Oxygen Reduction Reaction in Nitrogen-Doped Graphene Nanoribbons. *Physical Chemistry Chemical Physics* **2011**, *13*, 17505-17510.
61. Lee, J. Y.; Kim, N. Y.; Shin, D. Y.; Park, H.-Y.; Lee, S.-S.; Joon Kwon, S.; Lim, D.-H.; Bong, K. W.; Son, J. G.; Kim, J. Y., Nitrogen-Doped Graphene-Wrapped Iron Nanofragments for High-Performance Oxygen Reduction Electrocatalysts. *Journal of Nanoparticle Research* **2017**, *19*(98).
62. Ferrero, G. A.; Diez, N.; Sevilla, M.; Fuertes, A. B., Iron-Nitrogen-Doped Dendritic Carbon Nanostructures for an Efficient Oxygen Reduction Reaction. *ACS Applied Energy Materials* **2018**, *1*, 6560-6568.

63. Miao, H.; Li, S.; Wang, Z.; Sun, S.; Kuang, M.; Liu, Z.; Yuan, J., Enhancing the Pyridinic N Content of Nitrogen-Doped Graphene and Improving Its Catalytic Activity for Oxygen Reduction Reaction. *International Journal of Hydrogen Energy* **2017**, *42*, 28298-28308.
64. Ning, X.; Li, Y.; Ming, J.; Wang, Q.; Wang, H.; Cao, Y.; Peng, F.; Yang, Y.; Yu, H., Electronic Synergism of Pyridinic- and Graphitic-Nitrogen on N-Doped Carbons for the Oxygen Reduction Reaction. *Chemical Science* **2019**, *10*, 1589-1596.
65. Tan, H.; Tang, J.; Kim, J.; Kaneti, Y. V.; Kang, Y.-M.; Sugahara, Y.; Yamauchi, Y., Rational Design and Construction of Nanoporous Iron- and Nitrogen-Doped Carbon Electrocatalysts for Oxygen Reduction Reaction. *Journal of Materials Chemistry A* **2019**, *7*, 1380-1393.
66. Du, D.; Li, P.; Ouyang, J., Nitrogen-Doped Reduced Graphene Oxide Prepared by Simultaneous Thermal Reduction and Nitrogen Doping of Graphene Oxide in Air and Its Application as an Electrocatalyst. *ACS Appl Mater Interfaces* **2015**, *7*, 26952-26958.
67. Li, X.; Wang, H.; Robinson, J. T.; Sanches, H.; Diankov, G.; Dai, H., Simultaneous Nitrogen Doping and Reduction of Graphene Oxide. *Journal of the American Chemical Society* **2009**, *131*, 15939-15944.
68. Li, X.; Zhang, B.; Yan, X.; Zhang, Y.; Deng, X.; Zhang, S., Fe,N-Doped Graphene Prepared by NH_3 Plasma with a High Performance for Oxygen Reduction Reaction. *Catalysis Today* **2019**, *337*, 97-101.
69. Zhou, H. P.; Ye, X.; Huang, W.; Wu, M. Q.; Mao, L. N.; Yu, B.; Xu, S.; Levchenko, I.; Bazaka, K., Wearable, Flexible, Disposable Plasma-Reduced Graphene Oxide Stress Sensors for Monitoring Activities in Austere Environments. *ACS Applied Materials & Interfaces* **2019**, *11*, 15122-15132.
70. Lee, B.-J.; Shin, D.-H.; Lee, S.; Jeong, G.-H., Revealing Impact of Plasma Condition on Graphite Nanostructures and Effective Charge Doping of Graphene. *Carbon* **2017**, *123*, 174-185.
71. Dave, K.; Park, K. H.; Dhayal, M., Two-Step Process for Programmable Removal of Oxygen Functionalities of Graphene Oxide: Functional, Structural and Electrical Characteristics. *RSC Advances* **2015**, *5*, 95657-95665.
72. Ossoinon, B. D.; Bélanger, D., Synthesis and Characterization of Sulfophenyl-Functionalized Reduced Graphene Oxide Sheets. *RSC Advances* **2017**, *7*, 27224-27234.
73. Xu, S.; Zhang, Z.; Liu, J.; Wang, Y.; Hu, J., Facile Preparation of Reduced Graphene by Optimizing Oxidation Condition and Further Reducing the Exfoliated Products. *Journal of Materials Research* **2016**, *32*, 383-391.
74. Kauppila, J.; Kunnas, P.; Damlin, P.; Viinikanoja, A.; Kvarnström, C., Electrochemical Reduction of Graphene Oxide Films in Aqueous and Organic Solutions. *Electrochimica Acta* **2013**, *89*, 84-89.
75. Peng, X.-Y.; Liu, X.-X.; Diamond, D.; Lau, K. T., Synthesis of Electrochemically-Reduced Graphene Oxide Film with Controllable Size and Thickness and Its Use in Supercapacitor. *Carbon* **2011**, *49*, 3488-3496.
76. Ramachandran, R.; Felix, S.; Joshi, M. G.; Raghupathy, P. C. B.; Jeong, K. S.; Grace, N. A., Synthesis of Graphene Platelets by Chemical and Electrochemical Route. *Materials Research Bulletin* **2013**, *48*, 3834-3842.

77. Ma, Y.; Wang, Q.; Miao, Y.; Lin, Y.; Li, R., Plasma Synthesis of Pt Nanoparticles on 3d Reduced Graphene Oxide-Carbon Nanotubes Nanocomposites Towards Methanol Oxidation Reaction. *Applied Surface Science* **2018**, *450*, 413-421.
78. Lee, S. W.; Mattevi, C.; Chhowalla, M.; Sankaran, R. M., Plasma-Assisted Reduction of Graphene Oxide at Low Temperature and Atmospheric Pressure for Flexible Conductor Applications. *The Journal of Physical Chemistry Letters* **2012**, *3*, 772-777.
79. Kim, M. J.; Jeong, Y.; Sohn, S.; Lee, S. Y.; Kim, Y. J.; Lee, K.; Kahng, Y. H.; Jang, J.-H., Fast and Low-Temperature Reduction of Graphene Oxide Films Using Ammonia Plasma. *AIP Advances* **2013**, *3*, 012117.
80. Kumar, N. A.; Nolan, H.; McEvoy, N.; Rezvani, E.; Doyle, R. L.; Lyons, M. E. G.; Duesberg, G. S., Plasma-Assisted Simultaneous Reduction and Nitrogen Doping of Graphene Oxide Nanosheets. *Journal of Materials Chemistry A* **2013**, *1*, 4431-4435.
81. Zhu, T.; Li, S.; Ren, B.; Zhang, L.; Dong, L.; Tan, L., Plasma-Induced Synthesis of Boron and Nitrogen Co-Doped Reduced Graphene Oxide for Super-Capacitors. *Journal of Materials Science* **2019**, *54*, 9632-9642.
82. Chien, H.-H.; Cheng, Y.-C.; Hao, Y.-C.; Hsu, C.-C.; Cheng, I. C.; Yu, I.-S.; Chen, J.-Z., Nitrogen DC-Pulse Atmospheric-Pressure-Plasma Jet (APPJ)-Processed Reduced Graphene Oxide (rGO)-Carbon Black (CB) Nanocomposite Electrodes for Supercapacitor Applications. *Diamond and Related Materials* **2018**, *88*, 23-31.
83. Dey, A.; Chronos, A.; Braithwaite, N. S. J.; Gandhiraman, R. P.; Krishnamurthy, S., Plasma Engineering of Graphene. *Applied Physics Reviews* **2016**, *3*, 021301.
84. Chen, J.; Zhu, C.; Xu, Y.; Zhang, P.; Liang, T., Advances in Phthalocyanine Compounds and Their Photochemical and Electrochemical Properties. *Current Organic Chemistry* **2018**, *22*, 485-504.
85. Ouyang, B.; Zhang, Y.; Xia, X.; Rawat, R. S.; Fan, H. J., A Brief Review on Plasma for Synthesis and Processing of Electrode Materials. *Materials Today Nano* **2018**, *3*, 28-47.
86. Bodik, M.; Zahoranova, A.; Micusik, M.; Bugarova, N.; Spitalsky, Z.; Omastova, M.; Majkova, E.; Jergel, M.; Siffalovic, P., Fast Low-Temperature Plasma Reduction of Monolayer Graphene Oxide at Atmospheric Pressure. *Nanotechnology* **2017**, *28(14)*, 145601.
87. Dong, Y.; Deng, Y.; Zeng, J.; Song, H.; Liao, S., A High-Performance Composite Orr Catalyst Based on the Synergy between Binary Transition Metal Nitride and Nitrogen-Doped Reduced Graphene Oxide. *Journal of Materials Chemistry A* **2017**, *5*, 5829-5837.
88. Li, C.; Chen, Z.; Kong, A.; Ni, Y.; Kong, F.; Shan, Y., High-Rate Oxygen Electroreduction over Metal-Free Graphene Foams Embedding P-N Coupled Moieties in Acidic Media. *Journal of Materials Chemistry A* **2018**, *6*, 4145-4151.
89. Lu, X.; Wang, D.; Ge, L.; Xiao, L.; Zhang, H.; Liu, L.; Zhang, J.; An, M.; Yang, P., Enriched Graphitic N in Nitrogen-Doped Graphene as a Superior Metal-Free Electrocatalyst for the Oxygen Reduction Reaction. *New Journal of Chemistry* **2018**, *42*, 19665-19670.
90. Zhang, B.; Wang, C.; Liu, D.; Liu, Y.; Yu, X.; Wang, L., Boosting Orr Electrocatalytic Performance of Metal-Free Mesoporous Biomass Carbon by Synergism of Huge Specific Surface Area and Ultrahigh Pyridinic Nitrogen Doping. *ACS Sustainable Chemistry & Engineering* **2018**, *6*, 13807-13812.

91. Guo, J.; Cheng, Y.; Xiang, Z., Confined-Space-Assisted Preparation of Fe₃O₄-Nanoparticle-Modified Fe–N–C Catalysts Derived from a Covalent Organic Polymer for Oxygen Reduction. *ACS Sustainable Chemistry & Engineering* **2017**, *5*, 7871-7877.
92. Zhao, J.; Li, C.; Liu, R., Enhanced Oxygen Reduction of Multi-Fe₃O₄@Carbon Core-Shell Electrocatalysts through a Nanoparticle/Polymer Co-Assembly Strategy. *Nanoscale* **2018**, *10*, 5882-5887.
93. Wang, H.; Wang, W.; Xu, Y. Y.; Dong, S.; Xiao, J.; Wang, F.; Liu, H.; Xia, B. Y., Hollow Nitrogen-Doped Carbon Spheres with Fe₃O₄ Nanoparticles Encapsulated as a Highly Active Oxygen-Reduction Catalyst. *ACS Applied Materials & Interfaces* **2017**, *9*, 10610-10617.
94. Chen, Z.; Lin, F.; He, D.; Jiang, H.; Zhang, J.; Wang, X.; Huang, M., A Hybrid Composite Catalyst of Fe₃O₄ Nanoparticles-Based Carbon for Electrochemical Reduction of Oxygen. *New Journal of Chemistry* **2017**, *41*, 4959-4965.
95. Zhang, Z.; Zhou, D.; Liao, J.; Bao, X.; Luo, S., One-Pot Synthesis of Fe₃O₄/Fe/C by Microwave Sintering as an Efficient Bifunctional Electrocatalyst for Oxygen Reduction and Oxygen Evolution Reactions. *Journal of Alloys and Compounds* **2019**, *786*, 134-138.
96. Liu, J.; Bao, H.; Zhang, B.; Hua, Q.; Shang, M.; Wang, J.; Jiang, L., Geometric Occupancy and Oxidation State Requirements of Cations in Cobalt Oxides for Oxygen Reduction Reaction. *ACS Applied Materials & Interfaces* **2019**, *11*, 12525-12534.
97. Xia, X.; Li, M.; Liu, T.; Liang, P.; Huang, X., Facile Synthesis of Cobalt Oxide as Electrocatalyst for the Oxygen Reduction Reaction in Microbial Fuel Cells. *Chemical Engineering Journal* **2018**, *342*, 395-400.
98. Xu, G.; Xu, G. C.; Ban, J. J.; Zhang, L.; Lin, H.; Qi, C. L.; Sun, Z. P.; Jia, D. Z., Cobalt and Cobalt Oxides N-Codoped Porous Carbon Derived from Metal-Organic Framework as Bifunctional Catalyst for Oxygen Reduction and Oxygen Evolution Reactions. *Journal of Colloid and Interface Science* **2018**, *521*, 141-149.
99. Chen, Y.; Li, L.; Liu, X.; Wan, W.; Luo, J., Synthesis of a Synergistic Catalyst for Oxygen Reduction and a Zn–Air Battery by the in Situ Coupling of Hemin-Derived Fe₃O₄/N-Doped Graphitic Carbon. *Materials Research Express* **2019**, *6(6)*, 065019.
100. Chen, P.; Zhou, T.; Xing, L.; Xu, K.; Tong, Y.; Xie, H.; Zhang, L.; Yan, W.; Chu, W.; Wu, C.; Xie, Y., Atomically Dispersed Iron-Nitrogen Species as Electrocatalysts for Bifunctional Oxygen Evolution and Reduction Reactions. *Angewandte Chemie International Edition* **2017**, *56*, 610-614.
101. Li, J.; Chen, M.; Cullen, D. A.; Hwang, S.; Wang, M.; Li, B.; Liu, K.; Karakalos, S.; Lucero, M.; Zhang, H.; Lei, C.; Xu, H.; Sterbinsky, G. E.; Feng, Z.; Su, D.; More, K. L.; Wang, G.; Wang, Z.; Wu, G., Atomically Dispersed Manganese Catalysts for Oxygen Reduction in Proton-Exchange Membrane Fuel Cells. *Nature Catalysis* **2018**, *1*, 935-945.
102. Chen, Y.; Ji, S.; Zhao, S.; Chen, W.; Dong, J.; Cheong, W. C.; Shen, R.; Wen, X.; Zheng, L.; Rykov, A. I.; Cai, S.; Tang, H.; Zhuang, Z.; Chen, C.; Peng, Q.; Wang, D.; Li, Y., Enhanced Oxygen Reduction with Single-Atomic-Site Iron Catalysts for a Zinc-Air Battery and Hydrogen-Air Fuel Cell. *Nature Communications* **2018**, *9*, 5422.

103. Yan, X.; Xu, X.; Liu, Q.; Guo, J.; Kang, L.; Yao, J., Functionalization of Multi-Walled Carbon Nanotubes with Iron Phthalocyanine Via a Liquid Chemical Reaction for Oxygen Reduction in Alkaline Media. *Journal of Power Sources* **2018**, *389*, 260-266.
104. Khandelwal, M.; Chandrasekaran, S.; Hur, S. H.; Chung, J. S., Chemically Controlled in-Situ Growth of Cobalt Oxide Microspheres on N,S-Co-Doped Reduced Graphene Oxide as an Efficient Electrocatalyst for Oxygen Reduction Reaction. *Journal of Power Sources* **2018**, *407*, 70-83.
105. Cheng, Q.; Yang, L.; Zou, L.; Zou, Z.; Chen, C.; Hu, Z.; Yang, H., Single Cobalt Atom and N Codoped Carbon Nanofibers as Highly Durable Electrocatalyst for Oxygen Reduction Reaction. *ACS Catalysis* **2017**, *7*, 6864-6871.
106. Zhang, Z.; Sun, J.; Wang, F.; Dai, L., Efficient Oxygen Reduction Reaction (Orr) Catalysts Based on Single Iron Atoms Dispersed on a Hierarchically Structured Porous Carbon Framework. *Angewandte Chemie International Edition* **2018**, *57*, 9038-9043.
107. Wang, X. X., et al., Nitrogen-Coordinated Single Cobalt Atom Catalysts for Oxygen Reduction in Proton Exchange Membrane Fuel Cells. *Advanced Materials* **2018**, *30*.
108. Liu, K.; Qiao, Z.; Hwang, S.; Liu, Z.; Zhang, H.; Su, D.; Xu, H.; Wu, G.; Wang, G., Mn- and N-Doped Carbon as Promising Catalysts for Oxygen Reduction Reaction: Theoretical Prediction and Experimental Validation. *Applied Catalysis B: Environmental* **2019**, *243*, 195-203.
109. Ferrero, G. A.; Diez, N.; Sevilla, M.; Fuertes, A. B., Iron/Nitrogen Co-Doped Mesoporous Carbon Synthesized by an Endo-Templating Approach as an Efficient Electrocatalyst for the Oxygen Reduction Reaction. *Microporous and Mesoporous Materials* **2019**, *278*, 280-288.
110. Park, H.; Oh, S.; Lee, S.; Choi, S.; Oh, M., Cobalt- and Nitrogen-Codoped Porous Carbon Catalyst Made from Core-Shell Type Hybrid Metal-Organic Framework (ZIF-L@ZIF-67) and Its Efficient Oxygen Reduction Reaction (ORR) Activity. *Applied Catalysis B: Environmental* **2019**, *246*, 322-329.
111. Chen, X.; Zhen, X.; Gong, H.; Li, L.; Xiao, J.; Xu, Z.; Yan, D.; Xiao, G.; Yang, R., Cobalt and Nitrogen Codoped Porous Carbon as Superior Bifunctional Electrocatalyst for Oxygen Reduction and Hydrogen Evolution Reaction in Alkaline Medium. *Chinese Chemical Letters* **2019**, *30*, 681-685.
112. Liu, X.; Li, W.; Zou, S., Cobalt and Nitrogen-Codoped Ordered Mesoporous Carbon as Highly Efficient Bifunctional Catalysts for Oxygen Reduction and Hydrogen Evolution Reactions. *Journal of Materials Chemistry A* **2018**, *6*, 17067-17074.
113. Liu, L.; Zhang, J.; Ma, W.; Huang, Y., Co/N Co-Doped Graphene-Like Nanocarbon for Highly Efficient Oxygen Reduction Electrocatalyst. *Science China Materials* **2018**, *62*, 359-367.
114. Tang, Y.; Liu, R.; Liu, S.; Zheng, B.; Lu, Y.; Fu, R.; Wu, D.; Zhang, M.; Rong, M., Cobalt and Nitrogen Codoped Ultrathin Porous Carbon Nanosheets as Bifunctional Electrocatalysts for Oxygen Reduction and Evolution. *Carbon* **2019**, *141*, 704-711.
115. Davari, E.; Ivey, D. G., Synthesis and Electrochemical Performance of Manganese Nitride as an Oxygen Reduction and Oxygen Evolution Catalyst for Zinc-Air Secondary Batteries. *Journal of Applied Electrochemistry* **2017**, *47*, 815-827.
116. Lai, Q.; Zhao, Y.; Zhu, J.; Liang, Y.; He, J.; Chen, J., Directly Anchoring Highly Dispersed Copper Sites on Nitrogen-Doped Carbon for Enhanced Oxygen Reduction Electrocatalysis. *ChemElectroChem* **2018**, *5*, 1822-1826.

117. Li, F.; Han, G.-F.; Noh, H.-J.; Kim, S.-J.; Lu, Y.; Jeong, H. Y.; Fu, Z.; Baek, J.-B., Boosting Oxygen Reduction Catalysis with Abundant Copper Single Atom Active Sites. *Energy & Environmental Science* **2018**, *11*, 2263-2269.
118. Xie, X.; Liu, J.; Li, T.; Song, Y.; Wang, F., Post-Formation Copper-Nitrogen Species on Carbon Black: Their Chemical Structures and Active Sites for Oxygen Reduction Reaction. *Chemistry - A European Journal* **2018**, *24*, 9968-9975.
119. Xie, Y.; Zhang, C.; He, X.; Su, J.-W.; Parker, T.; White, T.; Griep, M.; Lin, J., Copper-Promoted Nitrogen-Doped Carbon Derived from Zeolitic Imidazole Frameworks for Oxygen Reduction Reaction. *Applied Surface Science* **2019**, *464*, 344-350.
120. Zhao, Y.; Chu, Y.; Ju, X.; Zhao, J.; Kong, L.; Zhang, Y., Carbon-Supported Copper-Based Nitrogen-Containing Supramolecule as an Efficient Oxygen Reduction Reaction Catalyst in Neutral Medium. *Catalysts* **2018**, *8*, 53.
121. Czarnek, K.; Terpilowska, S.; Siwicki, A. K., Selected Aspects of the Action of Cobalt Ions in the Human Body. *Central European Journal of Immunology* **2015**, *40*, 236-242.
122. Tvermoes, B. E.; Finley, B. L.; Unice, K. M.; Otani, J. M.; Paustenbach, D. J.; Galbraith, D. A., Cobalt Whole Blood Concentrations in Healthy Adult Male Volunteers Following Two-Weeks of Ingesting a Cobalt Supplement. *Food Chem Toxicol* **2013**, *53*, 432-439.
123. Zagal, J. H.; Bedioui, F., *Electrochemistry of N4 Macrocyclic Metal Complexes*; Springer: Switzerland, **2016**, *1*.
124. Kim, D.-H.; Kwak, D.-H.; Han, S.-B.; Kim, M.-C.; Park, H.-S.; Park, J.-Y.; Won, J.-E.; Ma, K.-B.; Park, K.-W., Electrochemical Catalytic Contribution of Transition Metals at the Center of Porphyrin Macrocyclic Structures as Catalysts for Oxygen Reduction Reaction. *Journal of Industrial and Engineering Chemistry* **2017**, *54*, 200-204.
125. Liu, S.; Yang, Z.; Liu, L.; Li, M.; Wang, Y.; Lv, W.; Chen, X.; Zhao, X.; Zhu, P.; Wang, G., Metallic Iron Doped Vitamin B12/C as Efficient Nonprecious Metal Catalysts for Oxygen Reduction Reaction. *International Journal of Hydrogen Energy* **2018**, *43*, 16230-16239.
126. Fruehwald, H. M.; Ebralidze, I. I.; Zenkina, O. V.; Easton, E. B., Fe-N₃/C Active Catalytic Sites for the Oxygen Reduction Reaction Prepared with Molecular-Level Geometry Control through the Covalent Immobilization of an Iron-Terpyridine Motif onto Carbon. *ChemElectroChem* **2019**, *6*, 1350-1358.
127. Guo, J.; Yan, X.; Liu, Q.; Li, Q.; Xu, X.; Kang, L.; Cao, Z.; Chai, G.; Chen, J.; Wang, Y.; Yao, J., The Synthesis and Synergistic Catalysis of Iron Phthalocyanine and Its Graphene-Based Axial Complex for Enhanced Oxygen Reduction. *Nano Energy* **2018**, *46*, 347-355.
128. Hanana, M.; Arcostanzo, H.; Das, P. K.; Bouget, M.; Le Gac, S.; Okuno, H.; Cornut, R.; Jusselme, B.; Dorcet, V.; Boitrel, B.; Campidelli, S., Synergic Effect on Oxygen Reduction Reaction of Strapped Iron Porphyrins Polymerized around Carbon Nanotubes. *New Journal of Chemistry* **2018**, *42*, 19749-19754.
129. Huang, W.; Ahlfield, J. M.; Kohl, P. A.; Zhang, X., Heat Treated Tethered Iron Phthalocyanine Carbon Nanotube-Based Catalysts for Oxygen Reduction Reaction in Hybrid Fuel Cells. *Electrochimica Acta* **2017**, *257*, 224-232.

130. Liu, Y.; Fan, Y.-S.; Liu, Z.-M., Pyrolysis of Iron Phthalocyanine on Activated Carbon as Highly Efficient Non-Noble Metal Oxygen Reduction Catalyst in Microbial Fuel Cells. *Chemical Engineering Journal* **2019**, *361*, 416-427.
131. Xue, H.; He, T.; Chabu, J. M.; Liu, J.; Wu, H.; Zheng, J.; Tan, M.; Ma, J.; Shen, R.; Deng, L.; Zhang, Y., Iron Single Clusters Anchored on N-Doped Porous Carbon as Superior Trace-Metal Catalysts toward Oxygen Reduction. *Advanced Materials Interfaces* **2018**, *5*, 1701345.
132. Yan, X.; Xu, X.; Zhong, Z.; Liu, J.; Tian, X.; Kang, L.; Yao, J., The Effect of Oxygen Content of Carbon Nanotubes on the Catalytic Activity of Carbon-Based Iron Phthalocyanine for Oxygen Reduction Reaction. *Electrochimica Acta* **2018**, *281*, 562-570.
133. Zhang, Z.; Dou, M.; Ji, J.; Wang, F., Phthalocyanine Tethered Iron Phthalocyanine on Graphitized Carbon Black as Superior Electrocatalyst for Oxygen Reduction Reaction. *Nano Energy* **2017**, *34*, 338-343.
134. Zhang, Y.; Wu, H.; Zhao, W.; Li, X.; Yin, R.; Qian, L.; Qi, Y.; Yang, K., Iron (II) Phthalocyanine Nanoclusters - Graphene Sandwich Composite for Oxygen Reduction Reaction Catalysts. *Materials & Design* **2017**, *130*, 366-372.
135. Marianov, A. N.; Jiang, Y., Effect of Manganese Porphyrin Covalent Immobilization on Electrocatalytic Water Oxidation and Oxygen Reduction Reactions. *ACS Sustainable Chemistry & Engineering* **2019**, *7*, 3838-3848.
136. Yi, J.-D.; Xu, R.; Chai, G.-L.; Zhang, T.; Zang, K.; Nan, B.; Lin, H.; Liang, Y.-L.; Lv, J.; Luo, J.; Si, R.; Huang, Y.-B.; Cao, R., Cobalt Single-Atoms Anchored on Porphyrinic Triazine-Based Frameworks as Bifunctional Electrocatalysts for Oxygen Reduction and Hydrogen Evolution Reactions. *Journal of Materials Chemistry A* **2019**, *7*, 1252-1259.
137. Snitkoff, R. Z.; Levy, N.; Ozery, I.; Ruthstein, S.; Elbaz, L., Imidazole Decorated Reduced Graphene Oxide: A Biomimetic Ligand for Selective Oxygen Reduction Electrocatalysis with Metalloporphyrins. *Carbon* **2019**, *143*, 223-229.
138. You, J.-M.; Han, H. S.; Lee, H. K.; Cho, S.; Jeon, S., Enhanced Electrocatalytic Activity of Oxygen Reduction by Cobalt-Porphyrin Functionalized With Graphene Oxide in an Alkaline Solution. *International Journal of Hydrogen Energy* **2014**, *39*, 4803-4811.
139. Zhang, Y.; Liu, S.; Wang, L.; Liu, W.; Sun, R.; Ye, J., Cobalt Tetramethoxyphenylporphyrin Functionalized Graphene for Oxygen Reduction Reaction in Neutral Media. *Materials Letters* **2015**, *144*, 5-8.
140. Wang, M.; Wang, Q.; Zhu, W.; Yang, Y.; Zhou, H.; Zhang, F.; Zhou, L.; Razal, J. M.; Wallace, G. G.; Chen, J., Metal Porphyrin Intercalated Reduced Graphene Oxide Nanocomposite Utilized for Electrocatalytic Oxygen Reduction. *Green Energy & Environment* **2017**, *2*, 285-293.
141. Riquelme, J.; Neira, K.; Marco, J. F.; Hermosilla-Ibáñez, P.; Orellana, W.; Zagal, J. H.; Tasca, F., Biomimicking Vitamin B12. A Co Phthalocyanine Pyridine Axial Ligand Coordinated Catalyst for the Oxygen Reduction Reaction. *Electrochimica Acta* **2018**, *265*, 547-555.
142. Zagal, J. H.; Aguirre, M. J.; Páez, M. A., O₂ Reduction Kinetics on a Graphite Electrode Modified with Adsorbed Vitamin B12. *Journal of Electroanalytical Chemistry* **1997**, *437*, 45-52.

143. Pletcher, D.; Greff, R.; Peat, R.; Peter, L. M.; Robinson, J., *Instrumental Methods in Electrochemistry*, Woodhead Publishing, **2001**.
144. Bockis, J. O. M.; Khan, S. U. M., *Surface Electrochemistry: A Molecular Lever Approach*, Springer Science+Business Media, LLC, **1993**.
145. Bard, A. J.; Faulkner, L. R., *Electrochemical Methods. Fundamentals and Applications*, 2nd Ed.; John Wiley & Sons, INC, **2001**.
146. Treimer, S.; Tang, A.; Johnson, D. C., A Consideration of the Application of Koutecký-Levich Plots in the Diagnoses of Charge-Transfer Mechanisms at Rotated Disk Electrodes. *Electroanalysis* **2002**, *14*, 165-171.
147. Paulus, U. A.; Schmidt, T. J.; Gasteiger, H. A.; J., B. R., Oxygen Reduction on a High-Surface Area Pt/Vulcan Carbon Catalysts: A Thin-Film Rotating Ring-Disk Electrode Study. *Journal of Electroanalytical Chemistry* **2001**, *495*, 134-145.
148. Jiang, Y.; Ni, P.; Chen, C.; Lu, Y.; Yang, P.; Kong, B.; Fisher, A.; Wang, X., Selective Electrochemical H₂O₂ Production through Two-Electron Oxygen Electrochemistry. *Advanced Energy Materials* **2018**, *8*, 1801909.
149. Voigtländer, B., *Scanning Probe Microscopy - Atomic Force Microscopy and Scanning Tunneling Microscopy*. Springer, Germany, **2015**.
150. Haugstad, G., *Atomic Force Microscopy: Understanding Basic Modes and Advanced Applications*, John Wiley & Sons, Inc. **2012**.
151. Eaton, P.; West, P., *Atomic Force Microscopy*; Oxford University Press Inc., New York: United States, **2010**.
152. Hammond, K. D.; Conner, W. C., Analysis of Catalyst Surface Structure by Physical Sorption. **2013**, *56*, 1-101.
153. Galarneau, A.; Villemot, F.; Rodriguez, J.; Fajula, F.; Coasne, B., Validity of the T-Plot Method to Assess Microporosity in Hierarchical Micro/Mesoporous Materials. *Langmuir* **2014**, *30*, 13266-74.
154. Strem chemicals, INC Graphene nanoplatelets aggregates (sub-micron particles, surface area 750 m²/g) https://www.strem.com/catalog/v/06-0235/12/carbon_1034343-98-0 (Accessed in 15/09/2019).
155. Cai, M.; Thorpe, D.; Adamson, D. H.; Schniepp, H. C., Methods of Graphite Exfoliation. *Journal of Materials Chemistry* **2012**, *22*, 24992.
156. Schniepp, H. C.; Li, J. L.; McAllister, M. J.; Sai, H.; Herrera-Alonso, M.; Adamson, D. H.; Prud'homme, R. K.; Car, R.; Saville, D. A.; Aksay, I. A., Functionalized Single Graphene Sheets Derived from Splitting Graphite Oxide. *The Journal of Physical Chemistry B* **2006**, *110*, 8535-8539.
157. Banda, H. (2018) Development of graphene-Based composite materials for electrochemical storage applications. University of Grenoble Alpes, Grenoble, France.
158. Mendoza, M. E.; Ferreira, E. H. M.; Kuznetsov, A.; Achete, C. A.; Aumanen, J.; Myllyperkiö, P.; Johansson, A.; Pettersson, M.; Archanjo, B. S., Revealing Lattice Disorder, Oxygen Incorporation and Pore Formation in Laser Induced Two-Photon Oxidized Graphene. *Carbon* **2019**, *143*, 720-727.

159. Montaserin, C.; Blanco, M.; Aranzabe, E.; Aranzabe, A.; Laza, J. M.; Larranaga-Varga, A.; Vilas, J. L., Effects of Graphene Oxide and Chemically-Reduced Graphene Oxide on the Dynamic Mechanical Properties of Epoxy Amine Composites. *Polymers* **2017**, *9*(9), 449.
160. Jorio, A.; Dresslhaus, M.; Saito, R.; Dresslhaus, G. F., *Raman Spectroscopy in Graphene Related Systems*; WILEY-VCH, **2011**.
161. Li, J.; Song, Y.; Zhang, G.; Liu, H.; Wang, Y.; Sun, S.; Guo, X., Pyrolysis of Self-Assembled Iron Porphyrin on Carbon Black as Core/Shell Structured Electrocatalysts for Highly Efficient Oxygen Reduction in Both Alkaline and Acidic Medium. *Advanced Functional Materials* **2017**, *27*, 1604356.
162. Matter, P. H.; Biddinger, E. J.; Ozkan, U. S., Non-Precious Metal Oxygen Reduction Catalysts for Pem Fuel Cells. In *Catalysis*, Spivey, J. J.; Dooley, K. M., Eds. Royal Society of Chemistry 2007, *20*, 338-366.
163. Zhu, M.; Cao, C.; Chen, J.; Sun, Y.; Ye, R.; Xu, J.; Han, Y.-F., Electronic Tuning of Cobalt Porphyrins Immobilized on Nitrogen-Doped Graphene for CO₂ Reduction. *ACS Applied Energy Materials* **2019**, *2*, 2435-2440.
164. Almeida, I.; Mendo, S. G.; Carvalho, M. D.; Correia, J. P.; Viana, A. S., Catalytic Co and Fe Porphyrin/Fe₃O₄ Nanoparticles Assembled on Gold by Carbon Disulfide. *Electrochimica Acta* **2016**, *188*, 1-12.
165. Qu, L.; Liu, Y.; Baek, J.-B.; Dai, L., Nitrogen-Doped Graphene as Efficient Metal-Free Electrocatalyst for Oxygen Reduction in Fuel Cells. *ACS Nano* **2010**, *4*, 1321-1326.
166. Xing, W.; Yin, M.; Lv, Q.; Hu, Y.; Liu, C.; Zhang, J., Oxygen Solubility, Diffusion Coefficient, and Solution Viscosity. In *Rotating Electrode Methods and Oxygen Reduction Electrocatalysts*, Wei Xing, G. Y., Jiujun Zhang, Ed. Elsevier, **2014**, 1-31.
167. Feng, L.; Sun, X.; Yao, S.; Liu, C.; Xing, W.; Zhang, J., Electrocatalysts and Catalyst Layers for Oxygen Reduction Reaction. In *Rotating Electrode Methods and Oxygen Reduction Electrocatalysis*, Xing, W.; Yin, G.; Zhang, J., Eds. Elsevier, **2014**.
168. Ge, X.; Sumboja, A.; Wu, D.; An, T.; Li, B.; Goh, F. W. T.; Hor, T. S. A.; Zong, Y.; Liu, Z., Oxygen Reduction in Alkaline Media: From Mechanisms to Recent Advances of Catalysts. *ACS Catalysis* **2015**, *5*, 4643-4667.
169. Bikkarolla, S. K.; Cumpson, P.; Joseph, P.; Papakonstantinou, P., Oxygen Reduction Reaction by Electrochemically Reduced Graphene Oxide. *Faraday Discuss* **2014**, *173*, 415-28.
170. Kumar, K. V.; Preuss, K.; Guo, Z. X.; Titirici, M. M., Understanding the Hydrophilicity and Water Adsorption Behavior of Nanoporous Nitrogen-Doped Carbons. *The Journal of Physical Chemistry C* **2016**, *120*, 18167-18179.
171. Liu, K.; Lei, Y.; Chen, R.; Wang, G., Oxygen Electroreduction on M-N₄ Macrocyclic Complexes. In *Electrochemistry of N₄ Macrocyclic Metal Complexes*, 2nd Edition; Zagal, J. H.; Bedioui, F., Eds. Springer: Switzerland, **2016**, *1*, 1-40.
172. Denuault, G.; Sosna, M.; Williams, K.-J., Classical Experiments. In *Handbook of Electrochemistry*, Zoski, C. G., Ed. Elsevier, **2007**.

Appendix A

Table A.1. Electrocatalytic activity comparison of recent advances on iron-nitrogen co-doped carbon materials. The potentials values correspond to the onset potential and half-wave potential values vs. the reversible hydrogen electrode (RHE) at 25 °C.

Catalyst	Precursors	Methods	Electrolyte	E_{onset} (V)	$E_{1/2}$ (V)	Tafel slope (mV dec ⁻¹)	HO ₂ ⁻ yield (%)	n	Year&Ref.
CNT@Fe-N-C	CNTs; Pyrrole; Iron(III) nitrate; Zinc(II) nitrate	Hummer's method; Pyrolysis; Polymerization	0.1 M HClO ₄	Not given	0.82	68	< 3	4	2018, [35]
CNT@Fe-N-PC	CNTs; Iron(III) chloride; Zinc(II) nitrate	Pyrolysis; Polymerization; 2 nd pyrolysis	0.1 M HClO ₄	Not given	0.82	67	< 3		2018, [36]
SA-Fe-HPC	Cattle bone powder; unsubstituted phthalocyanine; Iron(II) phthalocyanine	Pyrolysis	0.1 M H ₂ SO ₄	Not given	0.81	Not given	–	4	2018, [106]
			0.1 M KOH		0.89				
Fe-N-CS-900	Mesoporous silica spheres; 2-aminopyridine; Iron(III) chloride	Polymerization; Pyrolysis at 900 °C	0.5 M H ₂ SO ₄	Not given	Not given	Not given	–	4	2017, [37]
			0.1 M KOH		0.309			84	
Fe-N _x -C (0.1 mmol of Fe)	Guanine; Iron(III) nitrate	Heat treatment; Pyrolysis	0.1 M KOH	0.93	0.85	74	2.3	4	2019, [18]
Fe-N _x -C (0.07 mmol of Fe)				0.92	0.82	86			
Fe-N-CNTs-800	Polyvinylpyrrolidone (PVP); Melamine; Iron(III) nitrate	Chemical blowing; Pyrolysis	0.1 M KOH	0.980	0.784	Not given	4.5	3.91	2019, [42]
Fe _{0.25} -N/C-900	Pluronic F127; Phenol/formaldehyde; Melamine/formaldehyde resol; Iron(III) chloride	Heat treatment; Hydrothermal reaction; Calcination; 2 nd heat treatment; NH ₃ annealing process	0.1 M KOH	Not given	0.812	Not given	11	3.56-3.67	2017, [12]
NH ₃ -Fe _{0.25} -N/C-900				1.018	0.865		5	4.08-4.20	
				0.1 M HClO ₄	0.935		0.710	–	

CCa-0.37-10	Calcium citrate; Urea; Ammonium iron(II) sulfate	Pyrolysis; Heat treatment	0.1 M KOH	0.91	0.814	Not given	~10	3.7	2019, [109]
			0.1 M HClO ₄	0.74	0.5		15	4	
NFe-PG	Glucose; Dopamine hydrochloride; Iron(III) nitrate	Pyrolysis	0.1 M KOH	1.00	0.827	Not given	-	3.86-3.97	2019, [39]
			0.5 M H ₂ SO ₄	Not given	0.823			Not given	
NFe-WHG	Water hyacinth; Dopamine hydrochloride; Iron(III) nitrate	Pyrolysis	0.1 M KOH	Not given	0.807	Not given	-	3.65-3.97	2019, [38]
			0.5 M H ₂ SO ₄		0.797			Not given	
FeNGC-950	Hydroxypropyl methylcellulose; Dicyandiamide; Iron(III) chloride	Heat treatment	0.1 M KOH	0.923	0.705	85	4.5-12.8	3.87-3.98	2019, [40]
Fe-N-comp-2	Carbide-derived carbon; 1,10-phenanthroline; Iron(II) acetate	Heat treatment; Ball milling; Pyrolysis;	0.1 M KOH	0.99	0.89	Not given	-	4	2018, [41]

CNT – Carbon nanotubes
 SA – Single atoms
 HPC – Hierarchically porous carbon
 CS – Carbon spheres
 CCa – Calcium citrate
 PG – Porous graphene
 WHG – Water hyacinth
 NGC – Nitrogen-doped graphene-like carbon sheets

Table A.2. Electrocatalytic activity comparison of recent advances on cobalt-nitrogen co-doped carbon materials. The potentials values correspond to the onset potential and half-wave potential values vs. the reversible hydrogen electrode (RHE) at 25 °C.

Catalyst	Precursors	Methods	Electrolyte	E _{onset} (V)	E _{1/2} (V)	Tafel slope (mV dec ⁻¹)	HO ₂ ⁻ yield (%)	n	Year&Ref.
Co,N-PCLs	ZIF-L with zinc(II) nitrate and 2-methylimidazole; ZIF-67 with cobalt(II) nitrate (0.4, 1.6, 3.2, 5.6 mmol)	Pyrolysis	0.1 M KOH	Not given	0.822-0.846	48.7	-	3.97 (4)	2019, [110]
Co-N-C-800	Poly(4-vinylpyridine); Silica colloid solution; Cobalt(II) chloride	Pyrolysis	0.1 M KOH	Not given	0.82	38	15.8	4.19	2019, [111]
Co-N/CNFs	Polyacrylonitrile; 4-Domethylaminopyridine; Cobalt(II) acetate	Air annealing process; Heat treatment	0.1 M KOH	0.82	0.70	Not given	~30	3.4	2017, [105]

Co,N-C900	O-Phenylenediamine; Ammonium peroxydisulfate; Cobalt(II) chloride; Colloidal silica solution	<i>o</i> PD polymerization; Pyrolysis; Heat treatment	0.1 M KOH	0.97	0.85	Not given	Not given	3.71-3.99	2018, [112]
Co/N-GLC	Cobalt(II) acetate; Ortho-phenanthroline; Tetraethylorthosilicate	Heat treatment; Pyrolysis	0.1 M KOH	0.966	0.946	Not given	–	3.98	2019, [113]
			0.1 M HClO ₄	0.825	Not given	Not given	Not given		
CoNPCs-700	Cobalt(II) nitrate; glycine	Pyrolysis	0.1 M KOH	0.93	0.81	Not given	10	3.84	2018, [6]
Co-N-PCN	Graphene oxide; Aniline; Pyrrole; Cobalt(II) nitrate	Polymerization, Carbonization	0.1 M KOH	0.90	0.82	69	Not given	4	2019, [114]
20Co-NC-1100	Zinc(II)nitrate; Cobalt(II) nitrate; 2-Methylimidazole; ZIF-8	Pyrolysis	0.5 M H ₂ SO ₄	0.93	0.80	Not given	5	4	2018, [107]

PCLs – Porous carbon leaves
 CNF – Carbon nanofibers
*o*PD – *o*-Phenylenediamine
 GLC – Graphene-like nanocarbon
 NPCs – Nitrogen porous carbon
 PCN – Porous carbon nanosheets

Table A.3. Electrocatalytic activity comparison of recent advances on manganese-nitrogen co-doped carbon materials. The potentials values correspond to the onset potential and half-wave potential values vs. the reversible hydrogen electrode (RHE) at 25 °C.

Catalyst	Precursors	Methods	Electrolyte	E_{onset} (V)	$E_{1/2}$ (V)	Tafel slope (mV dec ⁻¹)	HO ₂ ⁻ yield (%)	n	Year&Ref.
Mn-N-10 1100 °C at a heating rate of 5 °C min ⁻¹ for 10 h	Manganese metal flakes	Nitridation using N ₂	0.1 M KOH	1.410	Not given	Not given	–	3.75	2017, [115]
20Mn-NC-2 nd	Mn-doped ZIF-8; Manganese(II) chloride and nitrogen sources (for example, dipicolylamine, cyanamide, phenanthroline or melamine)	Pyrolysis; 2 nd pyrolysis	0.5 H ₂ SO ₄	Not given	0.80	80	< 2	4	2018, [101]
Mn-N-C	Manganese(II) chloride tetrahydrate; Aniline; Ammonia persulfate;	Aniline polymerization; Pyrolysis	0.5 H ₂ SO ₄	Not given	0.78	Not given	< 3	4	2019, [108]

Table A.4. Electrocatalytic activity comparison of recent advances on copper-nitrogen co-doped carbon materials. The potentials values correspond to the onset potential and half-wave potential values vs. the reversible hydrogen electrode (RHE) at 25 °C.


Catalyst	Precursors	Methods	Electrolyte	E_{onset} (V)	$E_{1/2}$ (V)	Tafel slope (mV dec ⁻¹)	HO ₂ ⁻ yield (%)	n	Year&Ref.
Cu-N/C	Copper(II) chloride; ZIF-8	Pyrolysis under N ₂ atmosphere	0.1 M KOH	0.883	0.804	Not given	12	3.75	2018, [116]
Cu (20.9 wt %)-N-C	Copper(II) acetate hydrate; L-glutamic acid; Dicyandiamide;	Pyrolysis under Ar atmosphere	0.1 M KOH	0.95	0.869	37	Not given	3.97	2018, [117]
Cu-N-C	Copper(I) chloride, Ammonia; Carbon black	Pyrolysis under Ar atmosphere	0.1 M KOH	0.91	0.80	63	2.92	3.95	2018, [118]
Cu-N/C	Copper(II) chloride ; ZIF-8	Pyrolysis under Ar/N ₂ atmosphere	0.1 M KOH	1.029	0.813	81	Not given	3.8	2019, [119]

Table A.5. Electrocatalytic activity comparison of recent advances on macrocycle doped carbon materials. The potentials values correspond to the onset potential and half-wave potential values vs. the reversible hydrogen electrode (RHE) at 25 °C.


Catalyst	Precursors	Methods	Electrolyte	E_{onset} (V)	$E_{1/2}$ (V)	Tafel slope (mV dec ⁻¹)	HO ₂ ⁻ yield (%)	n	Year&Ref.
Fe ₂₀ -VB12/C	Iron(II) chloride hexahydrate, vitamin B ₁₂ , carbon black	Pyrolysis under N ₂ atmosphere	0.1 M KOH	1.00	0.88	Not given	< 3.7	3.94 (4)	2018, [125]
			PBS pH 6	0.30				3.97	
MWCNT-FeP	Organic synthesis	Organic synthesis	PBS pH 8	0.16	Not given	Not given	Not given	3.95	2018, [128]
			PBS pH 10	0.13				3.96	
FeP-C	FeTMPPCI, carbon black	Pyrolysis under Ar atmosphere	0.1 M KOH	0.936	0.87		< 3	4	2017, [161]
			0.1 M HClO ₄	0.824	0.748	Not given	7.6	3.9	
C-TP-FE700 SMCs	HTP, Iron(II) chloride tetrahydrate, carbon black	Hydrothermal and calcination reaction	0.1 M KOH	0.976	0.865	62	Not given	4.0	2018, [131]
			0.1 M HClO ₄	Not given	0.720	Not given	Not given	3.88	

MnTPP-cov/1			0.5 H ₂ SO ₄	0.30		125	–		
MnTPP-cov/5	TPP-NH ₂ , Manganese(II) acetate	Covalent immobilization via electrodeposition on carbon cloth during 1, 5 and 10 minutes.	0.1 M KOH	0.30	Not given	110	–	4	2019, [135]
MnTPP-cov/10				0.45		113	–		
CoSAs/PTF	TPPCN, cobalt(II) hexahydrate	Pyrolysis under Ar atmosphere,	KOH	0.92	0.808	50	Not given	3.92-3.97	2019, [136]
Cu,SOCBP-C	Copper(II) perchlorate hexahydrate; Monomer OCBP	Polymerization of SOCBP	PBS pH 7	0.62	0.44	Not given	9	4	2018, [120]
FeTMPyP/Blm@rGO	Blm, FeTMPyP, GO		0.1 M KOH	0.83	0.73	Not given	~ 20	3.3	2019, [137]
ERGO-CoAPFP	CoAPFP, GO, EDC hydrochloride	Electrochemical reduction of GO	0.1 M KOH	0.911	Not given	Not given	~ 20	3.8	2014, [138]
N-CoTPP-graphene	CoTPP, GO		PBS pH 7	0.331	Not given	Not given	Not given	3.7	2015, [139]
CoTMPyP/rGO	GO, CoTMPyP		0.1 M KOH	Not given	0.445	Not given	Not given	3.88	2017, [140]

MWCTNs – Multiwalled carbon nanotubes
 FeTMPPCl – 5,10,15,20-tetrakis(4-methoxyphenyl)-21H, 23H-porphine iron(III) chloride
 SMCs – Superior trace-metal catalysts
 HTP – Meso-tetra(4-pyridyl)porphyrin
 TPP-NH₂ – 5-(4-aminophenyl)-10,15,20-triphenylporphyrin
 PTF – Porous porphyrinic triazine-based frameworks
 SA – Single atom
 TPPCN – 5,10,15,20-tetrakis(4-cyanophenyl)porphyrin
 SOCBP – (5,50-(9-octyl-9H-carbazole-2,7-diyl)bis(1,10-phenanthroline)
 Blm – Benzimidazole
 FeTMPyP – Fe(III)-tetra(1-methyl-4-pyridyl)porphyrin
 CoAPFP – Cobalt[5,15-(p-aminophenyl)-10,20(pentafluorophenyl)-porphyrin]
 ERGO – Electrochemically reduced graphene oxide
 EDC hydrochloride – N-(3-dimethylaminopropyl)-N0-ethylcarbodiimide hydrochloride
 CoTPP – Cobalt tetramethoxyphenylporphyrin
 CoTMPyP – Cobalt(II) 5, 10, 15, 20-tetrakis (N-methylpyridinium-4-yl) porphyrin



47th General Assembly
8 - 15 August, 2013



44th World Chemistry Congress
11 - 16 August, 2013

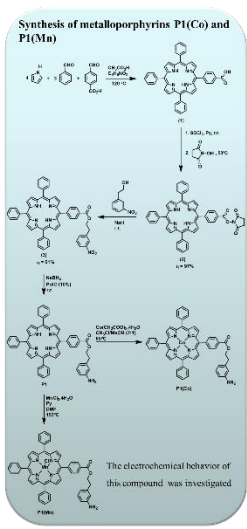
Direct Borohydride Fuel Cells: development of conducting polymers based on metalloporphyrins for oxygen reduction

José A. S. Cavaleiro¹, Cláudia M. B. Neves¹, I. M. Ornelas², A. S. Viana², M. Graça P. M. S. Neves¹, J. P. Correia²
¹Department of Chemistry & QOPNA, University of Aveiro, 3810-193 Aveiro, Portugal
²Department of Chemistry and Biochemistry & CQB, University of Lisbon, 1749-016 Lisbon, Portugal
 Presenting author: jcavaleiro@ua.pt

INTRODUCTION

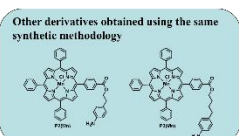
Direct borohydride fuel cells (DBFC) are currently recognized as promising chemical energy converters. The preparation of new electrocatalysts is one of the most important subjects in that field. Cobalt ions inserted into "conducting polymers like" matrices have revealed activity comparable to that of platinum for the electrochemical oxygen reduction [1]. This activity can be explained by the occurrence of metal-nitrogen active sites in such materials [2]. Also, the classical conducting polymers such as the polypyrrole and the polyaniline have revealed interesting activity for the molecular oxygen electroreduction [3]. Therefore, this work aims to associate the advantageous features of both materials by preparing conducting polymer films based on polyaniline incorporating metalloporphyrins with potential catalytic action. In the present work the synthetic routes to achieve the metalloporphyrins P1(Co) and P1(Mn) specially functionalized with an aniline-type moiety will be shown [4]. Aiming the generation of conducting polymeric films, the electrochemical behaviour of these novel compounds is investigated, and the anodic oxidation of such tailored monomers is studied *in-situ* by ellipsometry and electrogravimetric techniques. The modified electrodes are morphologically characterized by Atomic Force Microscopy and their activity towards molecular oxygen reduction is evaluated.

Synthesis of metalloporphyrins P1(Co) and P1(Mn)

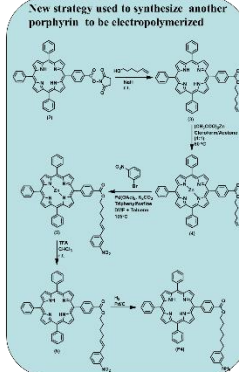


The electrochemical behavior of this compound was investigated.

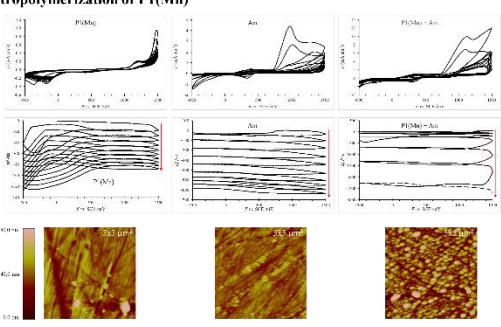
Other derivatives obtained using the same synthetic methodology



New strategy used to synthesize another porphyrin to be electropolymerized

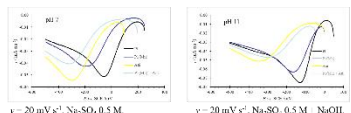


Electropolymerization of P1(Mn)



Mass increase during the growth of all films confirms the formation of a new phase on the electrode surface. Deposition of material starts at high potentials ($E \geq 1.4$ V) for films containing P1(Mn), at a lower potentials ($E \geq 0.7$ V) for the PANi film. The PANi and the copolymerized films show a pair of redox peaks at $E \approx 0.35$ V which can be attributed to the electrochemical conversion of the PANi backbone. The amount of deposited material and the currents registered are much greater for the copolymer. AFM imaging confirms that this film has a rougher morphology and, consequently, a higher surface area.

Catalytic currents for the reduction of O₂



All films are sensitive to the presence of O₂ in neutral and basic solutions.








Conclusions:

- The metalloporphyrins P1(Co) and P1(Mn) bearing an electropolymerizable aniline group in a peripheral chain were successfully synthesized and the same synthetic methodology was used to synthesize two other metalloporphyrins (P2(Mn) and P3(Mn)).
- A new strategy was used to synthesize another similar porphyrin (P3).
- The electrochemical behavior of P1(Mn) and their catalytic activity towards the oxygen reduction was evaluated.
- It is possible to modify the electrode surface through potential cycling in a solution containing P1(Mn). However, a higher surface coverage is obtained through copolymerization of P1(Mn) with An.
- The P1(Mn) film generates an electrocatalytic current that is comparable to that obtained with Pt in basic solution. The PANi- and copolymer-modified electrodes show worse performance for the reduction of molecular oxygen despite having a higher surface area, possibly due to a decreased accessibility of Mn-containing electrocatalytic sites.

Acknowledgements: Thanks are due to the Universities of Aveiro and Lisbon, to "Fundação para a Ciência e a Tecnologia"(FCT) / Project PTDC/QUI-QUI/121857/2010 and to the National NMR Network. CMB Neves thanks PTDC/ QUI-QUI/121857/2010 for her grant.

References

1. H. Y. Qin, Z. X. Liu, W. X. Yin, J. K. Zhu and Z. P. Li, *J. Power Sources* **185**, 909 (2008). 2. a) R. Bashyam and P. Zelenay, *Nature* **443**, 63 (2006). b) J. Ma, J. Wang and Y. Liu, *J. Power Sources* **172**, 220 (2007). 3. V. G. Khomenko, V. Z. Barzakov and A. S. Katashinski, *Electrochim. Acta* **50**, 1675 (2005). 4. K. M. Kadish, K. M. Smith and R. Guilard (Eds.), *The Porphyrin Handbook* (Academic Press, London, 2000).

Synthesis of new metalloporphyrins with potential catalytic action for development of conducting polymers

Cláudia M. B. Neves^a, I. M. Ornelas^b, A. S. Viana^b, M. Graça P. M. S. Neves^a, J. P. Correia^b, José A. S. Cavaleiro^a

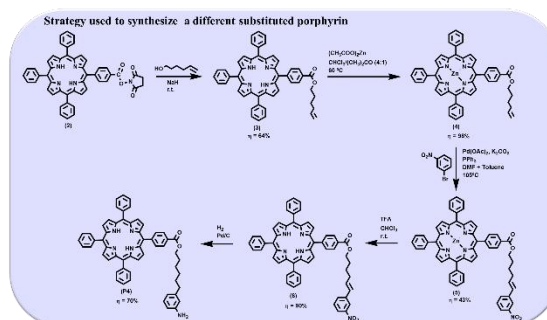
^aDepartment of Chemistry & QOPNA, University of Aveiro, 3810-193 Aveiro, Portugal;

^bDepartment of Chemistry and Biochemistry & CQB, University of Lisbon, 1749-016 Lisbon, Portugal

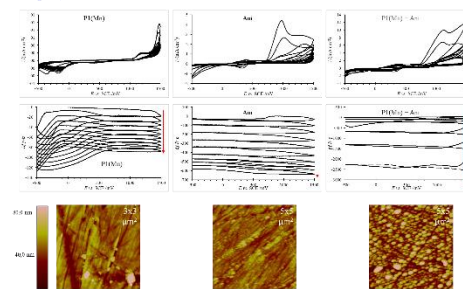
Email: claudianeves@ua.pt

INTRODUCTION

The direct borohydride fuel cells are currently recognized as the most promising chemical energy converters. The preparation of new electrocatalysts is one of the most important subjects in that field. It is known that some conducting polymer matrices containing metal-nitrogen active sites have revealed high activity for the electrochemical oxygen reduction.¹ This hypothesis is supported by the very good performance of metalloporphyrins and phthalocyanines in such processes.² Also, the classical conducting polymers like the polypyrrole and the polyaniline derivatives have revealed interesting activity for the molecular oxygen electroreduction.³ Therefore, it is intended to associate the advantageous features of those materials by preparing conducting polymer films based on polyaniline incorporating metalloporphyrins with potential catalytic action. The route to prepare the electrocatalysts for oxygen reduction involves the synthesis of specially designed Co and Mn porphyrin complexes bearing aniline-type moieties suitable for electropolymerization. From these monomers, polymer films will be electrogenerated on conducting substrates. In this communication the synthetic routes to achieve novel metalloporphyrins specially functionalized with an aniline-type moiety are shown.⁴ The ability of such compounds to form thin films onto solid surfaces by electropolymerization is also demonstrated. The electrochemical behaviour of these novel compounds is investigated, and the anodic oxidation of such tailored monomers is studied by electrogravimetric technique. AFM studies are also considered.



Electropolymerization of P1(Mn)



Growth conditions: $v = 50 \text{ mV s}^{-1}$, 10 cycles; solutions: LiClO_4 0.1 M, CH_3CN ; concentrations of the monomers: $[\text{An}] = 50 \text{ mM}$, $[\text{P1(Mn)}] = 0.5 \text{ mM}$.

Conclusions

- Porphyrins with aniline-type substituents and their Co and Mn complexes to be used in electropolymerization studies have been prepared and the electrochemical behavior of one of them [P1(Mn)] has been already evaluated.
- It is possible to modify the electrode surface through potential cycling in a solution containing P1(Mn).
- Mass increase during the growth of all films confirms the formation of a new phase on the electrode surface.
- The amount of deposited material and the currents registered are much greater for the copolymer.
- AFM imaging confirms that the copolymer has a rougher morphology and, consequently, a higher surface area.

Acknowledgements: Thanks are due to the Universities of Aveiro and Lisbon, to "Fundação para a Ciência e a Tecnologia" (FCT, Portugal) / Project PTDC/QUI-QUI/121857/2010. We also thank the European Union, QREN, FEDER and COMPETE for funding the QOPNA research unit (project PFC-C/QUI/0062/2011), and the Portuguese National NMR Network also supported by funds from FCT. Cláudia M. B. Neves thanks PTDC/QUI-QUI/121857/2010 for her grant.

References:

1. a) Qin H. Y.; Liu Z. X.; Yin W. X.; Zhu J. K.; Li Z. P. *J. Power Sources* **2008**, *185*, 909. b) Bashyam, R.; Zelenay P. *Nature* **2006**, *443*, 63. c) Ma J.; Wang J.; Liu Y. *J. Power Sources* **2007**, *172*, 220. 2. a) Tyurin, V. S.; Radyushkina K. A.; Levina O. A.; Tarasevich M. R. *Russ. J. Electrochem.* **2001**, *37*, 843. b) Ma J.; Wang J.; Liu Y. *J. Power Sources* **2007**, *172*, 220. 3. Khomenko V. G.; Barzakov V. Z.; Katashinski A. S. *Electrochim. Acta* **2005**, *50*, 1675. 4. a) Kadish K. M.; Smith K. M.; Guillard R. (Eds.), *The Porphyrin Handbook* (Academic Press, London, **2000**). b) Lacerda P. S. S.; Silva A. M. G.; Tomé A. C.; Neves, M. G. P. M. S.; Silva A. M. S.; Cavaleiro J. A. S.; Lamas-Saiz A. L. *Angew. Chem. Int. Ed.* **2006**, *45*, 5487.

Synthesis and characterization of rGO/M 2 and 10 wt%-N co-doped (M=Co, Fe, Mn, Ni, Cu and Rh) as abiotic electrocatalyst for oxygen reduction reaction

Alves A. C.¹, Correia J. P.¹, Dubois L.², Zebda A.³

¹ Grupo de Electroquímica Interfacial, Centro de Química e Bioquímica, Centro de Química Estrutural, Faculdade de Ciências da Universidade de Lisboa, Campo Grande 016, 1749-016 Lisboa, Portugal; ² Université Grenoble Alpes, CEA, CNRS, INAC, Grenoble 38000, France; ³ UGA-Grenoble 1/CNRS/INSERM/TIMC-IMAG UMR 2252, Grenoble, 38000, France.

BACKGROUND AND INTRODUCTION

The development of new and non-precious metal electrocatalyst based on transition metals for the oxygen reduction reaction (ORR) is the key to improve the energy conversion technology such as biofuel cells. In order to improve the cell efficiency of fuel cells by 4-electron reduction, the presence of an efficient catalyst as cathode for the oxygen reduction reaction is essential. Extensive research has been focused on the development of non-noble and highly efficient materials such as single atom transition metals [3-5] and macrocylic compounds [6-8] in a nitrogen-doped carbon matrix. The increasing of catalytic sites by an atom dispersion over a conductive and large surface area is a new strategy to enhance the ORR catalytic activity through the maximization of exposure of the atom. Therefore, in this work, we described a new methodology of synthesis of nitrogen-doped reduced graphene oxide and the incorporation of 2 and 10 wt % single atom transition metal catalysts for the electrochemical reduction of oxygen in neutral and alkaline media.

EXPERIMENTAL

Synthesis of rGO/M 2 & 10 wt%
 Extra exfoliation of graphene
 Incorporation of defects
 Co-doping with N and metal or macrocycle

Electroreduction of oxygen, evaluated by LSV with a glassy carbon (0.19 cm²) rotating disc electrode in PBS pH 7.4 and 0.1 M KOH solutions (10 mV/s, 400 to 2400 rpm).

Calculation of the number of electrons through Koutecký-Levich equation

$$\frac{1}{i} = \frac{1}{i_K} + \frac{1}{i_{Lev}} = \frac{1}{i_K} + \frac{1}{0.62nFD_i^{2/3}\omega^{1/2}v^{-1/6}C_0^*}$$

RESULTS AND DISCUSSION

CHARACTERIZATION OF THE MATERIALS

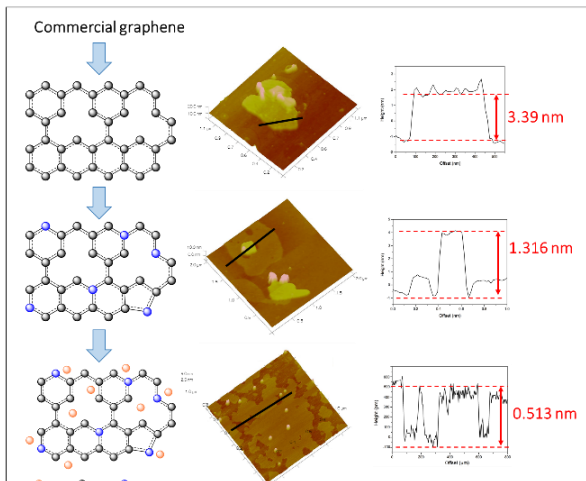


Figure 1. AFM images of modified electrodes: GO, GON and rGO/Co 2% and correspondent AFM profiles. AFM images show multi and monolayers of graphene involving a good exfoliation of the commercial graphene; The incorporation of N and metals may cause some aggregation of the GO.

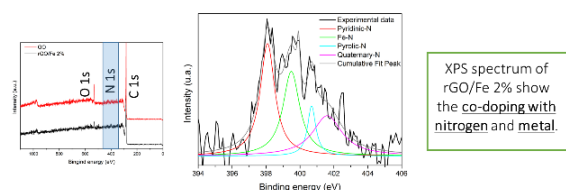


Figure 2. XPS general spectrum and high-resolution N 1s core level spectrum of GO and rGO/Fe 2%.

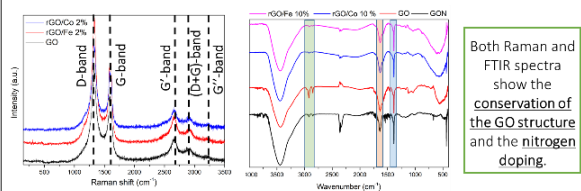


Figure 3. Raman spectrum of GO, rGO/Fe 2% and rGO/Co 2%; FTIR spectra of GO, GON, rGO/Fe 10% and rGO/Co 10%.

OXYGEN REDUCTION REACTION ON RGO/M CATALYSTS

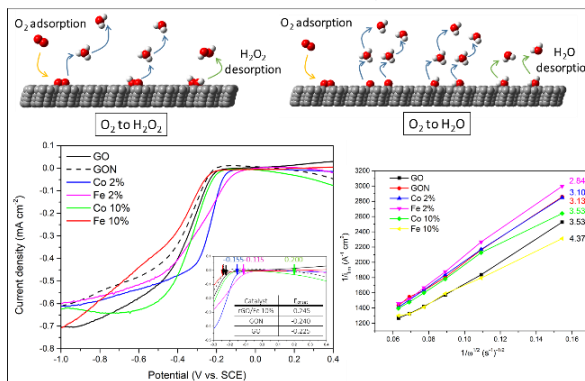


Figure 4. Rotating disk voltammograms of rGO/M 2 and 10 wt% measured in air-saturated 0.1 M KOH solution at 1600 rpm; Koutecký-Levich plot of different electrocatalysts at -1 V and the respective number of electrons transferred.

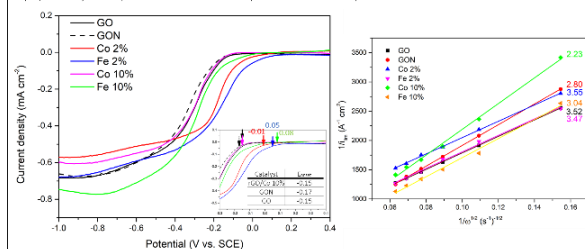


Figure 5. Rotating disk voltammograms of rGO/M 2 and 10 wt% measured in air-saturated PBS pH 7.4 solution at 1600 rpm; Koutecký-Levich plot of different electrocatalysts at -1 V and the respective number of electrons transferred.

LSVs show relevant contribution of the N-doped graphene for the overall ORR performance; Iron-doped graphene materials are considered more efficient towards extensive oxygen reduction.

FUTURE WORK

- Further physical characterization of the catalysts, such as BET and ICP analysis.
- Study the mechanism of ORR in the synthesized materials.
- Insertion of porphyrins in the GO and its electrochemical characterization.
- Finer assessment of the number of transferred electrons and % of H₂O₂ formed in ORR through RRDE experiments.

ACKNOWLEDGEMENTS

The authors thank the Fundação para a Ciência e Tecnologia for the financial support through the project UID/Multi/00612/2019

[1] Zhong et al. in *Chem Rec*, 2018, 18(7-8), 840-848; [2] Huang et al. in *Sci China Chem*, 2017, 60(12), 19-22; [3] Yan et al. in *J. Alloys Compd*, 2019, 773, 819-827; [4] Yan et al. in *Int. J. Hydrog. Energy*, 2019, 44, 409-410; [5] Zhang et al. in *Angew. Chem. Int. Ed.*, 2018, 57, 9038-9043; [6] Liu et al. in *Int. J. Hydrog. Energy*, 2018, 43, 16230-16239; [7] Riquelme et al. in *Electrochim. Acta*, 2018, 265, 547-555; [8] Almeida et al. in *Electrochim. Acta*, 2016, 188, 1-12.

Appendix D



06 CE



Funding:

Centro de Química Estrutural is funded by Fundação para a Ciência e Tecnologia – project UID/Multi/00612/2019.

References:

Jorio, A.; Saito, R.; Dresselhaus, M.S.; Dresselhaus, G. *Raman spectroscopy in graphene related systems* (2011). Weinheim, Germany: Wiley-VCH, 3-13;

Ferrero, G.A.; Diez, N.; Sevilla, M.; Fuertes, A. B. *ACS Appl. Energy Mater.* (2018), 1(11), 6560-6568.

Ferrero, G.A.; Diez, N.; Sevilla, M.; Fuertes, A.B. *Microporous and Mesoporous Materials* (2019), 278, 280-288

Synthesis and characterization of rGO/M 2wt%-N co-doped (M=Co, Fe, Mn, Ni, Cu and Rh) as abiotic electrocatalyst for oxygen reduction reaction

Alves A. C.¹, Correia J. P.¹, Dubois L.², Zebda A.³

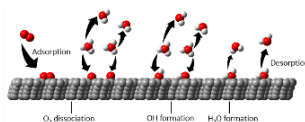
¹ Grupo de Electroquímica Interfacial, Centro de Química e Bioquímica, Centro de Química Estrutural, Faculdade de Ciências da Universidade de Lisboa, Campo Grande 016, 1749-016 Lisboa, Portugal; ² Université Grenoble Alpes, CEA, CNRS, INAC, Grenoble 38000, France; ³ UGA-Grenoble 1/CNRS/INSERM/TIMC-IMAG UMR 2252, Grenoble, 38000, France.

BACKGROUND AND INTRODUCTION

The development of new and non-precious metal electrocatalyst based on transition metals for the oxygen reduction reaction (ORR) is the key to improve the energy conversion technology.

Strategy:

Increase the catalytic sites by an atom dispersion over a conductive and large surface area.



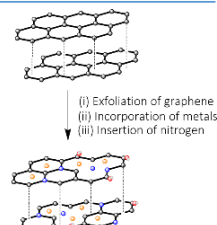
Main goals:

Synthesis of a 2 wt% single-atom transition metal catalyst supported in nitrogen-reduced graphene oxide;

Electrochemical evaluation of ORR by linear sweep voltammetry (LSV) with a rotating disc electrode in PBS pH 7.4 and 0.1 M KOH pH 13 solutions.

METHODS

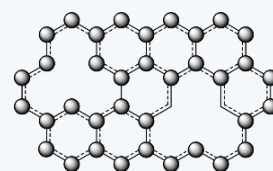
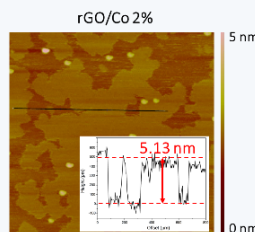
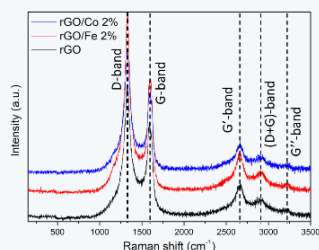
Extra exfoliation of graphene
Incorporation of defects
Co-doping with N and metal



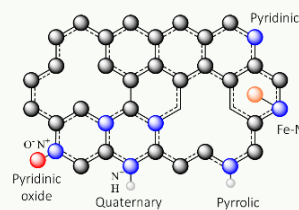
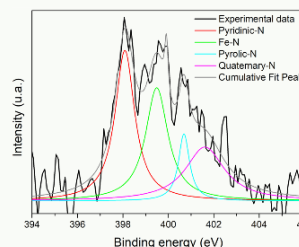
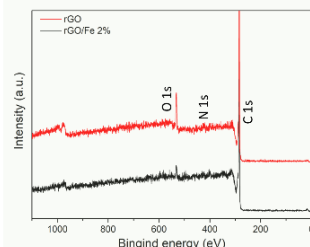
Physical Characterization by
XPS
Raman
AFM

Electroreduction of oxygen, evaluated by LSV with a glassy carbon rotating disc electrode in PBS pH 7.4 and 0.1 M KOH pH 13 solutions (10 mV/s, 400 to 2400 rpm).

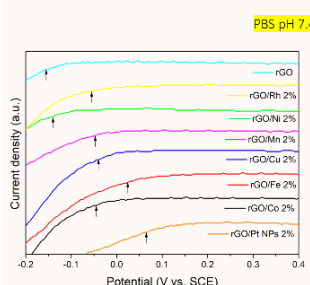
ELECTROCATALYSTS & OXYGEN REDUCTION REACTION – DISCUSSION AND RESULTS



Raman spectra of rGO and its derivatives and AFM measurements confirm the incorporation of defects in the graphene structure.

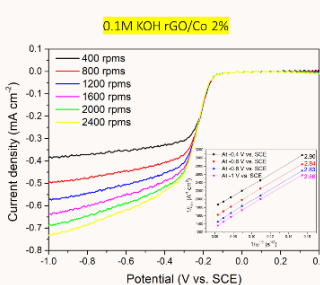


XPS general spectrum and high-resolution N 1s core level spectrum of rGO/Fe 2% show the co-doping with nitrogen and metal.



PBS pH 7.4 and 1600 rpm

Catalyst	E_{onset}/V	$E_{1/2}/V$	$J_{lim}/mA\text{cm}^{-2}$	Nr of e
rGO	-0.025	-0.022	-0.7334	3.17
rGO/Fe 2%	-0.045	-0.190	-0.5704	2.69
rGO/Mn 2%	-0.050	-0.335	-0.5602	3.74
rGO/Cu 2%	0.040	-0.215	-0.8047	2.66
rGO/Ni 2%	-0.140	-0.310	-0.6672	2.78
rGO/Rh 2%*	-0.055	-0.260	-0.6570	2.58
rGO	-0.155	-0.385	-0.7283	-
rGO/Pt NPs 2%*	0.065	-0.230	-0.7996	1.60



CURRENT & FUTURE WORK

- Incorporation of porphyrins in the rGO structure and its electrochemical and physical characterization.
- Synthesis of new electrocatalyst with 10% wt (or more!) of transition metal and their characterization by AFM, Raman, XPS and ICP.
- Electrochemical oxidation of glucose in both neutral and alkaline media in the presence of rGO/M 10%.